The Role of Afferent Hippocampal to Prefrontal Cortex Projections in a Mouse Model of Alzheimer´s Disease

Dissertation zur Erlangung
des Doktorgrades (Dr. rer. nat.)
der **Mathematisch-Naturwissenschaftlichen Fakultät**
der Rheinischen Friedrich-Wilhelms-Universität Bonn

vorgelegt von

Emine Ciftci

aus
Dortmund

Bonn, 2025

Angefertigt mit Genehmigung der Mathematisch-Naturwissenschaftlichen Fakultät der Rheinischen Friedrich-Wilhelms-Universität Bonn

Gutachter/Betreuer: Prof. Dr. Martin Fuhrmann

Gutachterin: Prof. Dr. Elvira Maas

Erscheinungsjahr: 2026

Tag der Promotion: 11.02.2026

May we never lose the passion to pursue what we love, no matter how rough the road may get…

The task is not to see what has never been seen before, but to think what has never been thought before about what you see every day.

Erwin Schrödinger

Acknowledgements

My special thanks go first to my doctoral advisor, supervisor, and mentor, Prof. Martin Fuhrmann, whose valuable insights and professional expertise significantly contributed to the success of finishing this project. The stimulating discussions and constructive feedback continually motivated me to consider new perspectives and sharpen my focus. I have learned so much from you − both scientifically and personally.

Prof. Elvira Maas, my second supervisor, for her valuable insights and ideas that helped improve my data. I´m also grateful to Prof. Martin Reuter and Prof. Walter Witke for being a part of my defense committee.

A heartfelt thank you to Dr. Sabine Krabbe for your personal and scientific support! Thank you for being there and for providing relief, ideas, and improvements to my project. I truly appreciate your calm presence and your help!

I would also like to extend my sincere gratitude to Prof. Stefanie Poll, who gave me the opportunity to work on this project.

To Nancy El Deiry, the good fairy of the DZNE − thank you! Without you, organizing all the (travel) documents and bookings would have been impossible.

I am also grateful to my colleagues in the Fuhrmann lab, who supported me with both advice and hands-on help.

A special mention goes to my beloved friends and great scientists Shuvrangshu Guha, Arush Baijal, Dilek Mercan-Saglam, Benay Baskurt, Alana Stüdle, Hanna Khomyak, Ayse Ulusoy, Eileen Tedt, Nazlı Altınısık, Seda Koyun, Burcu Sivri, Mehwish Salamat, Berkan Koyak, and Niko Moriba Britt. Whether through inspiring conversations, shared perseverance, or the exchange of ideas − your scientific and emotional support meant so much to me. You guys were my support system, my laughter, my reality check, and at times, my co-survivors. Together, we navigated the ups and downs of experiments, deadlines, data loss, caffeine dependence, and existential crises. You reminded me that giving up was never an option.

To my lifesavers and favorite animal caretakers: Mateusz Krawczyk, Jan Engels, and Jaqueline Agor − Danke von ganzem Herzen für euren Einsatz!
Many thanks also to Dr. Ireen König, Dr. Hans Fried and, Dr. Severin Filser for being there and troubleshooting during the never-ending microscope sessions. Without their varied contributions, completing this thesis in its present form would not have been possible.

Lastly, my deepest gratitude goes to my family, especially Seyyid Ahmed Ciftci, Tariq Doukkali Attar and Daniel Weidlich. Mehtap, Nourajni, Fatma, Base, Ruth Kiedrowski and all my precious friends, whose unwavering support and confidence carried me through this journey − Thank you! Your encouragement and understanding gave me the strength to keep going and focus on my work. My heartfelt thanks go to Kaneschka, for being a role model.

And finally, I would like to thank my mice, without whom this research would not have been possible in its current form!

Muhakkak ki, her zorluğun ardından bir kolaylık vardır!

Summary

Alzheimer's disease is the most common cause of dementia and is marked by progressive cognitive decline. Early dysfunction appears in the hippocampus and later involves the prefrontal cortex. These two brain regions are strongly interconnected and support critical functions such as spatial navigation, working memory, and memory consolidation. Healthy animals show strong synchronization between hippocampal and prefrontal activity, especially in the theta (4–12 Hz) and gamma (40–80 Hz) ranges, which supports memory performance.

While hippocampal pathology in Alzheimer's disease has been studied extensively, the specific role of disrupted hippocampal-prefrontal circuitry in driving memory deficits remains unclear. In particular, it is not well understood how excitatory and inhibitory hippocampal projections to the prefrontal cortex are altered in Alzheimer´s disease, and how such changes impair local network activity and cognitive function.

The first aim of this project is to describe and characterize hippocampal projections to the prefrontal cortex in a transgenic mouse model of Alzheimer's disease such as the APP/PS1 mouse model. This will involve the use of cell type-specific viral tracers in Cre-driver mouse lines, such as Somatostatin-Cre, combined with immunohistochemical techniques to distinguish excitatory from inhibitory pathways. This anatomical mapping will provide insights into whether certain neuronal subtypes are particularly vulnerable to Alzheimer's disease-related degeneration.

The second objective is to determine the functional consequences of any structural alterations. Using calcium imaging in awake, behaving mice engaged in a spatial working memory paradigm, I monitored how hippocampal inputs recruit local prefrontal circuits during encoding and retrieval phases. Disruptions in synchronous oscillatory activity will be directly related to cognitive impairments characteristic of Alzheimer's disease. To establish causal links, chemogenetic manipulations were employed in healthy control animals to selectively silence hippocampal projections to the prefrontal cortex at defined stages of the memory task, thereby experimentally simulating the connectivity deficits observed in Alzheimer's disease. Finally, by reactivating or enhancing specific prefrontal neuronal ensembles, I tested whether memory performance can be restored.

Together, these experiments aim to advance our mechanistic understanding of how abnormal hippocampal-prefrontal interactions drive cognitive decline in Alzheimer's disease and to highlight potential circuit-level targets for therapeutic intervention.

Table of Contents

1. Introduction

This doctoral thesis deals with the anatomy, connectivity, and function of two brain regions that are essential for memory and executive functions – the ventral hippocampus (vHPC) and the medial prefrontal cortex (mPFC) – and examines how these areas are impaired in models of Alzheimer's disease (AD). In particular, the focus is on the role of these areas in spatial working memory (SWM) and the underlying neural circuits, such as somatostatin (SST^+) -expressing interneurons (INs) in the *Cornu amonis 1* (CA1) region in the vHPC. Understanding these relationships is of great importance, as early changes in these networks are often signs of incipient cognitive decline, and insights into the underlying mechanisms could potentially lead to new therapeutic approaches.

1.1. Alzheimer´s Disease: Pathophysiology and Impact on Neural Circuits

AD is the most common form of dementia and was first described at the beginning of the 20th century by the German psychiatrist and neuropathologist Alois Alzheimer. In 1907, Alzheimer presented the pathological findings of his patient Auguste Deter, who was already suffering from severe memory impairment, speech difficulties, and profound personality changes in her middle age. After her death, he discovered characteristic deposits during histological examination of her brain, which he described as senile plaques (SP) and neurofibrillary tangles (NFTs) (Alzheimer 1906, 1907a, 1907b). These observations marked the beginning of systematic research into neurodegenerative diseases and led psychiatrist Emil Kraepelin to coin the term “Alzheimer's disease” in the 8th edition of his Handbook of Psychiatry (1911) (Möller und Graeber 1998; Cipriani et al. 2011).

Since this initial description, our understanding of AD has changed fundamentally. While it was initially described as a rare, early-onset disease, it is now known to be predominantly a neurodegenerative disorder that occurs in older age. With currently around 50 million people affected worldwide and a projected increase to over 150 million by 2050, AD represents one of the greatest medical and social challenges.

Clinically, AD manifests itself in progressive cognitive decline, initially beginning with memory impairment and subtle neuropsychiatric symptoms such as depression, anxiety, sleep disturbances, and social withdrawal. As the disease progresses, pronounced deficits in language, orientation, and executive functions develop, accompanied by behavioral abnormalities that ultimately lead to a complete loss of independence. This individual burden

of disease is exacerbated by the immense strain on family members and society, which manifests itself in emotional and physical stress as well as significant economic costs.

A variety of risk factors have been identified that significantly influence the onset and progression of AD. Accumulating evidence emphasizes that AD is a multifactorial disorder shaped by an interplay between genetic, biological, and environmental risk factors. Increasing age remains the strongest risk factor, with the incidence rising sharply after the age of 65. A positive family history further elevates susceptibility, indicating the contribution of heritable determinants. On the molecular level, genetic predisposition plays a crucial role: while mutations in amyloid precursor protein (APP), presenilin-1 (PSEN1), and presenilin-2 (PSEN2) cause familial early-onset AD, the apolipoprotein E (ApoE) genotype represents the major genetic risk factor for the sporadic form. In particular, the presence of the ApoE4 allele significantly increases the likelihood of developing AD compared to other isoforms. Beyond genetics, external risk factors such as traumatic brain injury, hyperlipidemia, hypertension, diabetes mellitus, obesity, and elevated homocysteine levels have also been implicated in modulating disease onset and progression.

Pathophysiologically, AD is characterized by the extracellular deposition of amyloid-ß (Aß) plaques (Hardy und Allsop 1991; Regland und Gottfries 1992) and the intracellular formation of NFTs from hyperphosphorylated tau protein (Goedert 1993; Mandelkow und Mandelkow 1998). These changes initiate a complex network of secondary processes, including neuroinflammatory reactions (Aisen und Davis 1994; Heppner et al. 2015), synaptic dysfunction, mitochondrial disorders (Wang et al. 2025; Swerdlow 2020), oxidative stress (Praticò 2008; Wang et al. 2006; Keller et al. 2005), and vascular changes (L Lorenzini et al. 2024), which ultimately lead to the irreversible degeneration of neural networks. In addition to the amyloid and tau cascade hypothesis, several complementary mechanistic models have been proposed to explain the complex pathogenesis of AD. The hypothesis suggests that a loss of cholinergic neurons and reduced acetylcholine levels critically contribute to cognitive decline (Whitehouse et al. 1981; Francis et al. 1999), while the glutamate excitotoxicity hypothesis postulates that dysregulated glutamatergic signaling and NMDA (N-Methyl-D-Aspartate) receptor overactivation induce synaptic damage and neuronal death (Bukke et al. 2020). More recently, the microbiota-gut-brain axis hypothesis has gained attention, proposing that alterations in the gut microbiome can modulate systemic inflammation and neurodegeneration (Chen et al. 2022; Chandra et al. 2023). Furthermore, impairments in autophagy and proteostasis have been implicated, with evidence suggesting that defective clearance of misfolded proteins exacerbates Aß and tau accumulation (Zhang et al. 2021).

Finally, the metal ion hypothesis emphasizes the dysregulation of biometals such as zinc, copper, and iron in the brain, which can catalyze oxidative stress and promote Aß aggregation (Figure 1) (Bush et al. 1994; Zatta et al. 2009).

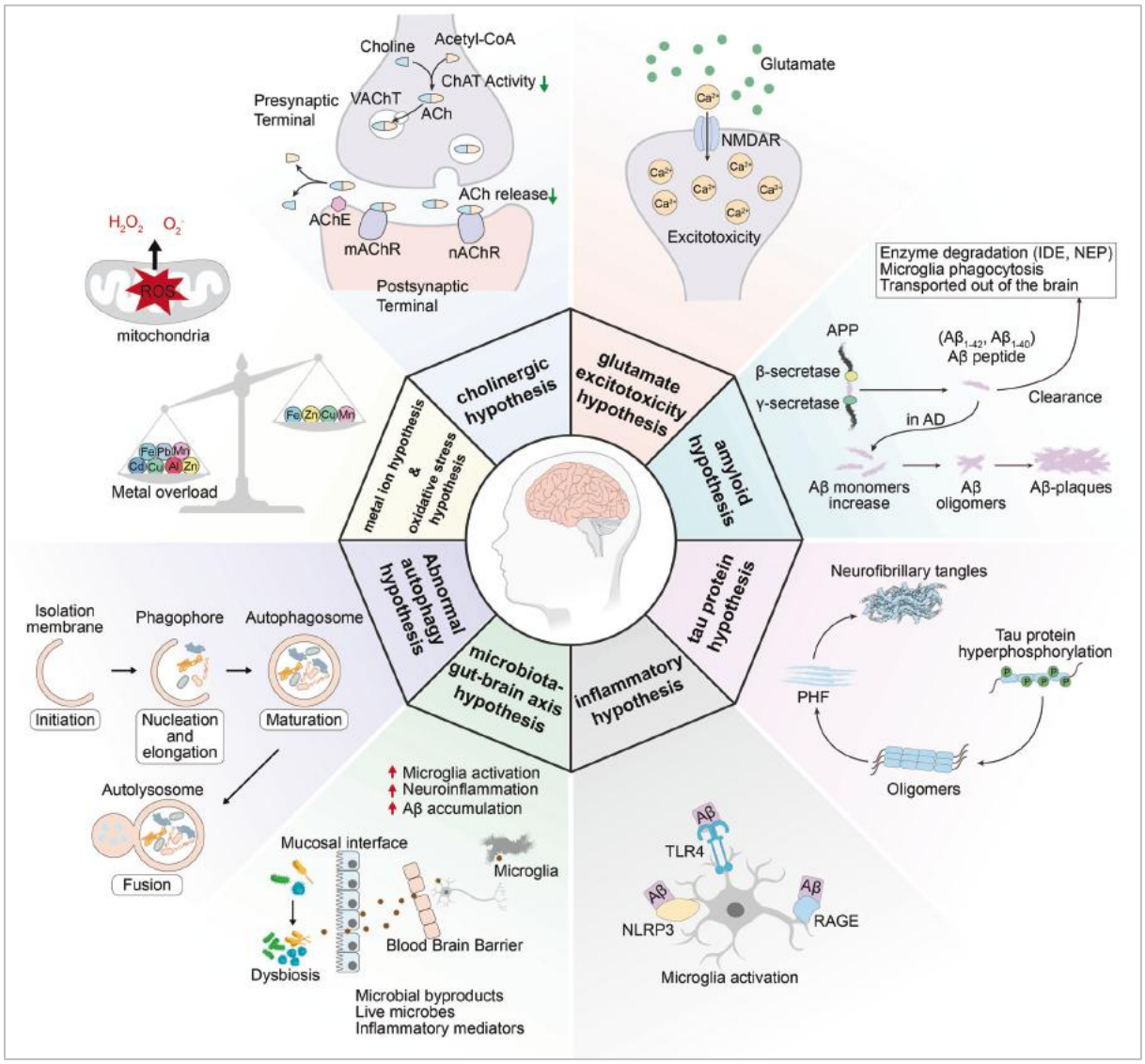

Figure 1. Schematic overview of major pathophysiological hypotheses in AD. The cholinergic hypothesis highlights reduced acetylcholine synthesis, impaired vesicular transport (VAChT), and altered receptor signaling. The glutamate excitotoxicity hypothesis describes excessive glutamatergic activity and NMDA receptor-mediated calcium influx, leading to excitotoxic damage. The amyloid hypothesis depicts the sequential cleavage of APP by ß- and γ-secretases, resulting in Aß monomers that aggregate into oligomers and plaques, with impaired clearance further exacerbating accumulation. The tau protein hypothesis focuses on tau hyperphosphorylation, oligomerization, and NFT formation. The inflammatory hypothesis emphasizes chronic activation of microglia through receptors such as TLR4 and RAGE, leading to NLRP3 (NACHT, LRR, and PYD domains-containing protein 3) inflammasome activation and sustained neuroinflammation. The microbiota–gut–brain axis hypothesis links dysbiosis and microbial byproducts crossing the blood-brain barrier with microglial activation and inflammatory cascades. The abnormal autophagy hypothesis outlines impaired formation and maturation of autophagosomes, preventing efficient degradation of toxic proteins. Finally, the oxidative stress and metal ion imbalance hypothesis illustrates mitochondrial dysfunction, ROS

production, and toxic effects of metal overload. Together, these interconnected pathways demonstrate the multifactorial nature of AD pathophysiology (figure from Zhang et al. 2024).

1.1.1. Pathophysiology of Alzheimer´s Disease

A main hallmark of AD is the abnormal accumulation of Aß, which is produced by proteolytic cleavage of the APP via ß- and γ-secretases (Hardy & Selkoe, 2002; Haass & Selkoe, 2007). The Aß42 peptide in particular has a pronounced aggregation tendency. It first forms soluble oligomers, which are now considered the key neurotoxic species, before forming fibrillar structures and extracellular plaques (De Strooper & Karran, 2016; Selkoe & Hardy, 2016).

At the functional level, Aß oligomers interfere with postsynaptic signal transmission by binding to receptors such as NMDA and AMPA (α-amino-3-hydroxyl-5-methyl-4-isoxazole-propionate) receptors and disrupting calcium (Ca^{2+}) homeostasis. This leads to a weakening of long-term potentiation (LTP) and an enhancement of long-term depression (LTD), processes that are closely related to learning and memory performance (Mucke & Selkoe, 2012; Long & Holtzman, 2019). In addition, Aß species activate intracellular stress signaling pathways, impair mitochondrial function, and increase the formation of reactive oxygen species (ROS), which promotes synaptic degradation and neuronal cell death (Figure 2).

In addition to these molecular mechanisms, Aß also acts as a disruptive factor at the level of neuronal networks. Imaging studies in animal models have shown that Aß is associated with neuronal hyperactivity, which occurs early in the disease and contributes significantly to cognitive symptoms (Busche & Konnerth, 2015; Busche & Konnerth, 2016). Palop and Mucke (2010, 2016) were able to demonstrate that Aß causes dysfunction of inhibitory interneurons and a shift in the excitatory-inhibitory balance, leading to pathological network activity. This manifests itself in epileptiform discharges, altered theta and gamma oscillations, and impaired communication between the hippocampus and cortex, which is directly linked to memory deficits.

In addition, amyloid pathology interacts closely with neuroinflammatory processes. Microglia and astrocytes are permanently activated by Aß deposits, release proinflammatory mediators, and exacerbate neuronal dysfunction via inflammasome-mediated mechanisms (Heneka et al., 2015). An additional pathological factor is the deposition of Aß in vessel walls, which leads to the development of cerebral amyloid angiopathy (CAA). This reduces the vascular clearance of Aß, thereby reinforcing the vicious cycle of pathological accumulation (Bero et al., 2011; Zott et al., 2018).

In summary, it appears that Aß is not only harmful through the formation of extracellular plaques, but primarily through its soluble oligomers, which impair synaptic transmission,

intracellular signaling pathways, and neuronal network dynamics. These multiple pathomechanisms − from the molecular to the systemic level − highlight the central role of Aß in Alzheimer's pathophysiology.

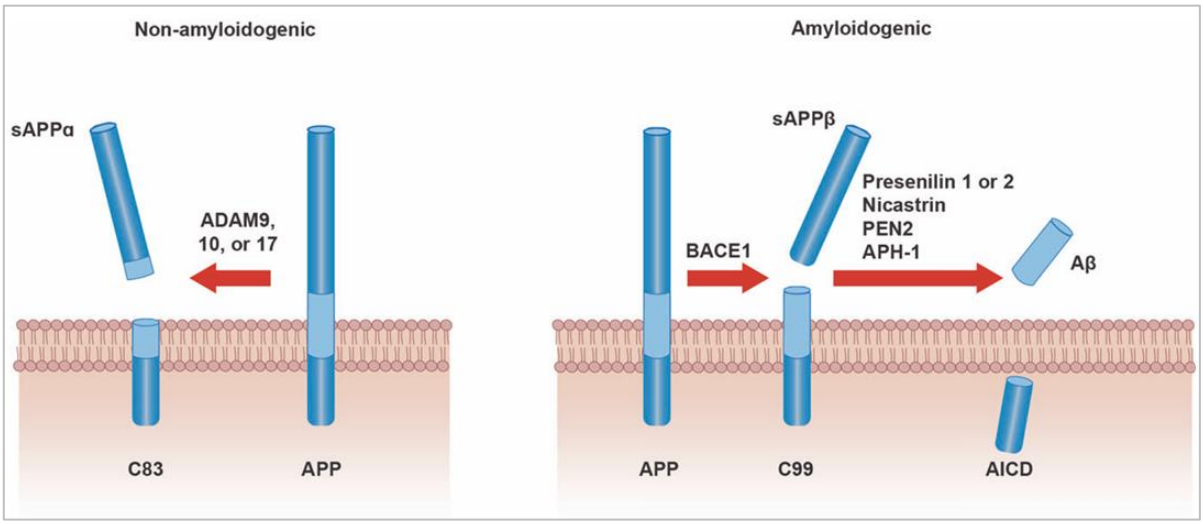

Figure 2. Schematic illustration of the non-amyloidogenic and amyloidogenic metabolic pathways. There are two enzymatic pathways APP can be cleaved: the non-amyloidogenic pathway (left), α-secretases of the ADAM family (ADAM9, ADAM10, or ADAM17) cleave APP within the Aß domain, releasing the soluble ectodomain sAPPα and leaving behind a membrane-bound C83 fragment, thereby preventing the formation of Aß. In the amyloidogenic pathway (right), sequential cleavage by ß-secretase (BACE1) and the γ-secretase complex (consisting of presenilin-1/2, nicastrin, PEN2, and APH-1) produces the soluble sAPPß fragment, the intracellular domain of APP (AICD), and Aß peptides. The latter, especially Aß42, tend to aggregate and represent the triggering species in the amyloid cascade hypothesis of AD (figure from Hampel et al. 2021).

1.1.2. Neurodegenerative Changes in Alzheimer´s Disease Mouse Model

Transgenic mouse models of AD, like APP/PS1, 5xFAD, or 3xTg-AD, are key tools for understanding the pathological mechanisms of the disease. Even if they do not fully reflect the clinical heterogeneity of humans, they reproduce essential neurodegenerative changes that correlate with cognitive deficits (Ashe und Zahs 2010; Jankowsky und Zheng 2017).

As mentioned, a key feature is the progressive deposition of Aß in the hippocampus and cortex. Soluble amyloid oligomers are particularly toxic, disrupting synaptic plasticity, blocking long-term potentiation, and causing dendritic spine loss (Selkoe und Hardy 2016; Walsh und Selkoe 2007). In APP/PS1 mice, it has also been shown that microglia-dependent mechanisms increase amyloid pathology. Heneka et *al.* demonstrated that activation of the NLRP3 inflammasome in microglia leads to increased Interleukin-1ß (IL-1ß) release, which enhances Aß deposition and ameliorates cognitive deficits. In contrast, mice lacking NLRP3 or caspase-1 show reduced plaque formation and improved memory performance (Heneka et al. 2013). Additionally, it has been shown that microglia release apoptosis-associated speck-like protein containing a CARD

(caspase recruitment domain) (ASC) specks, which interact extracellularly with Aß and promote its aggregation and spread − a mechanism that further exacerbates progressive amyloid pathology in transgenic mice (Venegas et al. 2017).

Simultaneously with amyloid pathology, some models such as 3xTg-AD also exhibit tau changes, which manifest as hyperphosphorylation and intracellular aggregates. This impairs axonal transport processes and enhances neuronal dysfunction (Oddo et al. 2003; Iqbal et al. 2009). Once again, neuroinflammation acts as a critical amplifier, as chronic microglial and astrocytic activation by amyloid and tau promotes an inflammatory microenvironment that supports synaptic dysfunction and neuronal loss (Heneka 2017).

Functionally, mouse models show a significant reduction in dendritic spines and synaptic markers, particularly in the hippocampus and prefrontal cortex (Spires-Jones und Hyman 2014). In addition, alterations in cholinergic, glutamatergic, and GABAergic transmission occur, disrupting the balance between excitatory and inhibitory signaling in the hippocampal-prefrontal network. This imbalance contributes significantly to deficits in working memory and cognitive flexibility (Palop und Mucke 2016, 2010; Busche und Hyman 2020).

To sum up, Alzheimer's mouse models represent central neurodegenerative pathologies − amyloid and tau pathology, neuroinflammation, synaptic and neuronal loss, and neurotransmission dysfunction. These processes interact to cause progressive network dysfunction and cognitive decline, providing valuable, even if still limited, insights into the complex mechanisms underlying AD.

1.1.3. Treatment and Limitations

Diagnostics have also evolved over the course of research history: from early clinical case reports and neuropsychological tests to modern biomarker and imaging techniques. In particular, the determination of Aß and tau proteins in cerebrospinal fluid, as well as the development of blood-based biomarkers and novel radioligand-based imaging, now make it possible to detect pathological changes in the preclinical phase. This is shifting the focus increasingly toward early detection, long before clinically manifest symptoms appear.

For a long time, purely symptomatic approaches were at the forefront of treatment, such as the use of cholinesterase inhibitors or NMDA receptor antagonists. In the recent past, however, the first disease-modifying approaches − in particular monoclonal antibodies against Aß such as aducanumab and lecanemab − have been successfully used clinically, even though their efficacy and safety are controversial (Ameen et al. 2024). At the same time, innovative therapeutic

approaches, including immunotherapies, stem cell and gene therapies, and proteolysis targeting chimera (PROTAC) -based strategies, are being tested in clinical trials.

1.2. Neuroanatomy and Circuitry of the Hippocampus and mPFC

1.2.1. Anatomy of the mPFC

The mPFC is a highly integrative region in the anterior frontal lobe that interacts closely with limbic, thalamic, and cortical networks. In rodents, it is typically divided into the prelimbic (PL), infralimbic (IL), and anterior cingulate cortex (ACC), which differ in both their cytoarchitecture and functional roles (Vertes 2006; Laubach et al. 2018). The PL is primarily involved in executive control and working memory, while the IL is relevant for emotion processing and fear extinction. The ACC performs integrative tasks in motivation, error detection, and attention (Bush et al. 2000).

The mPFC exhibits the typical six-layer organization of the neocortex, with pyramidal cells in layers II/III and V forming the main outputs. These projection neurons are embedded in dense feedback loops that integrate afferent signals from the hippocampus, amygdala, thalamus, and monoaminergic brainstem nuclei (Hoover und Vertes 2007). Especially relevant is the strong projection of the vHPC to the PL and IL, which represents an interface between context-dependent memory processing and executive control (Jay und Witter 1991; Spellman et al. 2015b). In contrast, the mPFC transmits feedback signals back to the hippocampus via direct pathways and via the thalamic nucleus reuniens, establishing a bidirectional flow of information (Vertes 2006).

The local network dynamics of the mPFC are largely regulated by inhibitory interneurons, especially parvalbumin (PV)- and SST-expressing populations. These interneurons control the temporal precision of action potentials and form oscillations that are necessary for synchronization with hippocampal networks (Courtin et al. 2014). Recent studies also show that the development and maturation of the mPFC is specifically sensitive to environmental influences and stress during adolescence, which can permanently alter the balance of excitatory and inhibitory signals (Goodpaster et al. 2025). Functional experiments show that specific stimulation of the mPFC can modulate competition between memory contents and improve retrieval (Khan et al. 2024).

In conclusion, the mPFC acts as a circuit hub that coordinates cognitive and emotional processes and, through its close connection to the hippocampus, creates the basis for working memory and context integration.

1.2.2. Anatomy of the Hippocampus

The hippocampus is a bilaterally arranged structure of the medial temporal lobe and is considered the central integration center of the limbic system. Its functions include episodic memory, spatial navigation, and contextual learning (Buzsáki und Moser 2013; Rolls und Treves 2024). Anatomically, the hippocampus can be divided into the classic subregions dentate gyrus (DG), CA1 − CA3, and subiculum. These areas are organized by the so-called trisynaptic circuit: neurons of the entorhinal cortex (EC) project via the perforant path (PP) to the DG, from there the mossy fibers extend to CA3, and Schaffer collaterals (Sch) finally connect CA3 with CA1. The output projections from CA1 and the subiculum in turn reach the entorhinal cortex and other cortical target areas, forming a feedback loop that is essential for memory consolidation (Figure 3) (Amaral und Witter 1989).

More recent models emphasize that the individual subfields perform specific computational functions: while the DG is primarily responsible for pattern separation, CA3 enables pattern completion through recurrent connections, and CA1 serves to integrate new representations with stored ones (Leutgeb et al. 2007; Rolls und Treves 2024). In addition to this internal architecture, the hippocampus is also organized longitudinally. Functional specializations are evident along the dorsoventral axis: the dorsal hippocampus (dHPC; posterior in humans) is more strongly associated with spatial and cognitive processes, while the vHPC (anterior in humans) primarily mediates emotional regulation, stress responses, and connectivity to the prefrontal cortex and amygdala (Fanselow und Dong 2010; Dalton et al. 2022).

At the cellular level, glutamatergic activity in pyramidal neurons (PNs) is modulated by a highly differentiated system of inhibitory interneurons, including PV, SST, vasoactive intestinal peptide (VIP), and cholecystokinin (CCK)-positive neurons (Klausberger und Somogyi 2008). These interneurons are crucial for controlling hippocampal oscillations, such as theta and gamma rhythms or sharp wave ripples, which in turn enable synchronization between the hippocampus and prefrontal cortex (Colgin 2011).

Furthermore, recent studies show that environmental and stress factors can cause structural and functional changes in the architecture of the hippocampus, underscoring its central role as a plastic, experience-dependent memory system (Albadawi 2025).

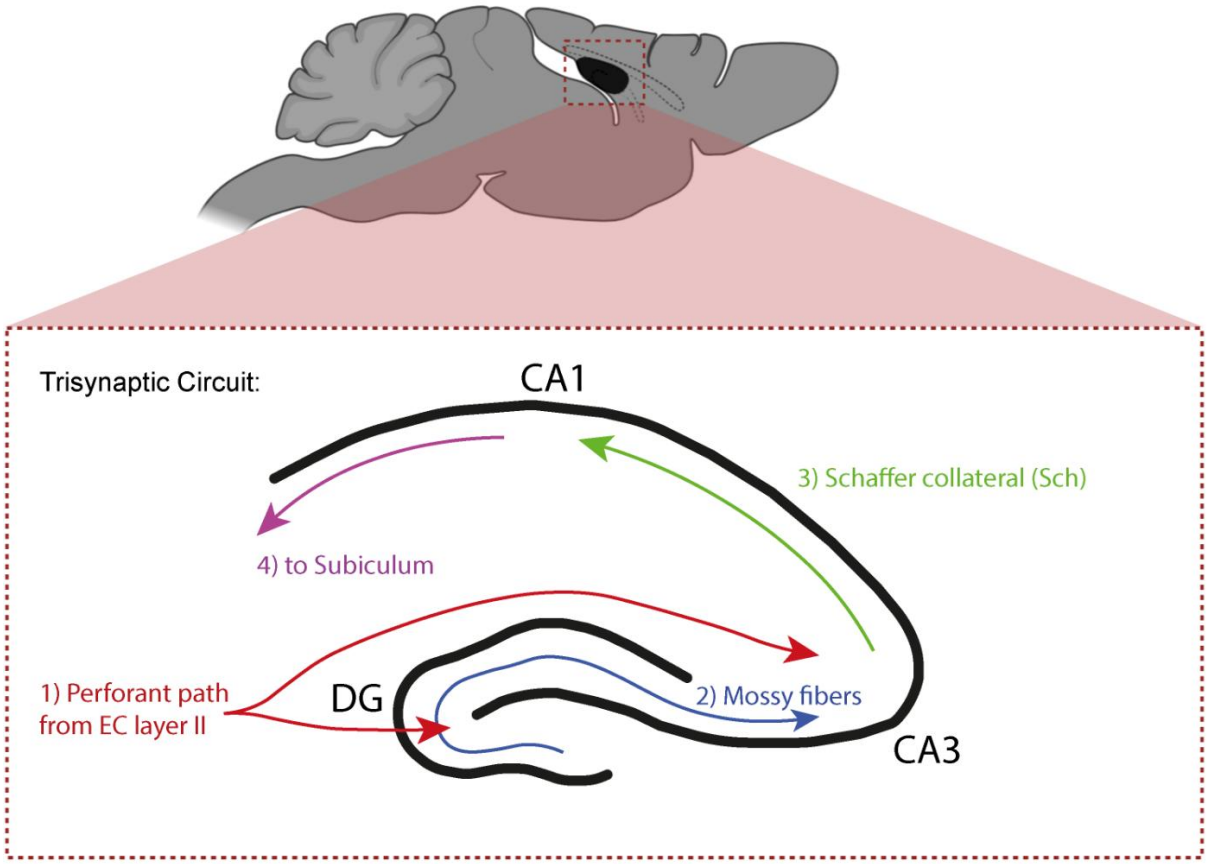

Figure 3. Schematic representation of the trisynaptic circuit in the rodent hippocampus. The excitatory input comes from neurons in layer II of the EC via the PP (1, red), which projects to the DG. From there, the axons of the granule cells form mossy fibers (2, blue), which target the PNs of CA3. The CA3 neurons in turn project via the Schaffer collaterals (Sch) (3, green) to the PNs of CA1. Finally, the output is transmitted from CA1 to the subiculum (4, purple) and then back to the EC and other cortical regions.

1.2.3. Interneurons in the CA1 Region and Network Modulation

In the brain, SST labels a large subpopulation of inhibitory interneurons (SST^+ INs), which are found primarily in the hippocampus and cortex. SST is a pleiotropic peptide hormone produced by neuronal, endocrine, and immunological cells that regulates numerous physiological processes. It acts as an endogenous inhibitor of central cellular functions such as secretion, metabolism, proliferation, and neuronal signaling. In the central nervous system, SST acts as a neurotransmitter and neuromodulator by modulating the efficiency of synaptic transmission and regulating neuronal activity (Liguz-Lecznar et al. 2022). They release SST together with GABA, whereas SST acts as a slower, longer-lasting inhibitor. Functionally, SST^+ INs, especially Martinotti cells, play a central role in regulating dendritic processing in pyramidal cells, controlling thalamocortical inputs, and regulating cortical oscillations. Therefore, they play a key role in maintaining inhibitory balance and controlling learning and memory processes.

It was first described in the year 1973 with the identification of a 14-amino acid peptide (SST-14), alongside which a longer peptide (SST-28) also exists in mammals (Brazeau et al. 1973; Pittaluga et al. 2021; Rai et al. 2015). Both are produced by the processing of pre-prosomatostatin. SST mediates its effects via five G protein-coupled receptors (SSTR1–5), which are expressed in various tissues and regulate different intracellular signaling pathways (Rai et al. 2015; Han et al. 2007; Pittaluga et al. 2021).

Disorders in the somatostatin system are correlated with cognitive deficits and neurological diseases such as Alzheimer's, schizophrenia, or depression. SST and SST^+ INs, are therefore a crucial between molecular signal regulation, network dynamics, and higher cognitive function (Sandoval und Witt 2024). Especially, oriens-lacunosum moleculare (O-LM) INs in the CA1 region of the hippocampus are a particularly well-studied subpopulation (Pelkey et al. 2017; Song et al. 2021). These cells function as central hubs in hippocampal networks. Pyramidal neurons receive their main glutamatergic inputs both from CA3 via the Schaffer collaterals (Sch), which mainly project into the *stratum radiatum* (SR), and from the entorhinal cortex via the temporoammonic pathway (TAP), which ends in the *stratum lacunosum-moleculare* (SLM). O-LM cells are located in the *stratum oriens* (SO) and project their axons into the SLM, where they inhibit the distal apical dendrites of the PNs. They therefore act as dendritic gatekeepers, selectively regulating the influence of entorhinal signals on the pyramidal cells (Pelkey et al. 2017; Pangalos et al. 2013; Leão et al. 2012).

In addition to this direct inhibition of PNs, O-LM cells also interact with a number of other interneurons. Through inhibitory projections to basket cells (BC), bistratified cells (BIC), radiatum-directed cells (RAD), neurogliaform cells (NGC), and other interneurons in the SLM, O-LM cells modulate the entire inhibitory system. This circuitry leads to context-dependent disinhibition of the PNs: if an inhibitory interneuron itself is inhibited, this results in a relative increase in excitatory inputs to the PNs. In this way, O-LM cells exercise a higher-level control function by not only directly filtering excitatory inputs, but also influencing the activity of other inhibitory circuits (Pelkey et al. 2017; Fernández-Arroyo et al. 2025).

The activity of O-LM cells is in return regulated by inhibitory interneurons, in particular by VIP-positive cells and interneuron-specific type 3 cells (IS-3). This circuitry leads to disinhibition of the PNs by downregulating O-LM activity, allowing entorhinal signals to act more freely on the distal dendrites (Turi et al. 2019; Tyan et al. 2014). In addition, O-LM cells receive significant long-range modulations from subcortical areas, in particular from the medial septum (MS) and the *nucleus incertus* (NI). While septal inputs rhythmically modulate the activity of O-LM cells in the theta range, determining their phase-dependent inhibition,

projections from the NI contribute to increasing the excitability of these cells (Klausberger et al. 2003; Hangya et al. 2009; Fernández-Arroyo et al. 2025; Lu et al. 2020).

As a result, a precisely balanced system of information retrieval and integration is created. O-LM cells determine the input of signals from the entorhinal cortex or CA3 into the CA1 circuits (Leão et al. 2012). In this way, they influence not only the synaptic plasticity, but also the rhythmic organization of hippocampal networks in the theta frequency, which is linked to learning and memory processes (Klausberger et al. 2003; Hangya et al. 2009; Siwani et al. 2018). Overall, it is clear that O-LM cells play a key role in controlling excitation and inhibition, contributing significantly to context- and phase-dependent information processing in the hippocampus (Figure 4) (Fernández-Arroyo et al. 2025).

Long-term potentiation (LTP) is considered a fundamental cellular mechanism for learning and memory and has been studied extensively, especially in the hippocampus. In this system, somatostatin-expressing interneurons play a crucial role, as they not only modulate synaptic plasticity locally, but also shape network dynamics in the vHPC – mPFC circuit. SST can induce LTP at excitatory synapses on SST^+ INs when applied externally, and blocking somatostatin-dependent signaling pathways leads to a significant reduction in hippocampal LTP (Racine et al. 2021). Based on this, it is hypothesized that SST^+ INs, by controlling GABAergic inhibition, represent a central hub for plasticity in the hippocampal-prefrontal circuits relevant for working memory (Artinian et al. 2019; Asgarihafshejani et al. 2022).

In the CA1 region, specifically in the O-LM, SST^+ INs inhibit the distal dendrites of pyramidal cells, therefore regulating the input of contextual information from CA3 and the entorhinal cortex (Leão et al. 2012). In this way, they control which information is transferred to the mPFC and integrated into working memory processes there (Spellman et al. 2015b). Ca^{2+} imaging studies show that CA1 SST^+ INs are active during learning processes, including contextual fear conditioning (cFC), and that their excitability increases after successful learning. This increased activity allows for fine-tuned control of pyramidal cell responses and facilitates the formation of stable memory traces (Artinian et al. 2019; Martinez-Losa et al. 2018; Siwani et al. 2018).

The role of SST^+ INs proves to be crucial for spatial working memory, which is based on the interaction of the vHPC and mPFC. Theta rhythms from the vHPC provide contextual information to prefrontal areas, while local interneuronal microcircuits in the mPFC, particularly through SST^+ INs, decide whether these signals are transformed into working memory representations (Spellman et al. 2015b; Abbas et al. 2018). If the SST^+ IN signaling is impaired, this information signaling is disrupted. Animal studies show that inhibition of CA1 SST^+ INs leads to hyperactivity of pyramidal cells and deficits in context-dependent memory

tasks (Abbas et al. 2018; Sigurdsson et al. 2010). This also affects spatial working memory pathways, where intact vHPC – mPFC communication is necessary to maintain context and location information across time intervals.

On a molecular level, the mammalian target of rapamycin complex 1 (mTORC1) signaling pathway in SST^+ INs is a key factor for plasticity in the vHPC − mPFC circuitry. Selective loss of mTORC1 activity in SST^+ INs leads to impairments in fear conditioning and context-dependent learning. Since mTORC1 is also essential for LTP at excitatory synapses on SST^+ INs, there is a significant correlation between somatostatin-dependent plasticity and working memory performance (Artinian et al. 2019; Asgarihafshejani et al. 2022; Racine et al. 2021).

In models of AD, O-LM SST^+ INs are impaired by the loss of cholinergic inputs, contributing to deficits in contextual and working memory. In addition, the number of somatostatin-expressing interneurons in the hippocampus and prefrontal cortex is reduced, leading to a disruption of the inhibitory balance, disturbed oscillation dynamics, and impaired vHPC – mPFC connectivity (Palop und Mucke 2016). However, experimentally stimulating SST^+ IN activity, for example by optogenetic activation or transplantation of interneuron precursor cells, can improve the synchronization of theta and gamma oscillations and stabilize cognitive performance (Martinez-Losa et al. 2018).

In summary, SST^+ INs in the vHPC – mPFC network act as gatekeepers that regulate the processing of contextual information and its integration into working memory processes. Their role in synaptic plasticity, oscillatory dynamics, and inhibitory control ensures the functional integration of hippocampal signals into prefrontal networks. Disruptions in this system lead to deficits in memory and cognitive function and are a key feature of neurodegenerative and psychiatric disorders (Sandoval und Witt 2024).

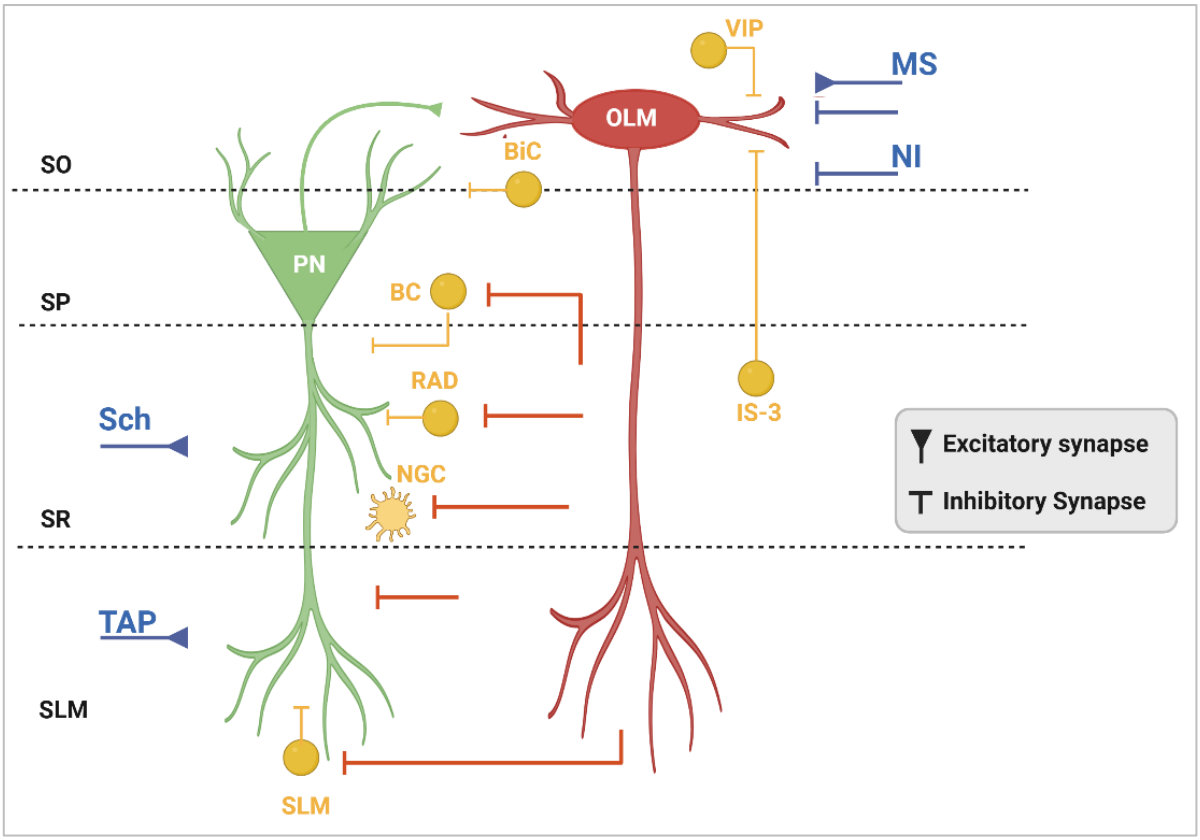

Figure 4. Schematic representation of the microcircuits in the hippocampus CA1, presenting the role of the INs of the O-LM. Pyramidal neurons (PNs, green) receive excitatory inputs from CA3 Schaffer collaterals (Sch) that terminate in the SR and from layer III of the entorhinal cortex via the temporoammonic pathway (TAP), which projects to the SLM. O-LM INs (red), located in the SO, extend their axons into the SLM to exert dendritic inhibition on the distal apical dendrites of PNs, thereby controlling entorhinal input. In addition, O-LM cells inhibit several classes of local INs − basket cells (BC), bistratified cells (BIC), radiatum-targeting cells (RAD), neurogliaform cells (NGC), and other SLM interneurons − resulting in disinhibition of the PN soma and proximal dendrites. O-LM activity itself is controlled by inhibitory inputs from VIP-expressing INs and IS-3, leading an additional level of disinhibition. Long-range modulatory inputs originate from the MS, which rhythmically controls O-LM activity in the theta range, and from the NI, which is responsible for excitatory control (figure adapted from Fernández-Arroyo et al. 2025).

1.2.4. Hippocampal-Prefrontal Connectivity and Functional Integration

The hippocampus and prefrontal cortex form a highly interconnected network that is crucial for the coordination of memory, executive functions, and flexible behavior. Anatomical tracing studies in rodents have demonstrated direct monosynaptic projections from the vHPC to the mPFC, along with reciprocal feedback from the prefrontal cortex via polysynaptic pathways involving thalamic and entorhinal relays (Hoover und Vertes 2007). This bidirectional connectivity enables the integration of context-rich hippocampal representations with the goal-directed and decision-relevant functions of the prefrontal cortex.

At the functional level, communication between the hippocampus and prefrontal cortex is strongly mediated by neural oscillations. In particular, theta (4–12 Hz) and gamma (30–80 Hz) rhythms play a central role in synchronizing activity in both regions. Studies in humans and animals have shown that theta phase coupling between the hippocampus and prefrontal cortex supports the integration of related memories and facilitates flexible retrieval strategies (Siapas et al. 2005; Jones und Wilson 2005a; Backus et al. 2016; Colgin 2016). Synchronization in the gamma range also contributes to the coordination of local computations within each structure and enables cross-frequency coupling, which may serve as a mechanism for selective information transfer (Colgin 2016).

The functional importance of this circuit has been highlighted in various cognitive areas. During spatial navigation, synchronized activity between the hippocampus and the prefrontal cortex is necessary to maintain working memory and update spatial representations (Jones und Wilson 2005b). In episodic memory, the prefrontal cortex exerts top-down control by directing retrieval from the hippocampus toward task-relevant information, supporting the dynamic recombination of memory traces (Preston und Eichenbaum 2013).

It is important to note that disruptions in this circuit are associated with cognitive impairments in neuropsychiatric and neurodegenerative diseases. For example, reduced synchrony between the hippocampus and prefrontal cortex has been observed in schizophrenia models, which is thought to contribute to deficits in cognitive flexibility (Sigurdsson et al. 2010) . Similarly, early disturbances in connectivity between the hippocampus and prefrontal cortex have been observed in mouse models of AD, where impaired oscillatory coupling correlates with deficits in executive functions and memory integration (Cunliffe et al. 2025; Wirt et al. 2021).

In summary, connectivity between the hippocampus and prefrontal cortex represents a critical substrate for the functional integration of memory and executive processes. Its dynamic coordination through oscillatory synchronization enables the flexible exchange of information necessary for adaptive behavior. Understanding the precise mechanisms of this network and how they change in disease states remains a central challenge for modern systems neuroscience.

1.3. Molecular Mechanisms Underlying Learning and Memory

Learning and memory processes are essentially based on molecular mechanisms that control synaptic plasticity in the hippocampus. Within the hippocampus, LTP and LTD are the most important pathways through which neural ensembles encode experience-dependent changes. The induction of LTP in CA1 PNs depends critically on glutamatergic signaling via NMDA receptors, which trigger Ca^{2+} influx and activate downstream effectors such as CaMKII and

PKA. These cascades facilitate the phosphorylation and insertion of AMPA receptors, strengthening excitatory synapses. LTD, on the other hand, involves the endocytosis or dephosphorylation of AMPA receptors, weakening synaptic efficacy and allowing for fine-tuning of communication between the hippocampus and prefrontal cortex (Azarnia Tehran et al. 2022; Park et al. 2014; Malenka und Bear 2004).

An important aspect of memory consolidation lies in the transition from early to late LTP, which requires de novo protein synthesis and transcriptional regulation. Transcription factors such as cAMP response element-binding protein (CREB) coordinate gene expression programs that provide plasticity-related proteins (PRPs) necessary for long-lasting synaptic modifications. The concept of synaptic tagging and capturing (STC) is particularly relevant in the hippocampus: Temporarily activated synapses can capture PRPs synthesized in response to strong activity, allowing distributed hippocampal networks to integrate temporally separated events (Wang et al. 2010).

The learning mechanisms of the hippocampus are not only regulated by excitatory pathways but also depend critically on inhibitory interneurons. Among these, somatostatin-expressing interneurons located in the SO layer of CA1 play a central role in controlling dendritic inputs and regulating the balance between excitatory and inhibitory inputs. By controlling the dendritic excitability of PNs, SST^+ interneurons shape the induction thresholds for LTP and LTD, thereby directly influencing the efficiency of information transmission along the hippocampus-prefrontal cortex axis (Lovett-Barron et al. 2014; Schulz et al. 2018). Dysfunctions of this inhibitory control, as described in AD models, contribute to abnormal oscillatory coupling and impaired working memory (Palop und Mucke 2016; Schmid et al. 2016).

Neuromodulators such as acetylcholine, dopamine, and norepinephrine further refine the plasticity of the hippocampus. For example, cholinergic inputs from the medial septum enhance theta rhythmicity, an important temporal structure underlying the synchrony between the hippocampus and prefrontal cortex. Dopaminergic signals, in turn, stabilize LTP and promote the persistence of memory traces, linking synaptic changes to motivational states (Dannenberg et al. 2015; Király et al. 2023; Takeuchi et al. 2016). Structural changes, including the remodeling of dendritic spines and the reorganization of the actin cytoskeleton, complement these signaling cascades to ensure long-term stabilization of connectivity between the hippocampus and prefrontal cortex. Proteases such as calpain modulate this process by cleaving elements of the cytoskeleton and facilitating the incorporation of AMPA receptors (Baudry und Bi 2024).

In the context of AD-like pathology, Aß and tau pathologies disrupt these molecular cascades, leading to impaired NMDA receptor signaling, reduced CREB-dependent transcription, and loss of dendritic spines. SST^+ interneurons are particularly vulnerable, undergoing selective dysfunction and contributing to disrupted hippocampal-prefrontal cortex oscillations, thereby exacerbating deficits in spatial working memory (Schmid et al. 2016; Palop und Mucke 2016).
In summary, learning and memory in the hippocampus arise from a complex interplay of excitatory and inhibitory synaptic plasticity, neuromodulatory inputs, and structural and epigenetic modifications. The dynamic integration of these molecular processes is crucial for stabilizing communication between the hippocampus and prefrontal cortex and ensures adaptive cognitive performance. Understanding how these mechanisms fail in disease models provides important insights into the pathophysiology of memory disorders and may reveal new targets for intervention.

1.4. Aim of the Study

The monosynaptic, glutamatergic projections from the vHPC to the mPFC are well known to play an important role in regulating anxiety, processing context, and guiding decision-making. However, recent studies show that this connection is more complex than previously thought. Here, GABAergic pathways are different from local interneurons because they can directly influence prefrontal circuits across long distances. Similar types of neurons have been described in hippocampal and entorhinal networks and there is also evidence that the mPFC itself sends long-range inhibitory projections back to the hippocampus. This suggests that hippocampal-prefrontal communication is not only driven by excitatory input followed by local inhibition, but also by direct inhibitory pathways.
The aim of this thesis is to investigate potential direct projections from the vHPC to the mPFC. This idea is especially important in AD. The mPFC is one of the regions that shows early impairment, including functional disconnection within the default mode network, synaptic changes, and early accumulation of amyloid and tau pathology. The possibility that LRIPs from the vHPC shape prefrontal activity, network rhythms, and working memory points to a clear research gap with major relevance for understanding early cognitive decline in AD.
Therefore, the aim of this study is to investigate how connectivity between the hippocampus and prefrontal cortex changes under Alzheimer's-like conditions and how these changes contribute to impairments in (spatial) working memory.
In a first step, anatomical mapping of hippocampal inputs to the prefrontal cortex will be performed in SST-Cre, SST-Cre::APP/PS1, and Chrna2-Cre mice. By combining anterograde

viral tracings with cell type-specific promoters and postmortem immunohistochemistry, for later investigation whether inhibitory projections originating from these defined interneuron populations exhibit structural changes under AD-like pathology. This approach will provide a detailed picture of cell type-specific connectivity changes in the hippocampal-prefrontal circuitry.

In a second step, I will investigate the causal role of these pathways for spatial working memory performance. Chemogenetic silencing and activation of hippocampal projections to the prefrontal cortex will be performed in wild-type and APP/PS1 mice, as well as in the mentioned Cre driver lines with and without APP/PS1 background. This strategy will allow to investigate the connectivity deficits identified in the Alzheimer's model and test whether restoration of projection activity can prevent synaptic dysfunction and improve behavioral outcomes.

As an additional preliminary step, a pilot study will be performed using a treadmill-based head fixation setup to establish a reliable behavioral paradigm for spatial working memory under imaging conditions. In this setup, APP/PS1 and WT mice will be compared directly to assess whether genotype-dependent network differences are observable. The treadmill design also enables stable recordings of neural population activity during task performance, providing the methodological basis for *in vivo* Ca^{2+} imaging experiments.

Taken together, these experiments will incorporate structural, functional, and causal evidence of connectivity between the hippocampus and prefrontal cortex. This approach will help clarify how Alzheimer's-related pathology affects these circuits and the role of targeted manipulations in restoring memory function.

2. Materials & Methods

2.1. Transgenic Mice

Animals were either housed single or in groups of up to five mice in individually ventilated cages (IVCs) under specific-pathogen-free (SPF) conditions. The housing environment was maintained at 22°C with 40% humidity, and a 12-hours light/dark cycle (lights on at 6:00 am, off at 6:00 pm). Mice were separated by sex, food and water were provided ad libitum. Throughout the study, the well-being of the animals was a primary concern, and all measures to ensure proper welfare were undertaken. Furthermore, the principles of the 3Rs (Replacement, Reduction, and Refinement) were continuously applied to minimize animal usage and distress wherever possible. Animal holding, breeding and experimentation were carried out in accordance with institutional guidelines, German federal law, directives of the European Union and approved by the "Landesamt für Natur, Umwelt und Verbraucherschutz Nordrhein-Westfalen" (LANUV). All animals were handled in full compliance with the German Animal Welfare Act and the Animal Welfare Ordinance for Laboratory Animals; consequently, no avoidable pain, distress or injury was inflicted.

2.1.1. APP/PS1 Mice

B6.Cg-Tg(APPswe,PSEN1dE9)85Dbo/Mmjax mice (MGI ID: 3611279; commonly referred to as "APP/PS1"; MMRRC stock number 034832, The Jackson Laboratory) serve as a key model for studying beta amyloidosis and Alzheimer's disease (Jankowsky et al. 2004). These animals carry two transgenes: a chimeric mouse/human amyloid precursor protein (Mo/HuAPP695) featuring the Swedish K594M/N595L mutation under control of the mouse prion protein promoter (PrnP), and a presenilin 1 gene (PS1) harboring an exon 9 deletion. Both transgenes reside at a single genomic insertion site, so they are inherited as one locus. Because of their increased Aß production, these mice develop progressively extracellular amyloid-beta deposits with advancing age, and female mice tend to exhibit more pronounced Aβ-plaque buildup at earlier ages compared to males (Jiao et al. 2016). In this dissertation, only heterozygous mice (APP/PS1) or wild-type littermates (WT) were used, given that the homozygous condition is associated with a more severe phenotype.

2.1.2. SST-Cre Mice

B6N.Cg-Ssttm2.1(cre)Zjh/J mice (MGI ID: 5509174; stock number 018973, The Jackson Laboratory) express Cre recombinase (IRES-Cre-pA cassette) in the 3' UTR of the somatostatin locus (Taniguchi et al. 2011). These mice are typically used for genetic targeting of specific interneuron populations in the central nervous system. SST-Cre mice were crossbred to APP/PS1 mice and only offspring heterozygous for the Cre transgene was used for experiments due to the partial knockout of the endogenous somatostatin protein resulting from the insertion method of the transgene.

2.1.3. Chrna2-Cre Mice

Tg(Chrna2-cre)1Kldr mice (MGI ID:87885) are a transgenic mouse line that expresses Cre recombinase under the control of the Chrna2 (nicotinic acetylcholine receptor α2 subunit) promoter*13*. These mice are used for genetic targeting of specific neuronal populations characterized by *Chrna2* expression, particularly by enabling selective targeting of O-LM interneurons (Leão et al. 2012). Mutation details: A construct (composed of Cre recombinase with a nuclear localization signal, SV40 polyadenylation sequence, and an Frt-Kanamycin/neo-Frt cassette) was introduced into the ATG site in exon 2 of the Chrna2 gene in a bacterial artificial chromosome (BAC RP23-48P22) by recombing in bacterial cells. Modified BAC DNA was purified and injected into mouse pronuclei to produce transgenic mice. One founder line showed Cre expression in cells that express the CHRNA2 protein (Leão et al. 2012). These mice were crossbred to APP/PS1 mice and only offspring heterozygous for the Cre transgene was used for experiments.

2.2. Surgical Procedures

In one set of experiments aimed at behavioral analysis of circuit manipulation, long-range inhibitory neurons in SST- and Chrna2-Cre mice were targeted using bilateral intracerebral injections of AAVs containing loxP-flanked genes of fluorescent reporter proteins, optogenetic or chemogenetic proteins (see section 2.2.1). This approach allowed selective manipulation of defined interneuron populations to examine their roles in circuit function during behavior later (see section 0). In a separate experimental cohort, neuronal activity was recorded in APP/PS1 and WT animals by expressing the fluorescent Ca^{2+} indicator GCaMP in the mPFC using unilateral AAV-mediated expression in excitatory (pyramidal) neurons using the CamKIIα promoter, followed by implantation of a prism (see section 2.2.2).

2.2.1. AAV-Injection

The analgesic tramadol was provided *ad libitum* in the drinking water (0.1 mg/ml), starting 24 h before surgery and continuing for 3-days post-operatively. On the day of the surgery, anesthesia was induced with a Ketamine/Xylazine (0.13/0.01 mg/g; i.p.) mix, after which the mouse was placed on the heating pad (7 × 7 cm) to maintain the body temperature at 37 °C (Stoelting Co., Wood Dale, Illinois, USA). A few minutes later the depth of anesthesia was confirmed by the absence of the hind-paw withdrawal reflex. The head was then positioned horizontally in a stereotaxic frame and immobilized with a bite bar and bilateral ear bars inserted into the external auditory canals (Narishige, Tokyo, Japan). Immediately after induction of anesthesia, eye cream (Bepanthen® Augen- und Nasensalbe, Bayer Vital GmbH, Leverkusen, Germany) was applied to prevent corneal drying.

A midline scalp incision was made from rostral to caudal with surgical scissors (Fine Science Tools (FST), Foster City, USA) while the skin was gently tensioned. The wound edges were retracted with a forceps (FST, Foster City, USA) and small rolled paper swabs were placed beneath the margins. The periosteum covering the skull was removed with a bone scraper (FST, Foster City, USA) to create a smooth surface and fully expose the *calvarium*. The stereotaxic zero point was set at Bregma. Using an XYZ micro-manipulator (Luigs and Neumann, Ratingen, Germany) and coordinates from the Paxinos and Franklin mouse brain atlas (2001), the craniotomies were performed for vHPC (coordinates relative to Bregma: AP −3.5 mm, ML ±3.7 mm, DV −3.2 mm) (

Table ***1***). The injection site was marked with a fine needle, and the craniotomy was performed with a high-speed drill (OmniDrill35; World Precision Instruments, Sarasota, FL, USA). Bleeding was controlled with medical sponges (i.e., Sugi® and SMI Spon®).

To induce the expression of the desired transgene, an AAV with the cloned cDNA construct was stereotactically injected into the brain of anesthetized mice. To selectively manipulate long-range inhibitory neurons in the behavior experiments, a Cre-dependent AAV encoding an inhibitory or excitatory DREADD (Designer Receptors Exclusively Activated by Designer Drugs) (Table 2) was injected into the CA1 region of the vHPC of SST-Cre and Chrna2-Cre mice. DREADDs are chemogenetic tools that enable reversible and cell-type-specific inhibition or activation of neuronal activity upon systemic administration of a synthetic ligand such as Clozapine N-oxide (CNO) or Compound 21 (C21) (Roth 2016). These receptors are based on artificially produced muscarinic G protein-coupled receptors (GPCRs) that have lost their sensitivity to endogenous acetylcholine but can be selectively activated by the synthetic ligand.

GPCRs represent the largest family of membrane receptors and are essential for the transmission of extracellular signals into intracellular responses. They are characterized by seven transmembrane helices and undergo conformational changes upon ligand binding that activate heterotrimeric G proteins. This activation involves the exchange of GDP for GTP on the Gα subunit, leading to the dissociation of Gα-GTP from the Gβγ dimer. Both components then regulate downstream effectors, including enzymes such as adenylyl cyclase or phospholipase C (PLC), as well as ion channels. This signaling cascade leads to the formation of second messengers (e.g., cAMP, IP_3, DAG, Ca^{2+}), which amplify the signal within the cell. The signal is terminated by the intrinsic GTPase activity of Gα and by receptor desensitization via phosphorylation and arrestin binding (Pierce et al. 2002; Rosenbaum et al. 2009; Weis und Kobilka 2018).

In this context, two important DREADDs have been used: the excitatory hM3Dq receptor, which couples to *Gq* proteins and induces the activation of PLC, the release of intracellular Ca^{2+}, and the depolarization of neurons, and the inhibitory hM4Di receptor, which couples to *Gi* proteins and leads to a reduction in cAMP levels, activation of GIRK (G protein-coupled inwardly rectifying potassium) channels, and suppression of neuronal activity. By enabling bidirectional and highly specific modulation of neural circuits *in vivo*, DREADDs offer a versatile experimental approach for analyzing causal relationships between defined cell populations and behavior (Armbruster et al. 2007; Urban und Roth 2015; Roth 2016).

The virus solution was drawn up into a 10 µl Hamilton syringe with a 34G cannula (World Precision Instruments, Sarasota, FL, USA). The injection rate and volume were programmed on the Ultra Micro Pump Controller (World Precision Instruments, Sarasota, FL, USA), while a motorized micromanipulator (Luigs & Neumann, Ratingen, Germany) positioned the cannula tip with micrometer precision in the anterior-posterior (AP), medio-lateral (ML) and dorso-ventral (DV) axes relative to Bregma (Table 1). The cannula was slowly lowered into the dura to the desired depth and 1 µl of virus was injected bilaterally at 100 nl/min. After application, the cannula remained in the tissue for around ten minutes to prevent reflux.

Table 1. Coordinates are given relative to Bregma, based on the Paxinos & Franklin mouse brain atlas (2001). Each hemisphere received 1 µl of the respective viral vector.

Coordinates	vHPC	mPFC
AP	− 3.5 mm	+ 1.8 mm
ML	± 3.7 mm	± 0.3 mm
DV	− 3.2 mm	− 1.0/ − 0.8 mm

Finally, the scalp was closed with surgical wire (Vicryl™ Plus 4-0 TF plus 13mm 1/2c, Ethicon®, Norderstedt, Germany). To ensure consistent manipulation of neural circuits, all

animals used for behavioral experiments received bilateral viral injections, as many behaviors depend on coordinated activity across both sides of the brain. As already mentioned below tramadol was provided *ad libitum* in the drinking water (0.1 mg/ml) for 3-days post-operatively.

Table 2. AAV vectors used for stereotactic injections.

Designation	ROI	Volume	Titer
AAV1.CAG.FLEX.tdTomato	vHPC	1000 nl	1×10^{13} vg/mL
AAV2.hSyn.DIO.hM3D(Gq).mCherry	vHPC	1000 nl	6×10^{12} vg/mL
AAV2.hSyn.DIO.hM4D(Gi).mCherry	vHPC	1000 nl	5×10^{12} vg/mL
AAV2.hSyn.hM4D(Gi).mCherry	vHPC	1000 nl	5×10^{12} vg/mL
pAAV.hSyn.DIO.mCherry	vHPC	1000 nl	4×10^{12} vg/mL
AAV (pAAV.retro.hSyn.DIO. EGFP)	mPFC	1000 nl	7×10^{12} vg/mL
AAV1.CamKII.GCaMP6f.WPRE.SV40	mPFC	1000 nl	1×10^{13} vg/mL

2.2.2. Prism-Assisted Cranial Windows in mPFC

In a separate cohort of mice (APP/PS1 mice), GCaMP6f, a genetically encoded calcium indicator, was expressed in PNs of the mPFC using a CaMKIIα promoter-driven AAV (AAV1.CamKII.GCaMP6f.WPRE.SV40, Addgene, Watertown, USA) (Table 2). This was followed by implantation of a 1.5 × 1.5 mm prism for *in vivo* Ca^{2+} imaging (2.4). GCaMP imaging was performed in unilaterally-injected mice in the mPFC (coordinates relative to Bregma: AP +1.8 mm, M/L ±0.3 mm, DV −1.0 mm) (see section 2.2.1).

Before the craniotomy, windows to access the mPFC, consisting of a microprism and a coverslip, were prepared. Microprisms (1.5 × 1.5 × 1.5 mm, Tower Optical, Norwalk, Connecticut, USA) were glued to a rectangular cover slip (4 mm × 3 mm) using UV-curable adhesive (Fast Curing Optical Adhesive 1 oz., Norland Products Inc., Cranbury, NJ, USA) and a UV diode laser (Omicron Laserage, OMICRON electronics GmbH, Austria). Fixation was achieved through targeted UV irradiation (365 nm) controlled by Omicron software (OMICRON electronics GmbH, Klaus, Austria) to ensure a stable and precise connection between the prism and cover glass (Figure 5a). The implantation of the microprisms was performed on the same day of AAV injection in adult APP/PS1 and WT mice eight weeks prior to *in vivo* imaging. Mice received tramadol *ad libitum* in the drinking water (0.1 mg/ml) 24 hours before surgery and were subsequently anaesthetized by administration of Ketamine/Xylazine (0.13/0.01 mg/g; i.p.). After reaching surgical tolerance, the mouse was placed in a stereotactic frame, while body temperature was maintained at 37 °C by a heating pad (Stoelting Co., Wood Dale, Illinois, USA). Under surgical conditions, the skin on top of the skull was first disinfected with 70% ethanol and then removed with surgical scissors. A rectangular piece (4 mm × 3 mm) of the skull spanning the sagittal sinus from ML: −2.0 mm of

the left hemisphere to ML: +2.0 mm of the right hemisphere above the mPFC (AP +1.8 mm) was removed using a dental drill (OmniDrill35; World Precision Instruments, Sarasota, FL, USA) (Table 1) (Figure 5). Drilling the skull bone above the sagittal sinus was carried out extremely careful to prevent puncturing the sinus. After removal of the skull bone potential bleedings were stopped using gel-foam (SMI Spon Gelatineschwamm Standard 80×50×10 mm, Praxisdienst GmbH, Longuich, Germany). The dura was carefully incised to enable the implantation of the microprism between the two hemispheres (Figure 5b). To keep the brain surface moist, it was frequently rinsed with sterile saline. The glass coverslip with the microprism was inserted into the fissure between the two hemispheres and glued to the skull bone with dental cement (GC Cooperation, Tokyo, Japan). A head bar (Luigs & Neumann, Ratingen, Germany) for head-fixation during *in vivo* imaging was mounted alongside the cranial mPFC-window with dental cement. For post-surgery analgesia, tramadol was given for 3 days in the drinking water *ad libitum* (0.1 mg/ml) and Carprofen (5 mg/kg) applied subcutaneously shortly after the surgery to prevent swelling of the brain.

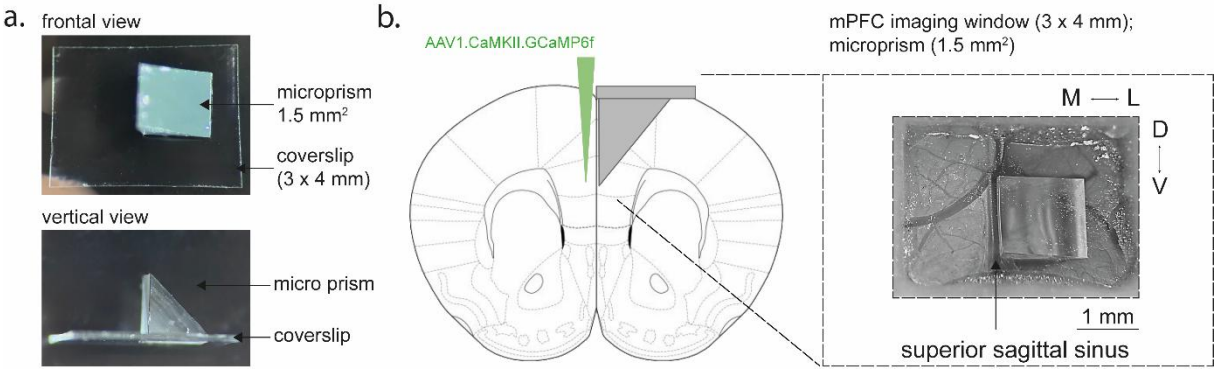

Figure 5. Schematic representation of the stereotactic placement of the microprism (1.5 mm²) for *in vivo* Ca^{2+} imaging in the mPFC. a. Microprism mounted on a cover slip. Frontal view: The microprism is positioned at the center of a rectangular glass coverslip (3 × 4 mm). The vertical orientation reveals the triangular shape of the microprism and its attachment to the coverslip. The prism was mounted using UV-curable adhesive and secured in place with a diode laser (365 nm) for precise alignment. **b.** After injection of an AAV1.CaMKII.GCaMP6f, the microprism attached to the 3 × 4 mm coverslip was inserted between the two hemispheres to access the contralateral mPFC in a 90 ° imaging angle. Right: Macroscopic image of the implanted mPFC window with clear position relative to the midline (*superior sagittal sinus*) and orientation.

2.3. Behavior Experiments

Established behavioral test procedures were used to investigate the relevance of inhibitory projections from the vHPC to the mPFC for cognitive and exploratory behaviors in mice. These included the open field (OF) test, the novel object recognition test (NOR), the y-maze test, and a cFC paradigm.

2.3.1. Open Field

An open field test was performed in a 50 × 50 × 50 cm acrylic box under dim lighting (20 LUX (lx)) to assess both exploratory activity (e.g., total distance traveled) and anxiety-like behaviors (e.g., time spent in the center vs. border). Here, the central zone was defined as a square located in the middle of the arena, measuring 20 × 20 cm, resulting in a surrounding border zone of 15 cm width on each side (

Figure **6**). To minimize visual distractions, the apparatus was encircled by a white room divider, hiding the experimenter and equipment from the mouse's view. Lighting in the room was kept low, provided by an overhead illumination. An overhead camera, mounted on a metal beam at the top of the enclosure, recorded the mice during the test. 30-45 minutes before the experiment started, mice received intraperitoneally 3 µg/g CNO or C21 solved in 1 % DMSO and 0.9 % NaCl (0.4 µg/µl) to activate the DREADD. Depending on the experimental batch, different control conditions were used: (i) control animals with DREADD injection received an intraperitoneal injection of saline, or (ii) animals with control virus (AAV.hSyn.DIO.mCherry) received an injection of C21.

Mice were allowed to explore the open field for at least 10 minutes. Before and after each session, the floor of the arena was cleaned with 70% ethanol and water, then dried with a paper towel. The behavior of the animals was recorded with an overhead video (software: IDS peak Cockpit 1.5.0.0; camera: UI-3140CP-C-HQ Rev.2 (IDS Imaging Development Systems GmbH; Germany)). After each session, the arena was cleaned with 70% ethanol and water to eliminate olfactory cues.

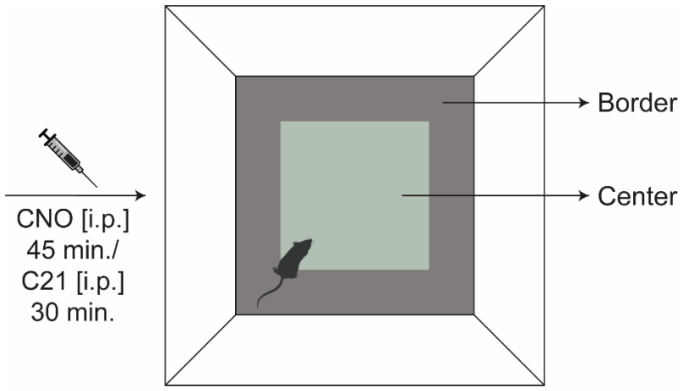

Figure 6. Schematic representation of the OF setup used to assess exploratory behavior and anxiety-like responses. Mice received C21 (30 min.) or CNO (45 min.) (i.p.) prior to testing and explored the arena for 10 minutes. The center and border zones are indicated.

2.3.2. Novel Object Recognition

The novel object recognition test (Figure 7) was conducted the next day in the same open field arena, under identical lighting conditions, and in the same room as described in section 0 (Figure **6**). Here, to guide the mice through the arena and support their spatial awareness, visual cues were attached to the walls in the arena.

During the acquisition phase, two identical, familiar objects (cell culture bottles with blue medium and red lids) were placed in the corners of the arena. Each mouse had 5 minutes to explore both objects. This procedure was repeated twice with an interval of 15 minutes between each repetition, resulting in a total exploration time of 15 minutes.

In a 2-hour session, after a break of 2 hours, the experimental mice received an intraperitoneal injection of CNO (45 min.) or C21 (30 min.) before the start. Again, depending on the experimental batch, different control conditions were used: (i) control animals with DREADD injection received an intraperitoneal injection of saline, or (ii) animals with control virus (c) received an injection of C21. In this session, one cell culture bottle (approx. 15 cm high, filled with brown substrate and closed with a yellow lid) was replaced with one of the familiar objects and used as the first “novel” object. The animals were allowed to explore these objects for 5 minutes.

After a delay of 24 hours, on the second day, one of the two familiar objects was replaced by a second new object- a cylindrical aluminum can of comparable size. Again, prior to this session, the animals received CNO (45 min.) or C21 (30 min.) intraperitoneally before the start of the test.

After each session, both the arena and the objects were cleaned with 70% ethanol, then rinsed with water and thoroughly dried to eliminate olfactory cues.

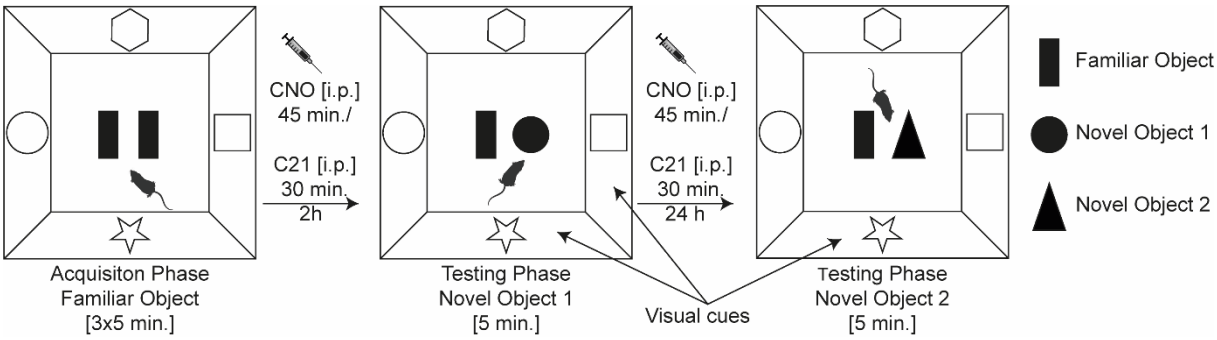

Figure 7. Schematic representation of the NOR test. Recognition memory was assessed by calculating the DI based on the recorded exploration time of individual objects. On day 1, mice were exposed to two identical familiar objects during the acquisition phase. After 2 hours, one familiar object was replaced with a novel object (novel object 1) for the first test phase. On day 2, following a 24-hour delay, a second novel object (novel object 2) replaced one of the previously explored objects. Mice received CNO (45 min.) or C21 (30 min.) (i.p.) before each testing phase.

2.3.3. Y-Maze

There are multiple variants of the y-maze, each tailored to assess different types of memory (Figure 8). In this study, a version designed to evaluate mPFC-dependent spatial working memory – requiring both egocentric and allocentric navigation – was used. The maze itself features three corridors arranged in a Y-shape (each arm 30 cm long), each separated by a 120° angle. At the far end of each arm, distinct geometric cues were affixed to facilitate navigation and orientation of mice in the arena. Mice received C21 intraperitoneally 30 minutes before the start and were introduced into the start-arm of the y-maze and permitted to explore freely for a total of five minutes (Figure 8, sample phase). After the acquisition session, mice were placed in their home cages for 60-minute delay (Figure 8, delay phase). The animals were then reintroduced to the maze for an additional five-minute test session, during which they could freely explore the two accessible arms now (Figure 8, choice phase). After each session, the arena was cleaned with 70% ethanol, then rinsed with water and thoroughly dried to eliminate olfactory cues.

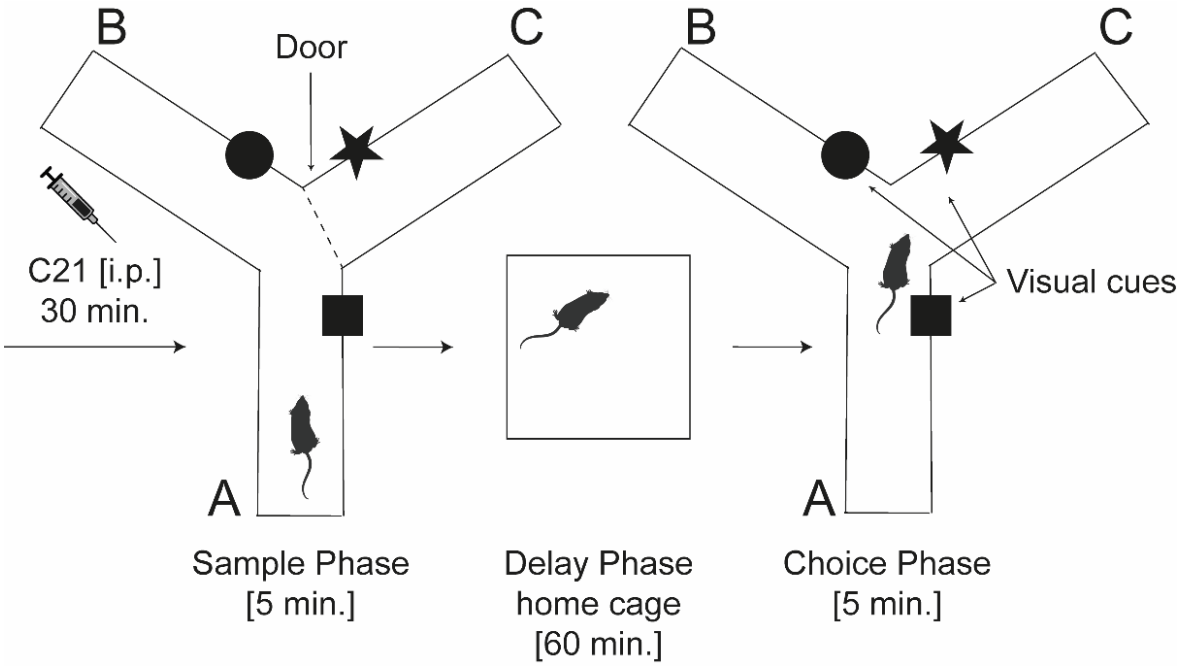

Figure 8. Schematic illustration of the y-maze test for testing spatial working memory. 30 min. before the start, the animals received C21 (i.p.). Sample phase (5 min): Mouse starts in arm A; arm C is closed; arm B is open. Delay phase (60 min): Stay in home cage. Choice phase (5 min): all arms open; preference for the previously unknown arm C serves as a memory measure. Geometric visual cues on both sites of the arms support orientation.

2.3.4. Contextual Fear Conditioning

Before contextual fear conditioning was performed, each mouse was handled on five days for 10 minutes. The experiment was conducted in a custom-built box (21.5 × 20.0 × 40.0 cm) with a metal grid at the bottom (Figure 9). Mice were first allowed to explore the context for two minutes, then three foot shocks of 0.75 mA for 2 s were applied via the metal grid with one-minute intervals. After the third shock the mouse was left in the box for another minute and finally returned to the home cage. The memory retrieval was performed 24 hours later. The mice were placed back into the conditioned context for 5 minutes. Mice received CNO or C21 intraperitoneally before each start and were introduced into the arena and allowed to explore freely for a total of five minutes animals. Again, depending on the experimental batch, different control conditions were used: (i) control animals with DREADD injection received an intraperitoneal injection of saline, or (ii) animals with control virus (AAV.hSyn.DIO.mCherry) received an injection of C21.

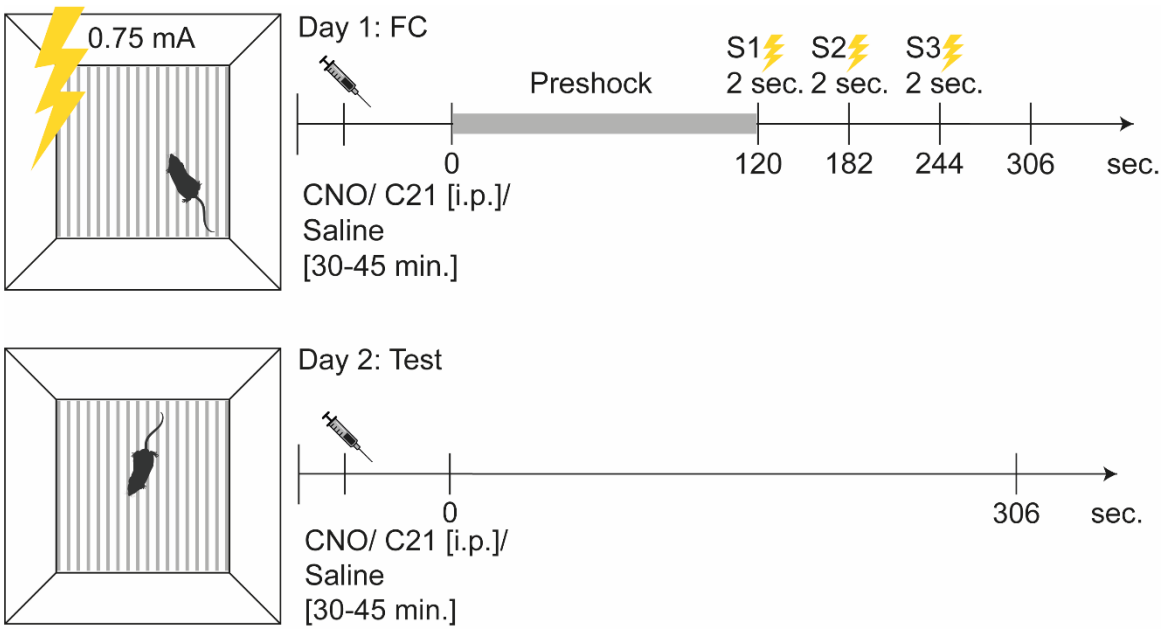

Figure 9. Schematic representation of the cFC paradigm. On day 1, acquisition phase, mice received three 0.75 mA foot shocks (2 s duration, 1-minute intervals) after a 2-minute exploration phase, followed by a 1-minute post-shock period. On day 2, memory retrieval was assessed by re-exposing the animals to the same context for 5 minutes without shocks. Mice received C21 (30 min.), CNO (45 min.) or saline (i.p.) before each session.

2.4. *In Vivo* Two-Photon Imaging

The two-photon effect is a nonlinear optical phenomenon in which an atom or molecule simultaneously absorbs two lower-energy photons, causing it to transition from its ground state to a higher-energy excited state. Upon returning to the ground state, it emits photons of higher energy than those originally absorbed. This is the basic working principle of two photon microscopes. Because of the non-linearity of the process, the signal depends on the second power of the light intensity ($S \propto I^2$). The signal also depends on the spatio-temporal concentration of the excitation light (Figure 10). To achieve spatial concentration, a high numerical aperture (NA) objective and a focused laser is used where the intensity of the light is highest in the vicinity of the focus and drops off quadratically with distance above and below. As a result, fluorophores are excited almost exclusively in a tiny diffraction-limited focal volume. To achieve the temporal concentration lasers capable of generating 'Ultrashort'pulses (femto second) with corresponding high peak intensities are used. For laser pulses of width (τ) occurring at a rate (f R), the signal is enhanced by a factor of $\frac{1}{(\tau\, f\, R)\, n-1}$ compared to continuous-wave illumination, where *n* is the number of photons involved in the elementary process.

Due to its optical sectioning capability and reduced phototoxicity, two-photon excitation microscopy enables high-resolution, three-dimensional contrast and resolution in deep tissue imaging, making it particularly well-suited for *in vivo* recordings of neuronal activity using

genetically encoded calcium indicators such as GCaMP during physiological and behaviorally relevant processes (Svoboda & Yasuda 2006; Helmchen & Denk 2005).

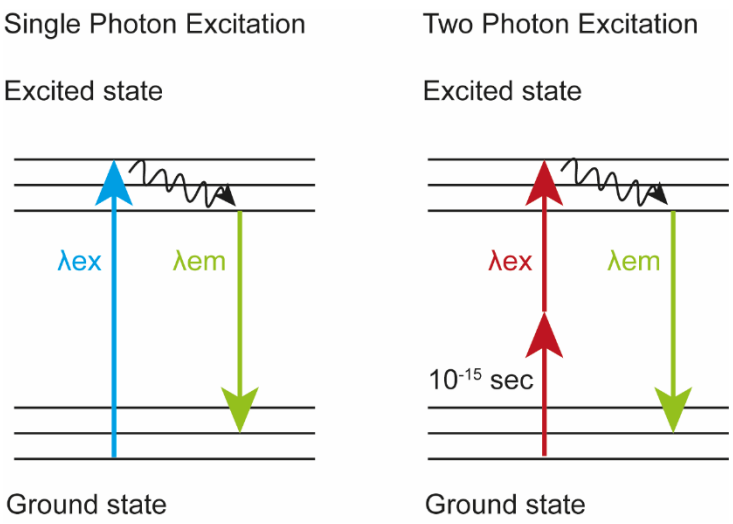

Figure 10. Schematic illustration of the Jablonski diagram. In single-photon excitation, an electron is transferred from its ground state to an excited state by absorbing a single photon with sufficient energy (excitation wavelength: λ_{ex}). After a brief period in the excited state, the electron returns to the ground state, emitting a photon with a longer wavelength (emission wavelength: λ_{em}). In contrast, in two-photon excitation, the electron is raised to the excited state by the almost simultaneous absorption of two photons, each with half the energy (twice the wavelength of single-photon excitation). The time span between the two absorption events is in the range of ~10^{-15} seconds. Here, the transition back to the ground state results in the emission of a photon with wavelength λ_{em}. Two-photon excitation enables localized excitation in the focus volume and is particularly advantageous for deep tissue imaging with reduced phototoxicity and scattering.

In this project, two-photon microscopy was used as an imaging method in an exploratory pilot study to systematically record neural activity in the mPFC of AD mice (APP/PS1) during a learning task for the first time. The aim was to document dynamic patterns of activation in the mPFC under AD-like conditions and to identify differences between genotypes.

The experiments were performed using a commercial two-photon microscope (Bergamo II, Thorlabs) equipped with a pulsed femtosecond laser (excitation wavelength 920 nm), a resonant scanner, and a non-scanned detection path with spectral separation and GaAsP photomultipliers (PMT) (Figure 11). Mice were previously virus-transduced with a GCaMP to visualize neural activity patterns. During imaging, the animals were fixed on a motorized treadmill and performed a spatial learning paradigm. Activity in the mPFC was continuously recorded during different phases of the task.

This pioneering work served to establish the technical feasibility and methodological basis for a more in-depth functional characterization of hippocampal-prefrontal interactions in the AD

mouse model. The data obtained form the basis for future studies in which the role of altered cortical activity patterns in AD-typical cognitive deficits will be further elucidated.

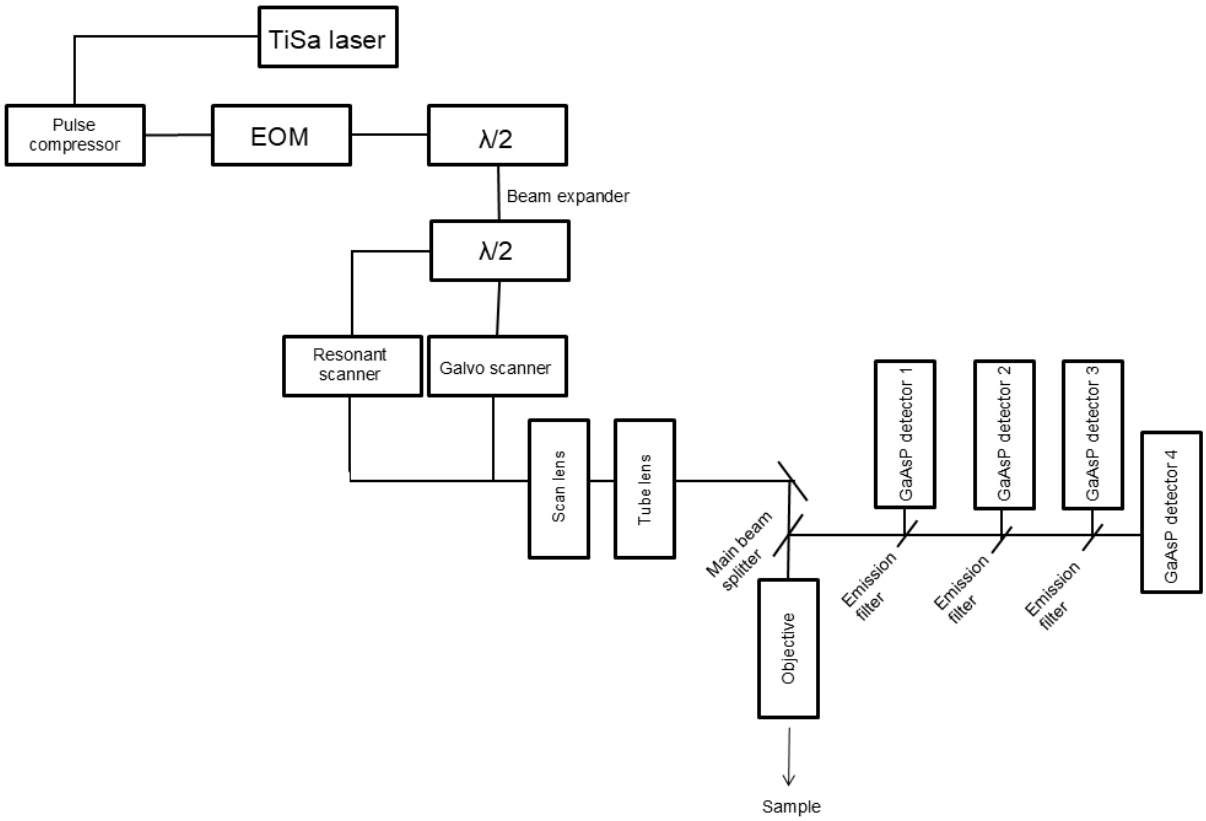

Figure 11. Schematic illustration of the two-photon microscope featuring spectral resolution in both excitation and emission pathways. A tunable Ti:sapphire (Ti:Sa) femtosecond laser provides the excitation. The beam first passes through a pulse compressor and then enters an electro-optic modulator (EOM) for fast blanking, which helps turning the light off outside the scan field to reduce phototoxicity. The first λ/2 plate on the beam path helps to regulate the laser power. Then the beam passes through a beam expander which increases the beam diameter to fill the objective's back aperture to have a uniform illumination. A second λ/2 plate then routes the beam to either the galvanometric scanner or the resonant scanner. Then a scan lens and a tube lens assembly help the beam reach the objective pupil, and the objective focuses the beam into the sample. A main dichroic beamsplitter separates fluorescence from the excitation path and directs it to four GaAsP PMTs. Each PMT is preceded by an emission band-pass filter that defines its detection wavelength range (figure credit from Microscope Facility, DZNE Bonn).

2.4.1. Linear Treadmill

The linear treadmill was equipped with a 360-centimeter-long belt (Figure 12). For treadmill preparation, fabric belts (width: 65 mm) (Laufbandstoff, Luigs und Neumann, Ratingen, Germany) were cut into 360 cm segments. Spatial cues were applied every 60 cm along each segment using a hot glue gun and white tape (Rollenpflaster Leukosilk®, Carl Roth GmbH & Co. KG, Karlsruhe, Germany) to create distinct tactile or visual patterns. These patterns served as fixed landmarks to support spatial orientation and reward localization during the behavioral

test. Mice received a reward in the form of a drop of condensed milk containing 10% fat upon entering the designated reward zone. Reward delivery was automatic and occurred independently of licking behavior, as long as the mouse entered the reward zone. Each lap completion through the reward zone triggered a single reward delivery. Their behavior was recorded using a body- and eye tracking system (IDS Imaging Development Systems GmbH, Heilbronn, Germany), which was manually activated before each time-series recording. A custom python 2.7 based script (Python Software Foundation, Delaware, USA) was used to track and log the position of the mouse on the treadmill and also to trigger events like reward delivery.

To synchronize the timing of all hardware components like Ca^{2+} imaging and the movement on the treadmill, TTL pulse timestamp of the treadmill that stored by input processor of the galvo-resonant scanner. The reward was dispensed at every belt turn via a custom-built delivery system comprising a pump and a reusable oral gavage needle.

To precisely track the animal's licking behavior, a lick sensor was used. The sensor reliably detects every tongue movement of the mouse by recording capacitive or optical changes as soon as the animal touches the gavage outlet. Licking behavior is directly coupled to the reward delivery system. In defined reward zones within the physical corridor, condensed milk is dispensed as a reward via a pump system, depending on the position reached. At the same time, the lick sensor is used to determine whether and when the animal actually consumes the reward. The precise recording of licking behavior thus serves not only for behavioral analysis, but also for correlation with neural activity patterns collected as part of the Ca^{2+}-imaging setup. The integration of this sensor into the overall system enables comprehensive and high-resolution documentation of behavior and neurophysiology during the experiment.

To log the positional information of the mouse on the treadmill, the licking behavior, and events such as reward delivery, a NI DAQ device (NI USB-6216 BNC) was used. All signals were timestamped and logged with high temporal precision, enabled by the board's high sampling rate (sampling frequency: 10.000 Hz). To align Ca^{2+}-imaging data with behavioral events, TTL pulses triggered by the galvo-resonant scanner were also recorded via the NI 6216 board. All data were saved in a predefined directory (C:\logs) for structured *post hoc* analysis. To motivate the animals to seek the reward, they were placed under a reversed day-night cycle, ensuring that behavioral training occurred during their active phase. In addition, mild food restriction was applied to enhance motivation for the reward. The animals were gradually accustomed to both the setup and the behavioral protocol. For this habituation, the mice were head-fixed and placed on the treadmill for one hour daily over at least five consecutive days. Here, both for habituation

and *in vivo* Ca^{2+} imaging, a small metal adapter was mounted onto the head bar that had previously been affixed to the animal's head (Luigs and Neumann, Ratingen, Germany). The animals were then positioned in a stereotactic frame or holder that stabilized their heads while still allowing them to run on the treadmill. Once they consistently completed at least 20 laps per hour, they were considered ready for the experimental sessions. During the test phase, mice were required to learn and remember the precise location of a reward delivered along a linear treadmill. The reward zone remained constant, and the animals' ability to learn and locate the reward was assessed. Each test session consisted of a single recording with a minimum of 20-30 laps per mouse.

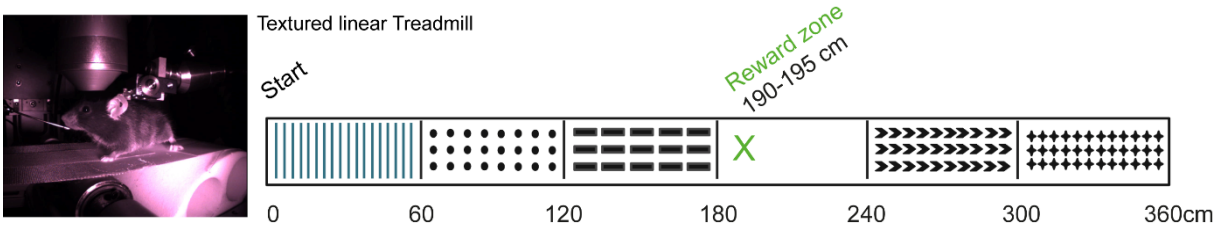

Figure 12. Schematic representation of the textured linear treadmill used for *in vivo* Ca^{2+}-imaging. The belt consists of sequential texture zones, each with distinct tactile patterns, extending over a total length of 360 cm from the start to the end zone with a single reward zone at 190-195 cm.

2.4.2. Two-Photon Imaging

The Ca^{2+} imaging was carried out using a galvo-resonant scanning system (Bergamo, Thorlabs, Newton, USA) integrated into a two-photon microscope. The system was equipped with a 10× air objective (NA 0.50; TL 10x-2P, Thorlabs Inc., Newton, NJ, USA). GCaMP6f was excited using a titanium-sapphire laser (Ti:Sa) operating at 80 MHz (Chameleon, Coherent, Dieburg, Germany), tuned to a wavelength of 920 nm. Emitted green fluorescence was collected through a 525/50 nm bandpass filter (AHF, Tübingen, Germany) and detected by a GaAsP photomultiplier tube (PMT, Thorlabs, Newton, USA). Image acquisition was controlled using ThorImageLS software (Thorlabs, Newton, USA).

Images were acquired at a resolution of 512 × 512 pixels, corresponding to a field of view of 959.05 µm × 959.05 µm and a spatial resolution of 1.873 µm per pixel. The pixel dwell time was 0.08 µs, and images were recorded at a frame rate of 23.962 Hz. A total of 35,000 frames were captured per imaging session, resulting in a total time series duration of approximately 24 minutes.

2.5. Perfusion & Histology

Perfusion is an essential step in the preservation and fixation of tissue. The targeted flushing of the bloodstream with a buffer solution and subsequent fixation creates optimal conditions for subsequent histological examinations. Histological analysis enables detailed examination of tissue at the cellular level. After fixation and processing, staining techniques can be used to visualize specific structures and assess morphological changes.

2.5.1. Perfusion

To achieve reliable tissue preservation, perfusion and fixation are essential. First, the entire circulatory system is flushed with a phosphate-buffered saline solution (pH 7.5). Once the vasculature is blood-free, a fixative is perfused to stabilize cellular architecture.

Immediately after the last behavior experiment, contextual fear conditioning (2.3.4) or head-fixed linear treadmill (2.4.), the mice were deeply anaesthetized with an intraperitoneal lethal dose of Ketamine/Xylazine (0.26/0.02 mg/g; i.p.). Depth of anesthesia was confirmed by the absence of the hind-paw withdrawal reflex. Each animal was secured on the perfusion table and prepared for transcardiac perfusion. A midline laparotomy was performed, extending from the symphysis to the xiphoid process, thereby exposing the thoracic cavity. A cannula was inserted into the left ventricle, and the right atrium was incised to provide an outflow tract for blood.

Perfusion began with ice-cold phosphate-buffered saline (PBS) to prevent clot formation for 5 minutes at a flow rate of around 4 ml/min. When the liver, tail and paws appeared pallor, fixation was initiated with 4% paraformaldehyde (PFA, pH 7.4) for approximately 5 minutes. The skull was then opened, the brain carefully dissected out, and post-fixed overnight in 4% PFA at 4 °C, which induces cross-linking of proteins, rendering the tissue more resilient. On the next day, PFA-fixed brains were stored in 0.01% PBS-azid at 4 °C before further processing.

2.5.2. Histology

Next, coronal brain sections were cut at a thickness of 70 µm by using a vibratome (VT1200, Leica Biosystems, Wetzlar, Germany) and collected in PBS for further processing.

For immunofluorescence staining, the free-floating sections were first permeabilized in 1% Triton X-100 (Sigma-Aldrich (St. Louis, USA)) in PBS for 1 hour at room temperature to increase membrane permeability and facilitate antibody access to intracellular epitopes. To block nonspecific binding sites and reduce background staining, a primary antibody staining solution was prepared. It consisted of 10% normal goat serum (NGS) (Life technologies (Carlsbad, USA)) as a blocking agent, 0.5% Triton X-100 to maintain permeability during

incubation, and 20% bovine serum albumin (BSA) (Roth (Karlsruhe, Germany)) in PBS to stabilize proteins and minimize nonspecific interactions. A defined volume of the respective primary antibody was added to this solution (Table 2), and sections were incubated overnight at room temperature on a shaker at 150 rpm (rounds per minutes).

On the following day, the sections were washed three times for 5 minutes each with PBS to remove unbound primary antibodies. The secondary antibody solution was prepared using 250 µl of 3% BSA in PBS, serving as a diluent and blocking component, and an appropriate amount of fluorescently labeled secondary antibody (Table 2), which binds to the Fc region of the primary antibody. Tissue sections were incubated with this solution for 1.5 hours at room temperature on a shaker again at 150 rpm. To visualize cell nuclei, sections were incubated with DAPI (4′,6-diamidino-2-phenylindole) for 20 minutes at room temperature (Table 2).

After staining, sections were washed once for 10 minutes in 0.5% Triton X-100, followed by three additional washes with PBS (5 minutes each). Finally, the sections were mounted on glass objective slides using DAKO mounting medium (Dako Denmark (Glostrup, Denmark)) and glass cover-slips.

For plaque staining, coronal brain sections were incubated with Methoxy-X04 (MeX04). A working solution was prepared by diluting 20 µl of a 50 mg/ml stock solution in DMSO with 90 µl propanediol and 90 µl PBS. After completion of the secondary antibody incubation, the sections were incubated for 10 min with MeX04 at a final dilution of 1:10,000. This step was followed by a 10 min wash in 0.5% Triton X-100 and three additional washes of 5 min each in PBS. Finally, the slices were embedded in DAKO mounting medium for fluorescence microscopy.

Table 3. Overview of the primary and secondary antibodies used for immunohistochemical staining, including their dilution ratios, LOT number and respective excitation wavelengths for fluorescence microscopy.

Primary antibody	Dilution	#LOT	Secondary antibody	Dilution	#LOT
Chicken anti-cfos	1:250	1-3	Goat anti-chicken IgY, Alexa Fluor® 488	1:400	2566343
Rabbit anti-Somatostatin	1:250	1226160328	Goat anti-rabbit IgG, Alexa Fluor® 647	1:400	2390713
Rat anti-mCherry	1:10000	YH374753	Goat anti-rat IgG, Alexa Fluor® 594	1:400	2026149
DAPI	1:5000		–	–	–

2.5.2.1. Confocal Imaging

Confocal microscopy was performed using a Zeiss LSM 900 laser scanning microscope (Carl Zeiss AG, Oberkochen, Germany) equipped with an Axio Observer Z1/7 inverted microscope stand and a Plan-Apochromat 20×/0.8 M27 objective lens for precise image acquisition. Fluorescence images were acquired using a bidirectional scanning mode with the scan speed configured to setting 8. Here, the pinhole was set to 1.00 Airy Units (AU), which, depending on the emission wavelength of the individual channel, has an optical layer thickness of 23-31 µm. For later image analysis (i.e. cell counting, plaque analysis, axon density) image acquisition was carried out as a tile scan consisting of ~20 tiles with a scaling factor of 0.832 × 0.832 µm per pixel. The z-stack consisted of 6 layers or images covering a total depth of 25 µm. The resulting image field measured 2.36 mm × 3.51 mm (2841 × 4224 pixels) with a pixel dwell time of 1.01 µs and a frame time of 698.18 ms. Four fluorescence channels were recorded simultaneously using GaAsP-PMT detectors (GaAsP-Pmt1(green and blue channel) and GaAsP-Pmt2 (red channel)), each with a digital gain of 1.0.

Importantly, for histological quantifications image acquisition was conducted using four detection channels with different excitation and emission settings. To precisely identify the viral injection site in the vHPC, the fluorescent marker mCherry (Alexa Fluor 594®) was excited at a wavelength of 590 nm. Emitted fluorescence was captured at 618 nm within a detection window of 400-650 nm, using a detector gain of 670 V. For the second channel, excitation of Alexa Fluor 647® was performed at 653 nm, and fluorescence was collected at 668 nm within a spectral detection range of 645-700 nm, using a detector gain of 620 V. The detection of Alexa488® was excited at 493 nm, and emission was detected at 517 nm within a 400-585 nm range; the detector gain was set to 630 V. Lastly, all brain slices were stained with DAPI, which was performed at an excitation at 353 nm, with emission detected at 465 nm across a window of 400-580 nm, and a gain of 650 V applied. All confocal images were saved as .czi format and processed using FIJI (Schindelin et al. 2012).

2.6. Analysis and Statistics

The analysis was divided into various categories, including behavioral analysis, confocal image analysis, Ca^{2+} imaging analysis, and statistical evaluation. In the following, I will explain the individual steps of the data analysis in detail and describe the respective methodological procedures.

2.6.1. Behavior Analysis

Behavioral experiments were analyzed using a combination of commercial and open-source tools like EthoVision XT 17 (Noldus, Wahningen, Netherlands) and DeepLabCut (DLC) Version 2.3.10. (Mathis et al. 2018). EthoVision was primarily used to quantify standard behavioral parameters such as total distance traveled, average velocity, and the duration spent in specific zones of the arena (e.g., center, border, or novel arm) in open field and y-maze test. These metrics provided insights into general locomotor activity and anxiety-related behavior, but also exploration in the novel environment.

2.6.1.1. Ethovision

The behavioral analyses for the open field test and the y-maze test were performed using EthoVision XT17 (Noldus Information Technology). First, the appropriate test setup was selected in the software – the open field square for the open field test and the corresponding y-maze layout for the y-maze test. In the Experiment Settings section, the method for tracking the mouse was specified. Center Point Detection was selected as the tracking method, which tracks movement based on the mouse's center of gravity. The Arena Settings were then fully adapted to the real test setups (e.g., size and shape of the arena) and finalized. In Detection Settings, the parameters for movement detection were defined to ensure the most accurate tracking possible. In the next step, all video files of the individual test animals were uploaded in Trial List and assigned to the test runs. Subsequently, all videos were processed one after the other in Acquisition Mode and the raw data for each test unit was recorded. Finally, the behavior parameters to be analyzed and calculated were defined in the Analysis Profile Settings. For the open field test, these included: distance traveled (in meters), velocity (in cm/s) and the time spent in the border zones (15 cm width on each side and in the center of the arena (20 × 20 cm). For the y-maze test, the following parameters were evaluated: distance traveled, velocity, time spent in the individual arms (in seconds) and preference for certain arms, measured by the duration of visits or number of arm changes.

After completion of the analysis, the data were exported in *.csv* format. These data sets were then imported into GraphPad Prism version 9 (GraphPad Software, Inc., San Diego, CA USA), where they were visualized and analyzed statistically.

2.6.2. DeepLabCut

To enable machine learning based quantification of specific behaviors − particularly freezing, object exploration, and subtle movement dynamics − DeepLabCut, a markerless pose

estimation toolbox based on deep neural networks, was used in the analysis (Mathis et al. 2018; Nath et al. 2019). Before analysis, behavioral videos were manually preprocessed by cropping to the relevant area (e.g., arena), adjusting resolution if necessary, and converting them to a supported duration and format (typically .mp4) by using a custom-built GUI-based video converter, which was developed to facilitate pre-processing.

To train the network, 114 frames were labeled from 6 videos of each experiment different contexts and light conditions. These labeled frames were used for training the network. ResNet-50-based neural network was then used with default parameters for 200.000 training iterations. A subset of video frames was extracted and manually annotated with the positions of the selected body parts. DLC operates by tracking defined body parts frame-by-frame across a video. For the analysis, the following body parts were labeled and used for training: nose, neck, center, left ear, right ear, and tail base. These key points allowed precise tracking of head orientation, posture, and general locomotion for further analysis. These labeled frames were then used to train a deep neural network. The training process included a maximum of 200.000 iterations, with the number of snapshots to keep set to 19, enabling periodic model saving and comparison. After training, the network was evaluated and refined as needed before being used to analyze the full set of behavioral videos. Once predictions were generated, DLC produced time-resolved coordinate data (X, Y positions for each body part) and associated likelihood values, which were exported in *.csv* format. These datasets were further processed using a custom Python-based analysis pipeline. Additionally, custom GUI-based tracking visualizations were generated, producing trajectory plots that provided a detailed and temporally resolved overview of the animal's movement patterns. These visualizations supported both result interpretation and quality control of tracking accuracy. The generated CSV files were used to define relevant parameters tailored to each experimental paradigm. These data were then analyzed using a Python-based analysis pipeline. For the novel object recognition and Fear Conditioning tasks, the following behavioral parameters were quantified: travelled distance (in meters), velocity (in cm/s), movement trajectories and plots within the arena, object investigation times to calculate the discrimination index (DI) (DI = [novel – familiar] / [novel + familiar]) and freezing behavior, which was defined as the complete absence of movement except for respiration and used as a measure of conditioned fear. All results were compiled and plotted using GraphPad Prism version 9 (GraphPad Software, Inc., San Diego, CA, USA) for statistical analysis and graphical visualization.

2.6.3. Image Processing and Quantitative Analysis of Cortical Projections and Plaque Deposition in the mPFC

Confocal image data generated during the corresponding series of experiments was used to analyze cortical projections in the mPFC. Image processing and quantitative analysis were performed using FIJI (Schindelin et al. 2012). Before starting image processing, the relevant measurement parameters, including area, perimeter, and other morphological parameters, were defined via *Analyze* and *Set Measurements*.

The image stacks (z-stacks) to be analyzed were opened by simply inserting the files into the Fiji main window. During the loading process, the "stitch tiles" checkbox was activated in the dialog box that appeared to ensure correct composition of the tile images. In the subsequent selection window, the data from the "Series 1" series was loaded. The quality of the image dataset was visually checked by manually scrolling through the individual layers.

In the first processing step, the image data was smoothed. Then, a global threshold value was defined via *Image → Adjust → Threshold*. The "Triangle" method was used, with the color representation set to 'Red' and the "Dark background" checkbox activated. To determine a representative threshold value, the z-stack was browsed and a slice with a high signal-to-noise ratio was selected. The threshold value used in each case was documented and transferred to the subsequent results table. The "Calculate threshold for each image" option remained deactivated to ensure uniform application of the threshold value to the entire data set.

To extract the axonal projections, the image was then binarized and skeletonized using Skeletonize via *Plugins → Skeleton*.

In the next processing step, a sum image was generated. This was segmented based on a threshold value in the same way as in the first processing step via *Image → Adjust → Threshold*. For further quantification of the data, a particle analysis was performed (*Analyze → Analyze Particles*). Only particles with a size of 0 to a maximum of 3 µm² were considered, with only the "Add to manager" checkbox activated. The ROIs (Region of Interest) generated in this way were saved. This was followed by the final extraction of the projections by executing the third macro. The resulting ROIs were again saved via the ROI Manager. In addition, the sum image was stored as a TIFF file.

All quantitative results, including the documented threshold values and other analysis metrics, were finally entered into the *.xlsx* path. To ensure the comparability and reproducibility of the analyses, all image processing and evaluation was performed under identical parameters for all samples examined.

To analyze plaque deposition in brain sections, particularly in the mPFC, begin by opening the image in the appropriate channel. It is important that the image contains only one channel – specifically the one corresponding to the staining of the plaques. Then, navigate to *Adjust* → *Threshold* and use the slider to set the threshold such that the plaques appear black and the background appears white. Care should be taken to include all relevant plaques while minimizing background noise. Once the threshold has been correctly set, go to *Analyze* → *Set Measurements* and select the options *Area* and *Area Fraction*. These parameters will allow you to determine both the absolute plaque-covered area and the percentage of the image occupied by plaques. To perform the measurement, click on the image to activate it, then either press *M* on your keyboard or select *Analyze* → *Measure* from the menu. The results will be displayed in the Results window, with particular interest in the "Area Fraction," which indicates the percentage of the total image area covered by plaques.

2.6.4. Ca^{2+} Data Analysis

CaImAn (Calcium Imaging Analysis) is the Python-based analysis framework used to process two-photon Ca^{2+} imaging data (Giovannucci et al. 2019). The following steps describe the complete preprocessing of the raw data up to the extraction of the denoised neural signals using the Constrained Non-negative Matrix Factorization (CNMF) pipeline. To study neuronal activity in mice during locomotion, we performed two-photon Ca^{2+} imaging while the animals ran on a linear treadmill. The mice expressed the calcium indicator GCaMP6f, and recordings were made at approximately 24 frames per second. The raw data were saved in TIFF format and later processed using CaImAn. Before extracting signals, motion artifacts were corrected using the NoRMCorre algorithm, which performs non-rigid motion correction. This is especially important in awake, behaving animals, where motion is often non-uniform across the field of view. The data were divided into overlapping patches, and local shifts were corrected within each patch to ensure that each pixel consistently represents the same physical location over time. Key parameters included a patch size of 33 × 33 pixels, 10-pixel overlap, and a maximum shift of ±6 pixels. After motion correction, the corrected video was converted into a memory-mapped file. This approach allows efficient processing of large datasets by keeping the data on disk while treating it as if it were in memory, which is particularly useful for systems with limited RAM. To extract neural signals from the imaging data, we applied the CNMF algorithm. This method simultaneously estimates the spatial footprints of neurons, their corresponding calcium activity over time, and the underlying spike events through deconvolution. The analysis was run in parallel across patches of the field of view. Important

parameters included an expected neuron half-width (gSig) of 4 pixels, a maximum of 6 components per patch, and a merging threshold of 0.85 to combine overlapping components with highly correlated activity. After the initial run, we refined the results using a refit step, where spatial footprints were fixed and temporal components were re-optimized for better accuracy.

To ensure high-quality signal extraction, the identified components were evaluated based on three criteria:

- Signal-to-noise ratio (SNR)
- Spatial correlation between the component and the raw data
- CNN-based shape classification, using a pretrained convolutional neural network

A component was accepted if it passed at least one of the thresholds (e.g., SNR ≥ 2.3, spatial correlation ≥ 0.85, CNN score ≥ 0.99). Components that fell below all thresholds were discarded as likely artifacts. To normalize calcium activity traces across neurons and sessions, we computed ΔF/F. Instead of assuming a fixed baseline period, we used a running 8th percentile over a 250-frame sliding window to estimate the baseline.

The ΔF/F value was then calculated as:

$$\Delta F/F = \frac{F0 - F(t)}{F0}$$

This approach avoids assumptions about quiescent periods and helps to standardize comparisons across datasets. Finally, we reconstructed a denoised version of the movie, combining the model's estimate of neural activity (A*C) and the background signal (b*f). This provides a clean visualization of the activity captured by the model, excluding residual noise. The denoised video was saved both as a TIFF file and as a memory-mapped file for downstream analysis. The behavior of the animals on the linear treadmill was evaluated using a specially developed Python script. This script enabled precise analysis of the velocity, licking behavior, and the corresponding position data. The implementation of the script made it possible to correlate the animals' movement dynamics with the reward-associated licking episodes and their spatial location along the treadmill.

2.6.5. Statistics

The behavior of the animals was examined in various paradigms, including open field test, the y-maze test, object recognition test, and contextual fear conditioning test. Because of the small sample sizes in some of the behavioral experiments, the Shapiro-Wilk test has only limited significance for detecting deviations from normal distribution. Since the data were normally distributed, experiments with multiple test conditions were evaluated using one- or two-factor

analysis of variance (one-way or two-way ANOVA). Multiple comparison tests were then performed using the Holm-Sidak method to correct for multiple testing. In addition, *post-hoc* analyses were performed to examine significant group differences in detail. If the data did not fit a normal distribution (as measured by the Shapiro-Wilk test), nonparametric statistical tests (Mann-Whitney U test for two groups, Kruskal-Wallis test for more than two groups) were used instead of parametric tests.

The results are presented as mean ± standard deviation (mean ± SEM). Statistical significance is indicated in the figures by the following notation: n.s. for $p > 0.5$, * for $p < 0.05$, ** for $p < 0.01$, *** for $p < 0.001$, and **** for $p < 0.0001$.

3. Results

In the following section, I present the results of this study. First, structural and pathological changes in the mPFC are examined, with a focus on Aß deposition. Next, I describe the anatomical mapping of hippocampal inputs, before moving on to functional and behavioral experiments in AD mouse models.

3.1. Mapping of Amyloid-ß Pathology in the mPFC

The following section presents results from an analysis investigating structural and functional alterations in hippocampal inputs to prefrontal cortical networks under Alzheimer-like pathological conditions in a transgenic mouse model. Specifically, the focus is on the mPFC, a brain region crucial for cognitive control, decision-making, and memory formation functions that are impaired in AD. Importantly, accumulating evidence has demonstrated that the mPFC is not only functionally affected in AD, but also undergoes characteristic structural pathology, including amyloid-ß plaque deposition (Jankowsky et al., 2004).

Aß plaques are one of the histopathological hallmarks of AD and are closely linked to synaptic dysfunction and neurodegeneration. Their distribution within cortical and subcortical brain regions correlates with disease progression and the severity of cognitive deficits. Thus, characterizing the spatial distribution and burden of Aß plaques in the mPFC provides critical insight into the potential mechanisms underlying prefrontal cortex dysfunction in AD models.

In the present study, Aß plaque load in 15-month-old APP/PS1 mice was examined, a well-characterized transgenic mouse model that recapitulates major features of AD pathology, including early and robust Aß accumulation (Figure 13a). The mPFC was anatomically subdivided according to established neuroanatomical atlases into three subregions: the ACC, the PL, and the ILA. Each subregion was further analyzed across cortical layers II/III, V, and VIa to investigate potential layer-specific patterns of plaque deposition.

Aß plaques were visualized using MeX04 staining, and neuronal cell bodies were identified via NeuN immunolabeling, as shown in Figure 13b. Particularly, the spatial distribution of plaques revealed distinct laminar patterns across the cortical architecture. Quantitative analysis of Aß plaque burden, expressed as percentage area occupied by plaques, was conducted for each subregion and cortical layer.

The results show a significantly higher Aß plaque load in the ACC compared to the PL and ILA across all examined layers (II/III, V, VIa). Both the PL and ILA exhibited comparatively lower

Aß accumulation (Figure 13c). These findings highlight a region-specific vulnerability within the mPFC, with the ACC emerging as a hotspot for Aß deposition in this AD mouse model. Taken together, the data demonstrate a heterogeneous pattern of Aß pathology within the mPFC, supporting the notion that distinct prefrontal subregions may differentially contribute to the cognitive impairments observed in AD.

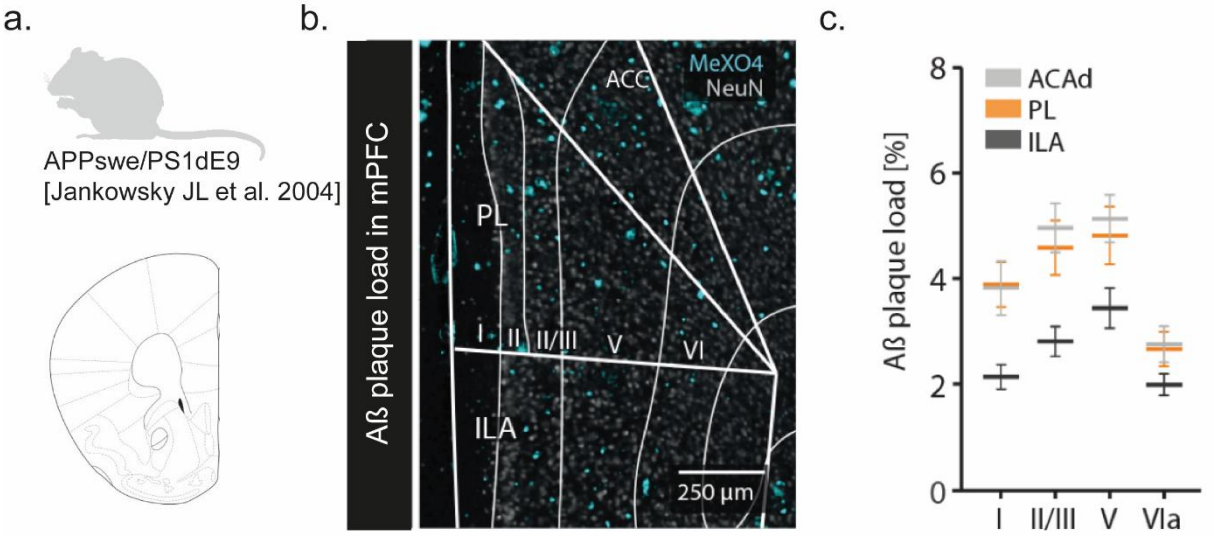

Figure 13. Quantification of Aß plaque load in the mPFC of APP/PS1 mice. a. Schematic of the transgenic APP/PS1 mouse model used for AD research (Jankowsky et al., 2004). **b.** Representative image of Aß plaques (MeX04, blue) and neuronal nuclei (NeuN, grey) in the mPFC. Cortical layers (I, II/III, V, and VIa) and subregions (ACC, PL, ILA) are described. Scale bar: 250 µm. **c.** Quantification of Aß plaque load (% area) across cortical layers I, II/III, V, and VIa in each subregion. The ACC shows dense plaque accumulation in layers II/III and V, while the PL and ILA display comparatively lower plaque density. Quantification is performed in 15-month-old APP/PS1 mice (n = 3), with 18 sections/per mPFC subregion. All quantitative results are presented as mean ± SEM.

3.2. Chemogenetic Silencing of the vHPC in WT Mice

To first understand the contribution of the vHPC activity to cognition and memory-related behavior, a global chemogenetic silencing approach was employed in WT C57Bl/6J mice. This strategy enabled a general functional assessment of vHPC outputs but did not provide cellular or projection specificity. Specifically, an inhibitory DREADD system was employed to transiently silence neuronal activity in the vHPC (Figure 14**Figure 14**). This initial experiment served to evaluate the feasibility and behavioral consequences of broad, chemogenetically induced inhibition of the vHPC in a WT background, prior to application in Cre-dependent, transgenic AD models. As illustrated in Figure 14b, an AAV vector carrying the inhibitory DREADD construct AAV2.hSyn.hM4D(Gi).mCherry was bilaterally injected into the O-LM layer of the CA1 region within the vHPC in both experimental and control groups. The stereotaxic injection targeted coordinates relative to Bregma (AP –3.5 mm, ML –3.7 mm, DV

–3.2 mm) encompassing the entire vHPC axis. The hSyn promoter ensures pan-neuronal expression of the hM4D(Gi) receptor, which, upon activation by the selective agonist CNO, leads to neuronal silencing via Gi-coupled signaling pathways.

The experimental timeline is outlined in Figure 14c. Following viral injection, animals underwent a 5-day handling period for habituation. Behavioral testing began with the OF test to assess locomotor and anxiety-like behavior, followed by the NOR test over two days to evaluate recognition memory. Subsequently, animals were subjected to a cFC paradigm, completed over two consecutive days. After the behavioral assessments, animals were sacrificed for histological verification and analysis of viral expression and targeting accuracy.

Figure 14d shows a representative coronal brain section from a wild-type animal injected with the AAV2.hSyn.DIO.hM4D(Gi).mCherry vector.

This initial experiment served to evaluate the feasibility and behavioral consequences of broad, chemogenetically induced inhibition of the vHPC in a WT background, prior to application in Cre-dependent, transgenic AD models.

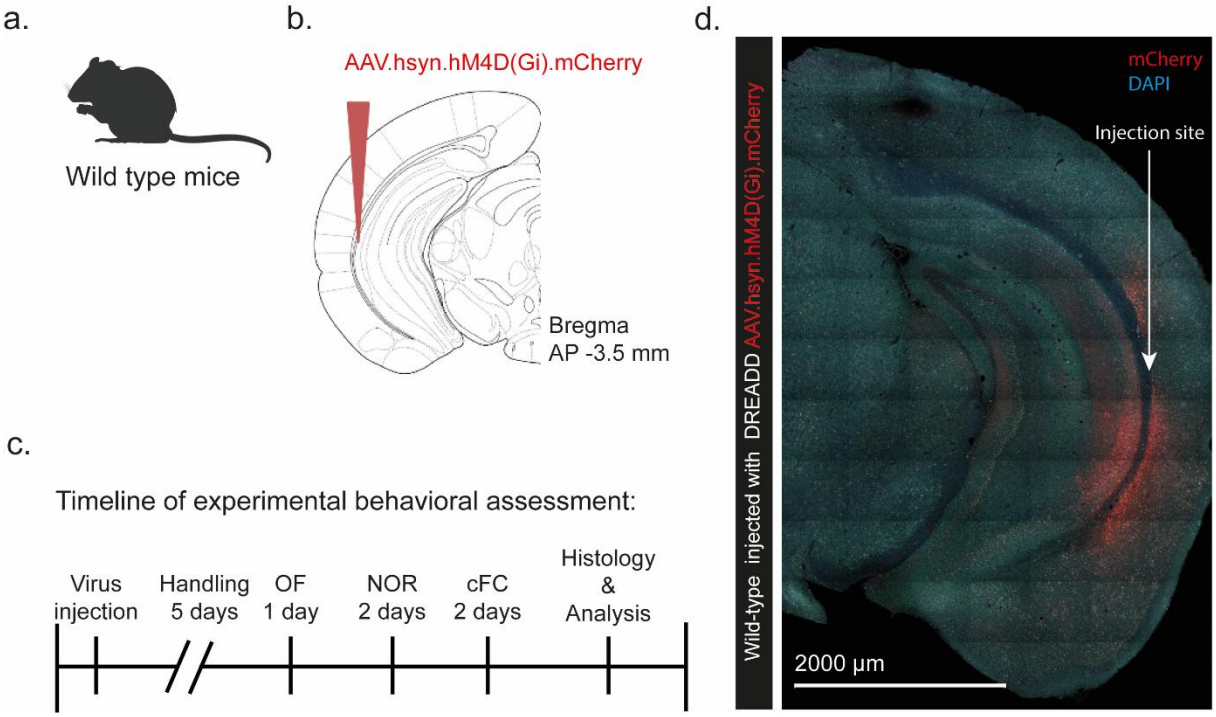

Figure 14. Chemogenetic inhibition of the vHPC in WT mice using hM4D(Gi).DREADDs. **a.** Schematic representation of the experimental animal model. WT mice were used to assess the behavioral impact of chemogenetically silencing the vHPC. **b.** Stereotaxic injection site of AAV2.hSyn.DIO.hM4D(Gi).mCherry) into the vHPC (AP –3.5 mm). The vector enables pan-neuronal expression of the inhibitory DREADD receptor hM4D(Gi) under control of the human synapsin promoter, with mCherry as a fluorescent reporter. **c.** Timeline of the behavioral experiment. Following virus injection, animals underwent a 5-day handling period, followed by a sequence of behavioral tests: OF (1 day), NOR (2 days), and cFC (2 days). After completion of behavioral testing, brains were collected for histological verification of viral expression and targeting. **d.** Representative coronal brain section showing mCherry expression

(red) and DAPI-stained nuclei (blue) in a WT mouse injected with the DREADD. The injection site is indicated by the arrow. Widespread mCherry fluorescence confirms successful and anatomically targeted expression of the DREADD construct throughout the vHPC formation. mCherry fluorescence (red) indicates the expression of the DREADD construct, and DAPI staining (blue) marks cell nuclei. The arrow highlights the injection site, confirming widespread expression of the construct throughout the vHPC. The image demonstrates the anatomical specificity and coverage of the viral transduction in the target region.

After at least three weeks of viral expression, behavioral tests were performed. Throughout the behavioral experiments, locomotor and cognitive parameters were quantitatively assessed using automated video-based tracking systems. Specifically, EthoVision XT software was used for the analysis of the OF test, while DLC was employed for markerless pose-estimation-based tracking during NOR and cFC tasks. The following behavioral parameters were extracted and analyzed: total distance traveled, average velocity, movement duration, time spent in the center zone vs. border zone, freezing behavior and DI.

Figure 15 presents data from the OF test, a widely used behavioral assay to assess general locomotor activity and anxiety-like behavior in rodents. The test relies on the natural conflict between a rodent's exploratory drive and its aversion to open, brightly lit spaces. Increased time spent in the center of the arena is typically interpreted as reduced anxiety, while preference for the periphery indicates heightened anxiety levels.

Prior to the OF test, experimental mice were systemically treated with CNO (3 µg/g; i.p.), whereas control mice received the same amount of saline, 45 minutes before behavioral assessment to selectively silence vHPC neurons (Figure 15a).

Figure 15b shows a representative locomotor trajectory of a control mouse within the open field arena, with the red square outlining the central zone used for assessing anxiety-like behavior. Analysis of cumulative movement duration (Figure 15c) revealed a slight, but non-significant increase in CNO-treated animals compared to controls, indicating that chemogenetic silencing of the vHPC did not impair general exploratory drive. Similarly, there were no significant differences in total distance traveled (Figure 15d) or average velocity (Figure 15e) between groups, suggesting that baseline locomotor function remained unaffected by CNO treatment.

Assessment of spatial exploration patterns yielded further insights into anxiety-related behavior. The cumulative time spent in the border zone (Figure 15f) did not differ significantly between groups. Additionally, although CNO-treated animals exhibited a reduced tendency to explore the center of the arena − a behavior typically associated with increased anxiety − this effect was not statistically significant (Figure 15g). Together, these data suggest a trend toward reduced anxiety-like behavior following vHPC inhibition, without significant impairment in locomotor performance.

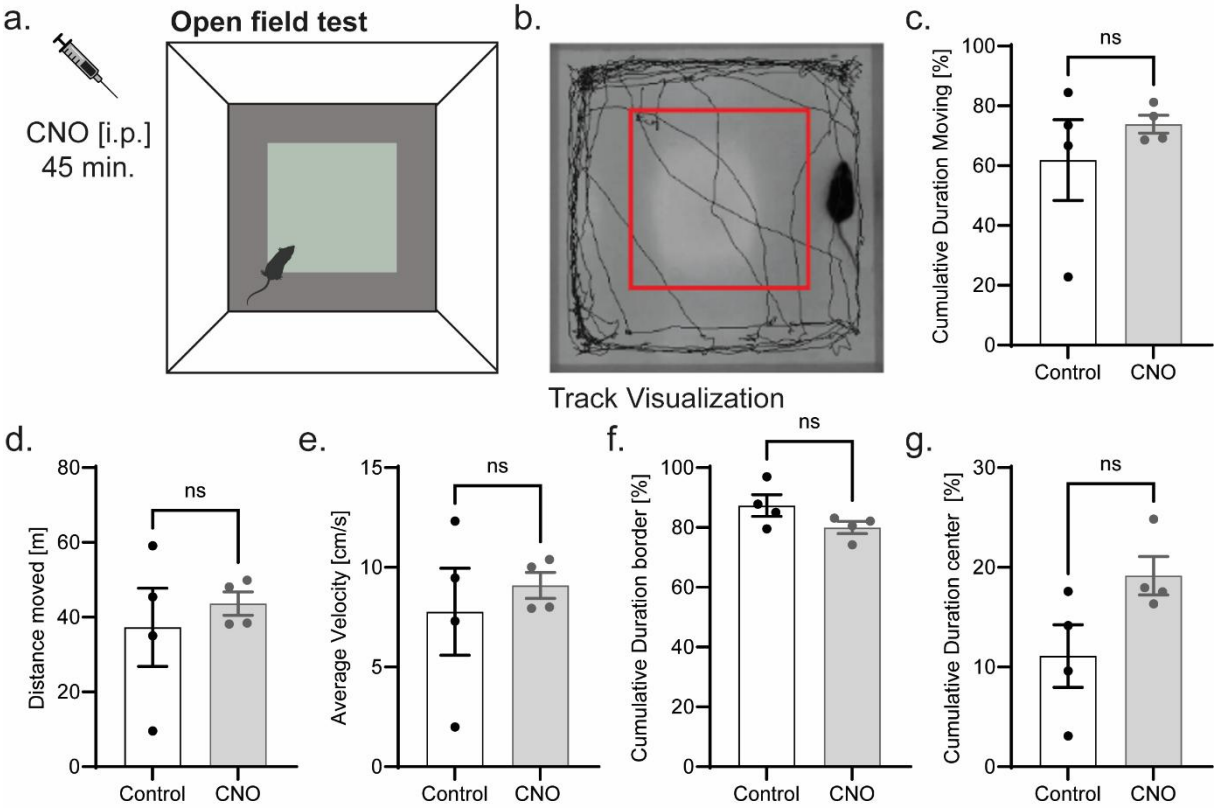

Figure 15. Schematic of an OF analysis to assess locomotor and anxiety-like behavior following chemogenetic silencing of the vHPC in WT mice. a. Schematic overview of the experimental design. WT mice were stereotactically injected with AAV2.hSyn.DIO.hM4D(Gi). mCherry into the vHPC. Mice received an intraperitoneal injection of either CNO (n = 4) or saline (n = 4) 45 minutes prior to the OF test to activate inhibitory DREADDs (hM4D(Gi)). **b.** Representative track plot showing the locomotor trajectory of a control mouse during the 10-minute open field session. The red square indicates the defined center zone used for anxiety analysis. **c.** Cumulative movement duration was slightly increased in the CNO group compared to controls, but the difference did not reach statistical significance (unpaired two-tailed t-test: $p > 0.5$). **d–e.** No significant differences were observed in total distance traveled ($p > 0.5$; **d**) or average velocity ($p > 0.5$; **e**), indicating intact basal locomotor function across groups. **f.** Time spent in the border zone was comparable between CNO and saline groups ($p > 0.5$). **g.** Time spent in the center zone was modestly increased in CNO-treated mice, consistent with reduced anxiety-like behavior, but this difference also failed to reach statistical significance ($p > 0.5$). Data are shown as mean ± SEM. Each dot represents an individual animal. Statistical comparisons were made using unpaired two-tailed t-tests.

To assess the impact of vHPC silencing on recognition memory, a NOR test was conducted in WT mice expressing inhibitory DREADDs (hM4D(Gi)) in the vHPC. Mice received either CNO (experimental group) or saline (control group).

The NOR paradigm consisted of an acquisition phase of three sessions of 15 minutes each, followed by two test phases − short-term memory at 2 hours and long-term memory at 24 hours. During acquisition, mice explored two identical objects (familiarization). The test sessions included one previously encountered (familiar) object and one novel object (novel object 1). A different novel object (novel object 2) was used at each time point to allow independent

assessment of short- and long-term memory. CNO or saline was administered 45 minutes before each test phase to activate the hM4D(Gi) receptors and inhibit vHPC neurons. Exploration behavior during the acquisition phase decreased over time, as indicated by a decline in investigation time from *t1* to *t3*. This habituation effect is typical and confirms that the animals became familiar with the objects (Figure 16b). The DI was calculated to quantify recognition memory performance, with a value of 0.5 representing chance level (equal preference for novel and familiar objects) (Figure 16).

At 2 hours post-acquisition (Figure 16c), both saline- and CNO-injected mice showed DI values not significantly different from chance. No significant group differences were observed between the control and CNO-treated experimental conditions. Similarly, at the 24-hour time point (Figure 16d), neither group demonstrated significant object discrimination, and no difference was observed between treatments. The DI remained at or near chance level in both saline and CNO conditions. Chemogenetic inhibition of the vHPC via CNO administration in hM4D(Gi)-expressing WT mice did not affect short- or long-term object recognition memory in this behavioral setting. Group comparisons were statistically non-significant (ns), and both CNO- and saline-treated animals failed to show object preference above chance at either time point.

These findings suggest that global silencing of the vHPC under these experimental conditions does not impair NOR performance in WT mice.

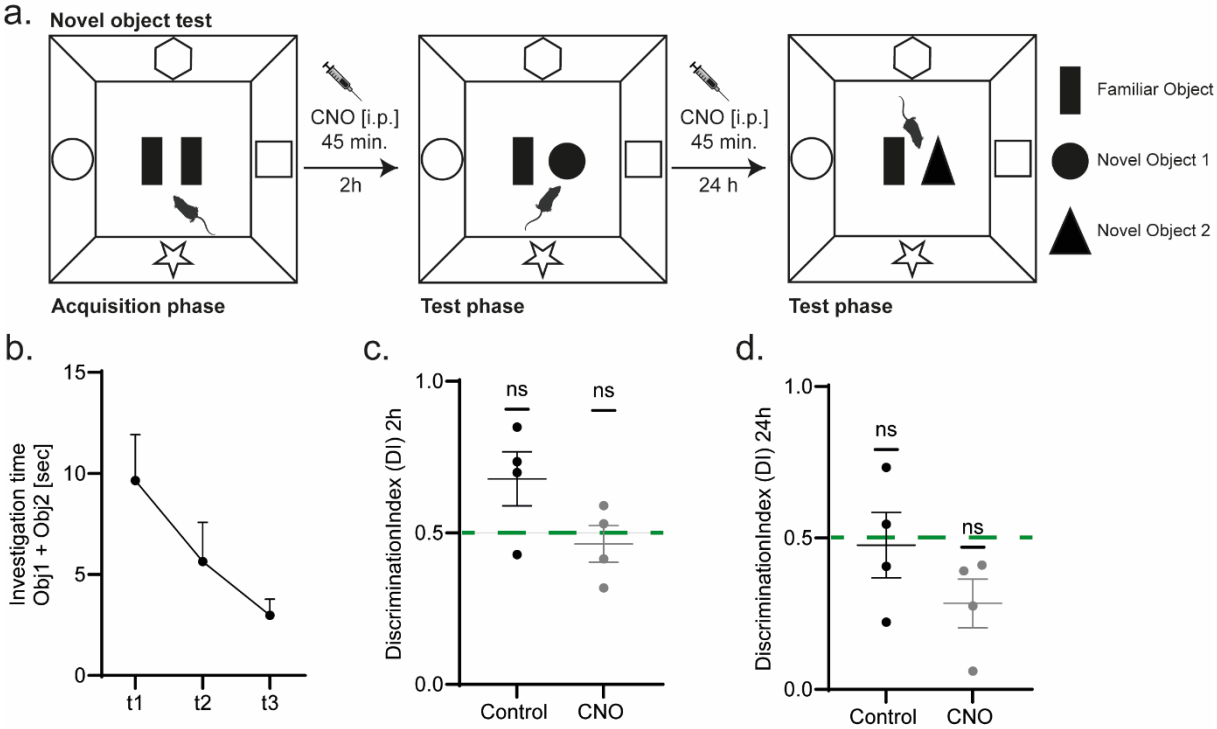

Figure 16. Chemogenetic inhibition of the vHPC does not impair short- or long-term object recognition memory in WT mice. a. Schematic representation of the NOR test paradigm. Mice underwent an acquisition phase (3 × 15 min.) with two identical objects,

followed by test phases at 2 hours (short-term memory) and 24 hours (long-term memory), during which one familiar object was replaced by a novel object (novel object 1 at 2 h, novel object 2 at 24 h). CNO (n = 4) or saline (n = 4) was administered 45 minutes prior to each test session to activate hM4Di DREADDs expressed in the vHPC in mice. **b.** Total investigation time of both objects during the acquisition phase decreased significantly across three consecutive time bins (t1 – t3), indicating normal habituation and successful encoding of object information (one-way repeated measures ANOVA: $p > 0.5$). **c.** DI at 2 h post-acquisition. Neither saline-treated nor CNO-treated mice showed significant preference for the novel object compared to chance level (dashed green line at DI = 0.5). One-sample t-tests against 0.5: saline group, $p > 0.5$; CNO group, $p > 0.5$; unpaired t-test between groups: $p > 0.5$. **d.** DI at 24 h post-acquisition. Again, no significant discrimination was observed in both groups (saline: n = 4; CNO: n = 4 (one-sample t-tests against 0.5: all $p > 0.05$; unpaired t-test: $p > 0.5$. Data is presented as mean ± SEM.

To investigate the functional role of the vHPC in contextual fear learning and memory retrieval, a cFC paradigm, consisting of an acquisition phase on day 1 (Figure 17a) and a retrieval test on day 2 (Figure 17d), was conducted. On both days, animals received either CNO or saline prior to the respective sessions. During the acquisition phase, animals were placed in the conditioning chamber for 5 minutes and received three mild foot shocks (0.75 mA) for two seconds in one-minute intervals (120, 180 and 244 s) (Figure 9). The next day, mice were re-exposed to the same context for 5 minutes without shocks to assess contextual memory.

Freezing behavior during the acquisition increased progressively after shock presentations (S1–S3), indicating normal learning in both saline- and CNO treated animals (Figure 17b). No significant difference was observed between groups. Representative locomotor traces illustrate typical exploratory behavior of a control mouse during day 1 (acquisition) and reduced movement during day 2 (retrieval), consistent with conditioned fear (Figure 17c). Locomotor measures including total distance traveled (Figure 17f) and average velocity (Figure 17g) during acquisition (day 1) did not differ significantly between treatment groups, suggesting that CNO administration did not affect general activity levels during learning. During the retrieval test (day 2), freezing levels were similar between saline and CNO groups (Figure 17e), with no significant differences detected, indicating that chemogenetic inhibition of the vHPC did not impair memory expression. Likewise, distance traveled and velocity during the test phase (Figure 17f/g; day 2) showed no significant group differences, confirming intact locomotor performance under both conditions.

Chemogenetic silencing of the vHPC via systemic CNO administration did not alter the acquisition or retrieval of contextual fear memory in WT mice. These results suggest that transient vHPC inhibition under the tested conditions does not disrupt fear learning or its behavioral expression.

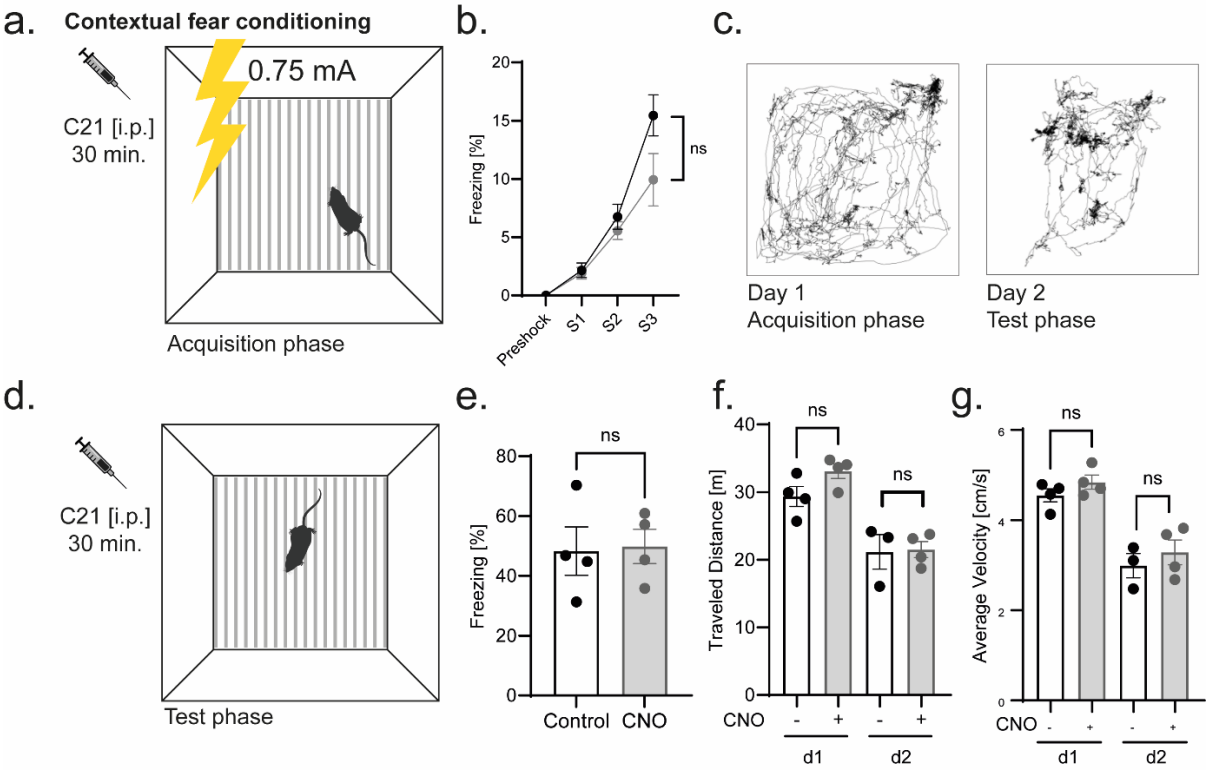

Figure 17. Chemogenetic inhibition of the vHPC during cFC in WT mice. a. Schematic of the cFC paradigm. Mice received an intraperitoneal injection of the DREADD agonist CNO (experimental; n = 4) or saline (control; n = 3-4) 45 minutes before the acquisition session. Animals were placed in a conditioning chamber for a total of 5 minutes. After an initial baseline period (pre-shock), three foot shocks (0.75 mA, 2 sec.) were administered at defined intervals (S1–S3). **b.** Freezing behavior during the acquisition phase showed a progressive increase across inter-shock intervals. No significant difference was observed between CNO-treated and control animals (two-way repeated measures ANOVA, interaction effect: $p > 0.05$). Representative locomotor traces from a DREADD-induced animal across both days. Left: day 1 (acquisition); right: day 2 (test phase), showing reduced movement during retrieval. **d.** On the following day, mice were returned to the same context for a 5-minute retrieval session, again 45 minutes after CNO injection. **e.** Freezing levels during the test phase did not differ significantly between CNO-treated and control groups (unpaired t-test, $p > 0.05$). **f.-g.** Locomotor activity during acquisition (d1) and test (d2) phases. No significant group differences were detected in total distance traveled **(f)** or average velocity **(g)** (two-way ANOVA, all $p > 0.05$). Data is shown as mean ± SEM.

3.3. Impact of SST$^+$ vHPC-mPFC Circuits in AD

3.3.1. Mapping Long-Range SST$^+$ Projections from vHPC to mPFC in SST-Cre::APP/PS1 Mice

Following the global chemogenetic silencing of the vHPC in WT animals, which allowed for an initial assessment of the functional relevance of hippocampal output on cognition and memory-related behavior, the next step was to dissect the contribution of specific neuronal subtypes within this circuit. While the number of mice analyzed were low, it also lacked the anatomical and cellular specificity required to identify which subcomponents of the

hippocampal circuit might be involved in the behavior tested, rendering possible conclusions difficult. I therefore changed the strategy and decided to address specifically the involvement of inhibitory projections from the vHPC to the mPFC in the context of AD.

To address this, a projection- and cell-type specific strategy was implemented using SST-Cre and SST-Cre::APP/PS1 mice. To enable cell-type-specific manipulation in an AD-relevant background, SST-Cre mice (Taniguchi et al., 2011) were crossed with APP/PS1 mice (Jankowsky et al., 2004), generating offspring in which Cre recombinase is selectively expressed in SST^+ neurons allowing for circuit manipulation within the pathological context of amyloid-ß accumulation. This cross results in offspring that express Cre recombinase selectively in SST^+ INs. The use of this genetic strategy permits Cre-dependent viral constructs to be directed specifically to inhibitory neurons along the hippocampal-prefrontal axis. In particular, it allows precise manipulation of SST^+ GABAergic INs in the vHPC.

Here, selective expression of the fluorescent reporter tdTomato in SST^+ neurons and their axons was achieved via stereotactic injection of AAV1.CAG.FLEX.tdTomato into the vHPC. This strategy allowed specific visualization of vHPC-derived SST^+ axon terminals in prefrontal regions (Figure 18a). Histological analysis of mPFC tissue sections revealed a pronounced accumulation of SST^+ axonal projections in the PL of APP/PS1 mice. High-resolution confocal microscopy further showed that these SST^+ axons are frequently found in close spatial proximity to amyloid-ß plaques, which were labeled with MeX04. Neuronal cell nuclei were counterstained using NeuN, as shown in (Figure 18c). To assess the pathological environment along these projection pathways, Aß plaque burden specifically within regions densely innervated by $tdTomato^+$ fibers were quantified.

Here, the area density covered by SST^+ projections was significantly elevated in the PL region along the vHPC→PL projection axis in SST-Cre::APP/PS1 mice (Figure 18d/e). This analysis was conducted on brain sections where the SST^+ projection field was clearly defined, allowing for a precise correlation between plaque deposition and axonal localization (Figure 18c/d). Interestingly, SST^+ axonal labeling showed a high degree of regional specificity, with dense fiber innervation in the PL, whereas neighboring mPFC subregions displayed substantially lower levels of SST^+ input. This spatial restriction enabled a detailed mapping of hippocampal-prefrontal SST^+ projections and their potential involvement in AD-related pathology within the prefrontal cortex (Figure 18e).

These findings support the first anatomical evidence for direct LRIPs from the vHPC to the PL of the mPFC and its selective vulnerability of Aß pathology. The overlap between SST^+ axon

terminals and Aß plaques suggests that these input pathways may constitute anatomically and functionally defined circuits which may be affected in early AD progression.

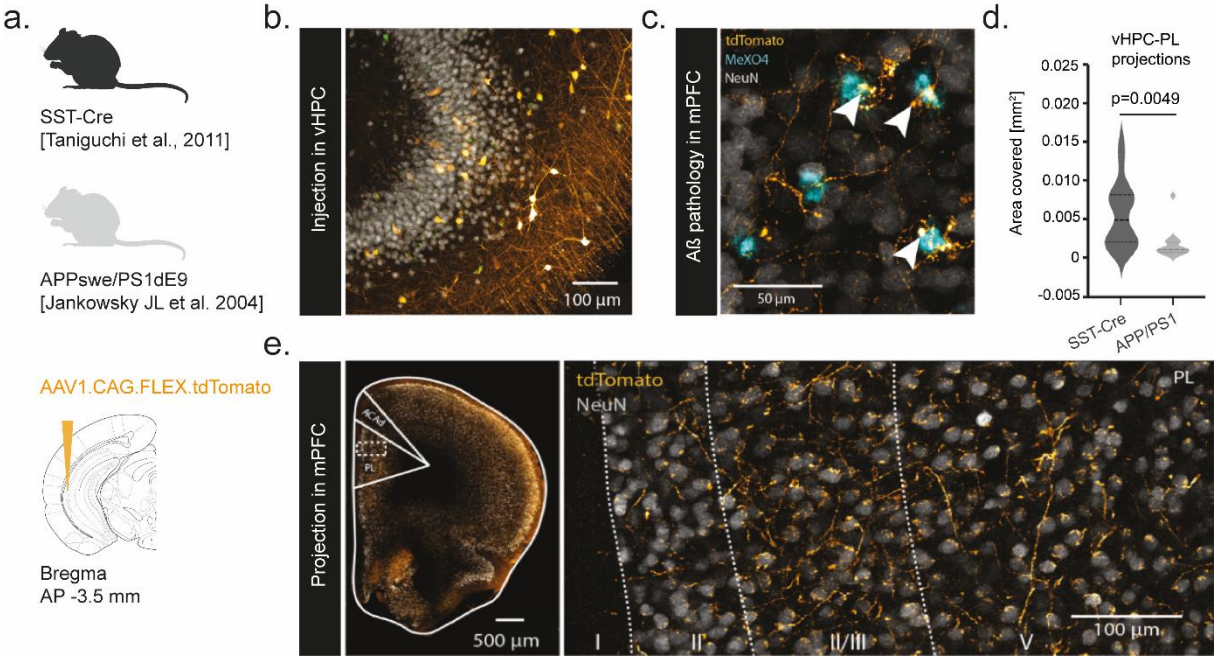

Figure 18. Tracing of SST⁺ projections from the vHPC to the mPFC in SST-Cre and SST-Cre::APP/PS1 mice. a. Illustration of the experimental mouse models: SST-Cre mice (Taniguchi et al., 2011) crossed with APP/PS1 mice (Jankowsky et al., 2004). AAV1.CAG.FLEX.tdTomato was injected into the vHPC to label SST⁺ neurons and their projections. **b.** AAV-mediated injection in the vHPC CA1 region labels SST⁺ axonal projections (orange) and local SST⁺ INs (orange) in SST-Cre:: APP/PS1 mice. **c.** High-magnification image showing the accumulation of Aß plaques (MeX04, blue) in close proximity to SST⁺ fibers (orange) in the mPFC. NeuN (gray) labels neuronal nuclei. Arrows indicate sites of spatial proximity between plaques and SST⁺ axons. **d.** Quantification of Aß plaque burden within the PL area of the mPFC reveals a significant increase in plaque load along vHPC-PL projections (unpaired t-test; p = 0.0049). Quantification was performed in 15-month-old SST-Cre mice (n = 4) and SST-Cre::APP/PS1 mice (n = 4), with 3-6 regions/ per mouse. **e.** Overview of SST⁺ axonal projections from vHPC to the mPFC, visualized via tdTomato⁺ expression. Strong laminar innervation is observed in PL, particularly in layers II/III and V. Dashed lines indicate cortical layers and subregion borders (ACC, PL, ILA).

3.3.2. Investigating Circuit-Specific Connectivity in SST-Cre Mice

After discovering direct LRIPs from the vHPC to the mPFC for the first time, it was essential to assess the functional relevance of these connections − particularly in the context of AD. To this end, the next logical step was to investigate whether selective silencing of these inhibitory projections has measurable effects on behavior. As a pilot approach, classical behavioral paradigms such as OF and NOR were conducted to assess locomotor, anxiety-like, and memory-related functions, serving as a first step toward understanding the contribution of vHPC SST⁺ projections to cognitive and memory processing in AD.

To silence these neurons, a Cre-dependent AAV2.hSyn.DIO.hM4D(Gi).mCherry was stereotactically injected into the vHPC. The hM4D(Gi) receptor allows for chemogenetic silencing of infected neurons upon systemic administration of the ligand CNO. This approach ensured precise, temporally controlled inhibition of SST^+ neuronal activity during behavior (Figure 19a).

Following viral expression, mice underwent the behavioral testing sequence described above (Figure 19c), beginning with a 5-day habituation period, followed by the OF test to assess locomotor and anxiety-like behavior, and the NOR task to examine recognition memory. These paradigms were selected for their sensitivity to hippocampal and prefrontal circuit function, providing a functional readout of the targeted circuit manipulation.

The histological validation shown in Figure 19d confirms successful expression of the DREADD construct in the vHPC. mCherry fluorescence highlights the spatial extent of viral spread and neuronal targeting, while DAPI staining provides an overview of the brain cytoarchitecture. The surgical procedure and injection were performed in a methodical manner, ensuring precise delivery to the CA1 O-LM layer, thereby confirming the accuracy of the targeted region.

Together, this experimental setup establishes the foundation and first steps for functional circuit analysis of LRIPs from vHPC→mPFC in AD. By combining cell-type-specific chemogenetics with behavior, this approach enables a direct investigation of how SST^+ vHPC neurons contribute to cognitive processes and whether their dysfunction may underlie behavioral deficits observed in AD models.

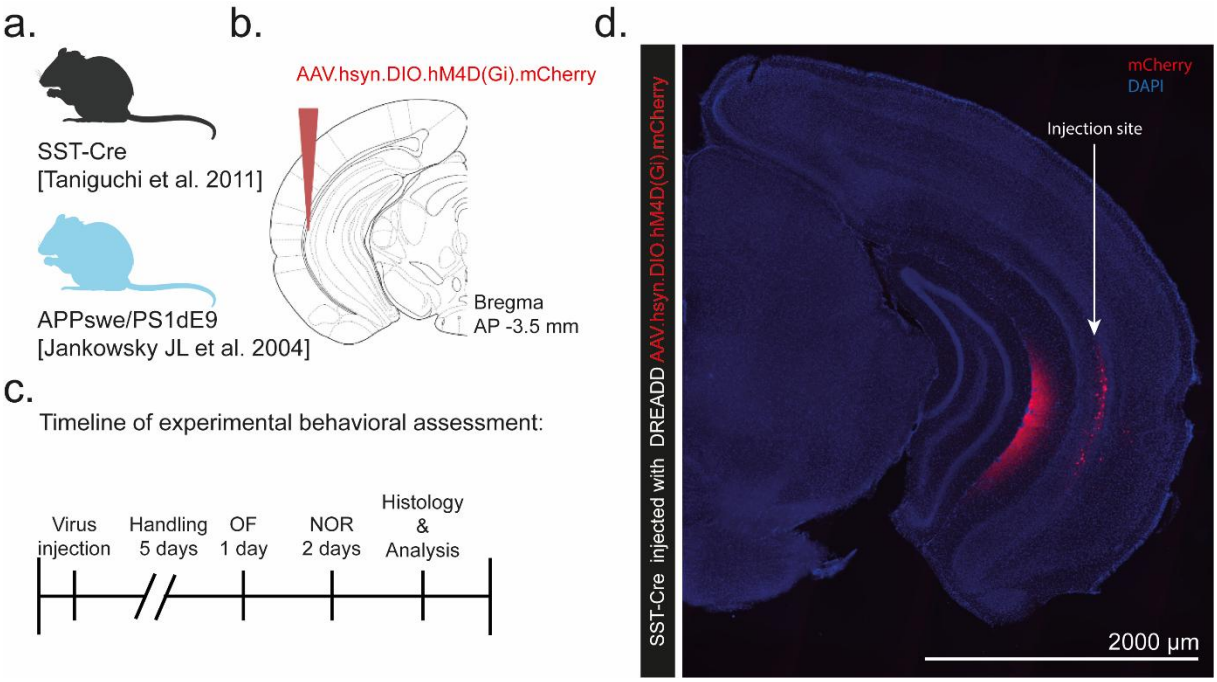

Figure 19. Schematic overview of the experimental design for selective chemogenetic silencing of SST$^+$ neurons in the vHPC of AD model mice. a. Transgenic mouse lines used in this experiment: SST-Cre mice were crossed with APP/PS1mice to generate offspring for targeted circuit manipulation in the AD context. **b.** Cre-dependent viral vector strategy for cell-type specific DREADD expression. AAV2.hSyn.DIO.hM4D(Gi).mCherry was stereotactically injected into the vHPC (Bregma: AP –3.5 mm) to enable selective expression of the inhibitory DREADD receptor (hM4D(Gi)) in SST$^+$ neurons. **c.** Timeline of experimental behavioral testing. Following virus injection and a 5-day handling period, mice underwent OF testing, the NOR test, and finally histological processing and analysis. **d.** DREADD-expressing neurons in the vHPC. mCherry shows the expression of hM4D(Gi), and DAPI co-staining indicates nuclear labeling. The expression is localized within the vHPC region, confirming successful and targeted viral delivery.

To assess general locomotor activity and anxiety-like behavior following chemogenetic silencing of SST$^+$ neurons in the vHPC of SST-Cre and SST-Cre::APP/PS1 transgenic mice, the open field test was conducted. Mice received intraperitoneal injections of CNO (SST-Cre; CNO$^+$ and SST-Cre::APP/PS1; CNO$^+$) or saline (SST-Cre; CNO$^-$ and SST-Cre::APP/PS1; CNO$^-$) 45 minutes prior to behavioral testing to activate the inhibitory hM4D(Gi) DREADD receptors expressed selectively in SST$^+$ neurons, thereby allowing transient silencing of these cells (Figure 20a). Figure 20b and c show that in saline injected SST-Cre mice (SST-Cre; CNO$^-$) exhibited a significant reduction in both total distance traveled and average velocity compared to SST-Cre::APP/PS1 (SST-Cre::APP/PS1; CNO$^-$) ($p < 0.01$). These findings indicate hypoactivity in the APP/PS1 model under baseline conditions. Interestingly, this genotype-related difference in locomotor activity was no longer observed upon chemogenetic silencing of SST$^+$ vHPC neurons: SST-Cre::APP/PS1 (SST-Cre::APP/PS1; CNO$^+$) mice treated with CNO exhibited similar levels of movement and speed as SST-Cre::APP/PS1 (SST-

Cre::APP/PS1; CNO^{-}) (no significant differences between groups), suggesting that silencing SST^{+} activity restored normal motor output in AD model animals. In contrast, no significant group differences were observed for cumulative movement duration (Figure 20d), cumulative time spent in the center zone of the arena (Figure 20e), or time spent along the border region (Figure 20f). These parameters are commonly interpreted as indicators of exploratory behavior and anxiety-like phenotypes. The absence of significant differences across genotypes and treatment groups suggests that silencing vHPC SST^{+} neurons did not alter anxiety-related behavior under these conditions.

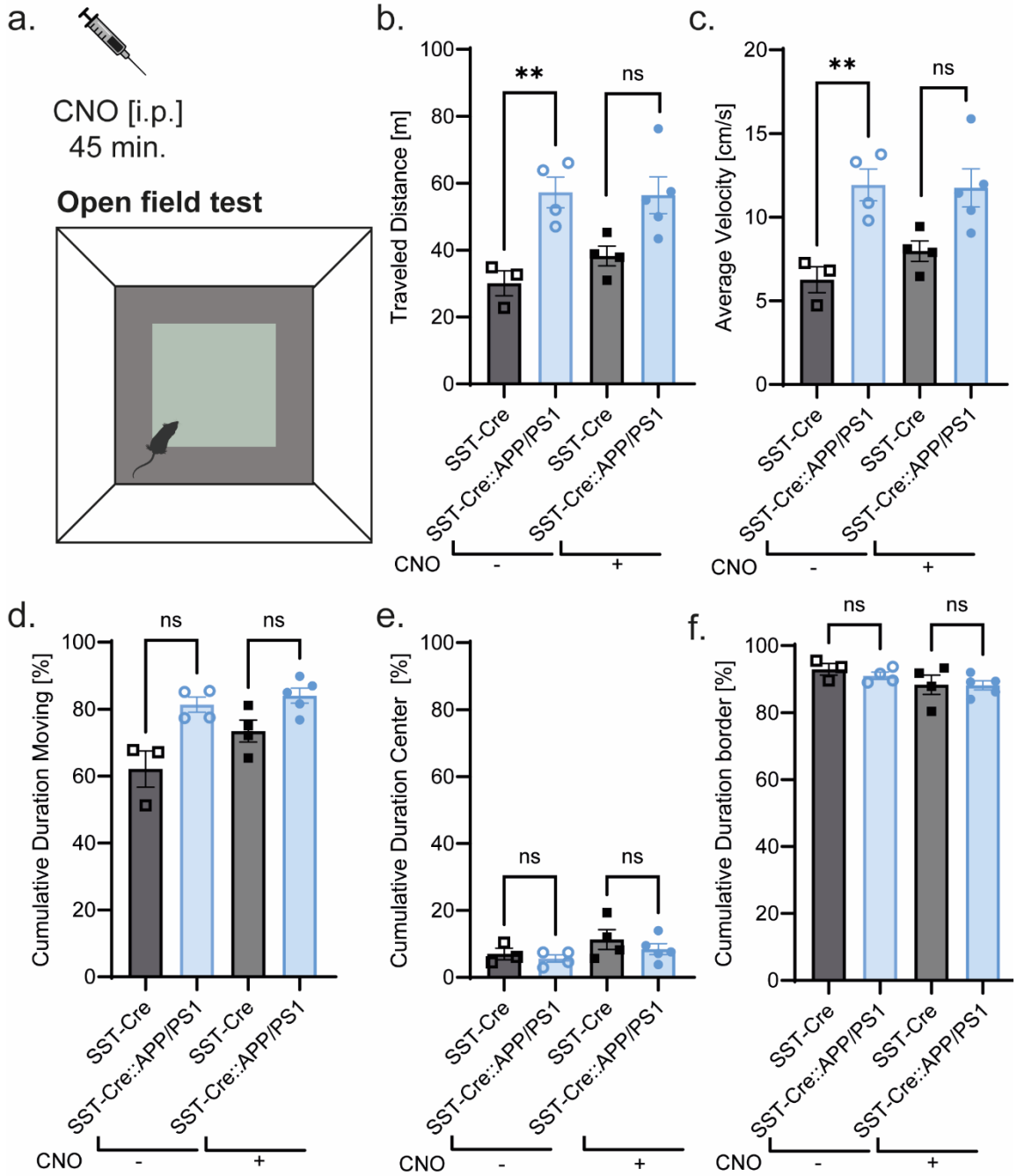

Figure 20. OF analysis following chemogenetic silencing of SST^{+} neurons in SST-Cre and SST-Cre::APP/PS1 mice. a. Schematic illustration of the OF test used to assess general locomotor activity and anxiety-like behavior. Mice received an intraperitoneal injection of CNO

or saline 45 min prior to testing, to activate the inhibitory DREADD receptor (hM4D(Gi)) selectively expressed in SST^+ neurons of the vHPC. **b.-c.** Quantification of traveled distance **(b)** and average velocity **(c)** revealed a significant hypoactivity in SST-Cre::APP/PS1; CNO^- mice compared to SST-Cre; CNO^- (control) under baseline conditions (saline-injected; $p < 0.01$, two-way ANOVA with Tukey's *post hoc* test). Chemogenetic silencing via CNO normalized these parameters in APP/PS1; CNO^+ mice, abolishing the genotype-related difference. **d.-f.** No significant group differences were detected for cumulative duration of movement **(d)**, time spent in the center **(e)**, or in the border zone **(f)** of the open field. These results suggest no alterations in anxiety-like behavior across genotypes or treatment groups. Animals: SST-Cre; CNO^-: n = 3; SST::APP/PS1; CNO^-: n = 4; SST-Cre; CNO^+: n = 4; SST::APP/PS1; CNO^+: n = 4. Data are presented as mean ± SEM.

Experimental design of NOR, to assess recognition memory and evaluate the functional role of SST^+ neurons in the vHPC, is shown in Figure 21a. Here, mice first underwent an acquisition phase with two identical objects, followed by a short-term memory test at 2 hours and a long-term memory test at 24 hours. In both test phases, one familiar object was replaced with a novel object, and time spent investigating each was recorded to calculate the DI.

During the acquisition phase (t1-t3), SST-Cre mice showed less investigation time across trials, which indicates normal habituation to the objects. In contrast, SST-Cre::APP/PS1 mice continued to explore at a high level and did not show the same decline. This suggests a reduced ability to habituate, in line with early problems in novelty recognition and memory. At the 2 h short-term memory interval (Figure 21c), only SST-Cre (SST-Cre; CNO^+) mice treated with CNO exhibited a DI significantly above chance (one-sample t-test vs. 0.5: $p < 0.05$), indicating preserved recognition memory despite acute inhibition of SST^+ vHPC neurons. In contrast, SST-Cre mice (SST-Cre; CNO^-) did not perform significantly above chance ($p > 0.05$), likely due to low n numbers with high variability, as one mouse showed zero interaction with object. Both groups of APP/PS1 mice, (SST-Cre::APP/PS1; CNO^-) and (SST-Cre::APP/PS1; CNO^+), failed to discriminate the NOR test with DI values not differing from chance ($p > 0.05$).

At the 24 h retention interval (Figure 21d), performance deteriorated in all groups. Nonetheless, both SST-Cre; CNO^- and SST-Cre; CNO^+ groups maintained DI values significantly above chance ($p < 0.05$ vs. 0.5), indicating preserved long-term recognition memory in SST-Cre mice regardless of SST^+ circuit activity. In contrast, both APP/PS1 groups (SST-Cre::APP/PS1;CNO^- and SST-Cre::APP/PS1;CNO^+) again failed to discriminate the novel object ($p > 0.05$), indicating persistent memory deficits in the AD model. Notably, no significant differences in DI ($p > 0.05$) were detected between SST::APP/PS1; CNO^- and SST::APP/PS1; CNO^+ (Figure 21d).

Together, these findings demonstrate that SST^+ hippocampal-prefrontal projections are not required for intact recognition memory in WT mice, as memory performance remains

unaffected by acute silencing. In contrast, the AD-like condition (SST::APP/PS1) is associated with profound object recognition deficits, which are not ameliorated by chemogenetic suppression of SST$^+$ input.

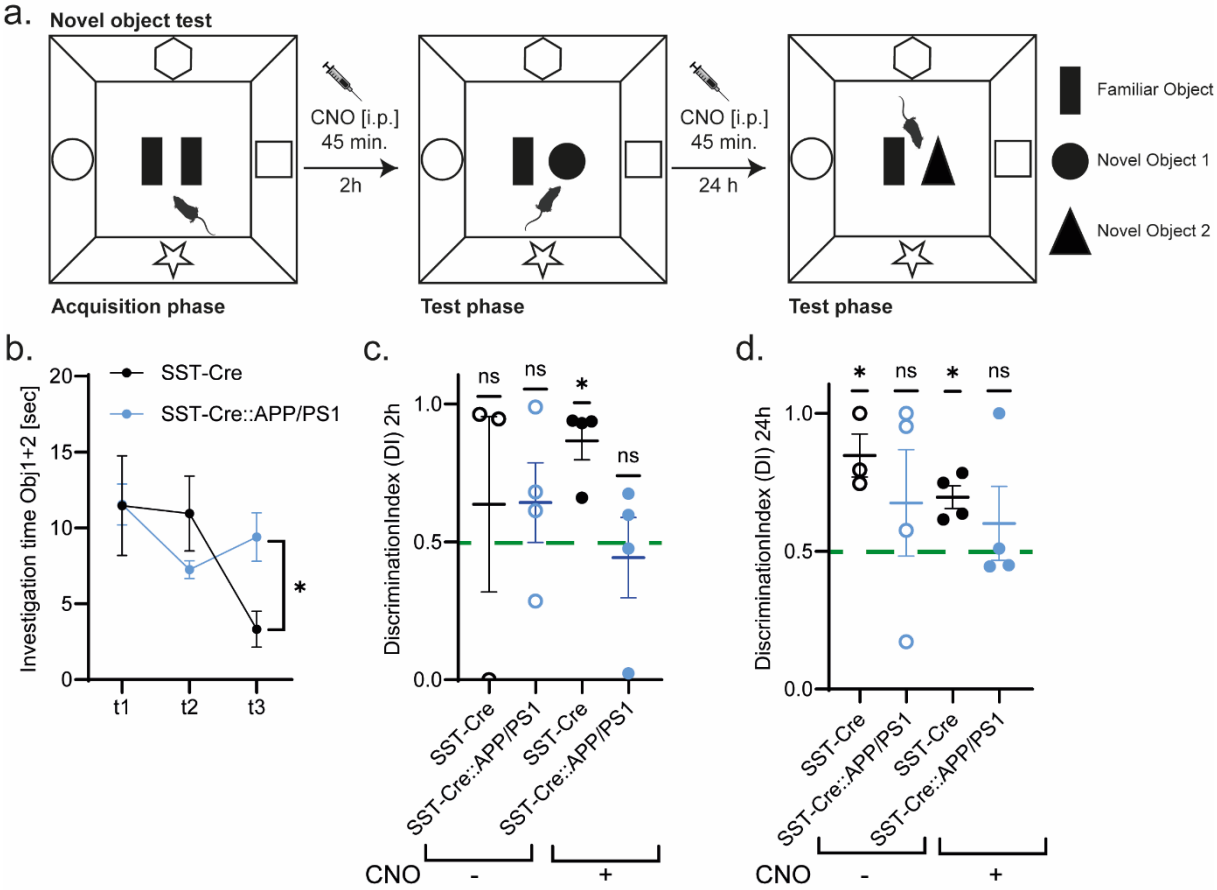

Figure 21. Chemogenetic silencing of vHPC SST$^+$ neurons in SST-Cre and SST-Cre::APP/PS1 mice in the NOR test. a. Schematic overview of the NOR paradigm. During the acquisition phase, mice explored two identical objects for habituation. For memory assessment, two test phases were conducted at 2 h and 24 h after acquisition, each preceded by i.p. injection of either CNO or saline 45 minutes prior to testing. In the 2 h test, one familiar object was replaced with a novel object (novel object 1), and in the 24 h test with a different novel object (novel object 2). The test evaluates recognition memory by measuring the animals' preference for novelty. **b.** Investigation time during the acquisition phase (t1–t3). SST-Cre animals (black circles) show a decline in exploration over time, indicative of successful object habituation. SST-Cre::APP/PS1 mice (blue circles) do not show the same decrease, suggesting reduced habituation. Two-way RM ANOVA with Sidak's post hoc test revealed a significant time effect ($p < 0.05$) and genotype × time interaction. **c.** DI at the 2 h test. SST-Cre/CNO$^+$ mice performed significantly above chance (green dashed line at DI = 0.5), indicating intact short-term memory. SST-Cre/CNO$^-$ animals failed to perform above chance. APP/PS1 mice, regardless of treatment (CNO$^-$ or CNO$^+$), did not show significant novelty preference, reflecting impaired short-term recognition memory. One-sample t-test vs. 0.5, $p < 0.05$; ns = not significant. **d.** DI at the 24 h test. Both SST-Cre/CNO$^-$ and SST-Cre/CNO$^+$ groups performed significantly above chance, suggesting preserved long-term memory in wild-type animals. In contrast, both APP/PS1 groups failed to perform above chance level, indicating long-term memory impairment. One-sample t-test vs. 0.5, $p < 0.05$; ns = not significant. Animals: SST-Cre/CNO$^-$: n = 3; SST-Cre::APP/PS1/CNO$^-$: n = 4; SST-Cre/CNO$^+$: n = 4; SST-Cre::APP/PS1/CNO$^+$: n = 4. Data are shown as mean ± SEM.

3.4. Behavioral Assessment of Structural and Functional Connectivity in Chrna2-Cre Mice

3.4.1. Converging Projections in the O-LM Layer of vHPC CA1 Identified by Bidirectional Tracing in Chrna2-Cre Mice

In the context of this study, the anatomical convergence of hippocampal-prefrontal connectivity within the O-LM layer of the CA1 region required precise labeling of a distinct interneuron population − named O-LM interneurons. Initially, an SST-Cre driver line was used to target SST^+ cells, which are typically enriched in the *stratum oriens*, to investigate the function of long-range inhibitory circuits. However, targeting O-LM interneurons with sufficient anatomical specificity using this line proved to be a significant technical challenge.

Previous work, including findings by (Müller-Komorowska et al. 2020) demonstrated that SST-Cre mice exhibit off-target expression, with reporter genes not only labeling SST^+ INs but also ectopically labeling PNs in the *stratum pyramidale*, particularly in the CA3 region. Such nonspecific labeling compromises the interpretation of circuit tracing experiments, especially when aiming to define long-range GABAergic projections or to distinguish between excitatory and inhibitory cell types within hippocampal-prefrontal networks. To overcome this methodological limitation and enhance cell-type specificity, we incorporated the Chrna2-Cre mouse line, a genetically refined model validated by (Leão et al. 2012) for its selective expression in O-LM interneurons. The Chrna2 gene encodes the *α2* subunit of the nicotinic acetylcholine receptor (α2-nAChR), which is restricted to a well-defined subset of GABAergic interneurons, including O-LM cells in the hippocampus, Martinotti cells in the neocortex, and Renshaw cells in the spinal cord.

To investigate the anatomical convergence of projection systems within the vHPC, I employed a dual-virus approach combining anterograde and retrograde tracing. Specifically, a Cre-dependent AAV carrying tdTomato (anterograde tracer) was injected into the vHPC in Chrna2-Cre mice, while an AAV retrograde encoding EGFP was delivered to the mPFC (Figure 22d) (Tervo et al. 2016). Retrograde tracing allows viral particles taken up by axon terminals in the mPFC to be transported back to their parent cell bodies in the vHPC, thereby labeling the specific population of vHPC neurons that projects to the mPFC. This approach enabled simultaneous labeling of axonal projections from the vHPC and retrograde transport from mPFC-projecting cells, facilitating high-resolution mapping of converging circuits.

In coronal hippocampal sections (Figure 22a), both anterograde ($tdTomato^+$) and retrograde ($EGFP^+$) fluorescent signals were observed predominantly in the CA1 region of the vHPC. These projections were especially limited to the O-LM layer, a layer enriched in long-range

inhibitory interneurons and a critical site for integrating cortical and hippocampal input. Higher magnification images (Figure 22b) revealed retrogradely labeled neuronal somata (EGFP$^+$) located specifically within the O-LM layer. Confocal imaging Figure 22c provided separate and merged views of anterograde and retrograde co-labeling labelled vHPC O-LM INs. The analysis demonstrated that labeled cells were confined largely to the O-LM layer. Quantitative evaluation identified three distinct populations: anterogradely labeled cells (tdTomato$^+$), retrogradely labeled cells (EGFP$^+$), and double-labeled (tdTomato$^+$/EGFP$^+$) cells. Here, approximately 50% of labeled neurons were double-positive, indicating a substantial overlap of projection pathways within this specific neuronal subpopulation. In summary, the combination of precise viral tracing and genetically refined mouse lines such as Chrna2-Cre provides an anatomically and functionally robust approach to dissecting the complex hippocampal-prefrontal networks involved in cognitive regulation and AD pathology.

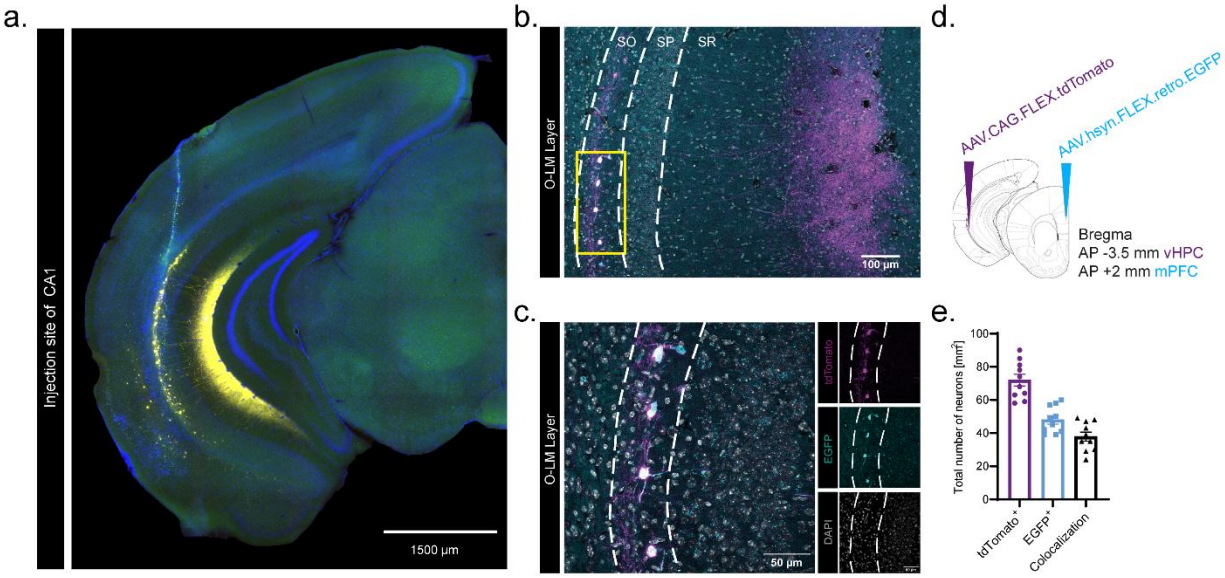

Figure 22. Anterograde and retrograde viral tracing in the CA1 region of the vHPC. a. Overview of a coronal brain section with tdTomato$^+$ and EGFP$^+$ expressing INs. The injection site is located in the vHPC, specifically in the CA1 region. **b.** Magnified view of the CA1 region showing retrogradely labeled neurons in the O-LM layer. White dashed lines show hippocampal layers: SO (*stratum oriens*), SP *(stratum pyramidale*), and SR (*stratum radiatum*). **c.** High-resolution image of the region highlighted in **(b),** showing separate channels for tdTomato$^+$ (anterograde, magenta), EGFP$^+$ (retrograde, cyan), and co-localization. Labeled neurons are primarily localized within the O-LM layer. **d.** Schematic representation of the experimental design, showing a retrograde injection of AAV1.syn.FLEX.retro.EGFP into the mPFC (cyan) and anterograde injection of AAV1.CAG.FLEX.tdTomato into the vHPC (magenta) in Chrna2-Cre mice. AP coordinates are given relative to Bregma: AP −3.5 mm (vHPC) and AP +2 mm (mPFC). **e.** Quantification of labeled neurons in the O-LM layer. Bar graph shows the number of tdTomato$^+$ (anterograde), EGFP$^+$ (retrograde), and double-labeled (colocalized) cells. The results indicate an overlap of ~50% of both projection types within the O-LM layer. n = 3; 3-4 vHPC sections/ animal.

3.4.2. Chemogenetic Activation of Chrna2^{+} Neurons in the vHPC of APP/PS1 Mice Using Excitatory DREADDs

As SST inhibition showed no significant effects, a gain-of-function strategy was implemented: in Chrna2-Cre mice, vHPC O-LM interneurons were chemogenetically activated (hM3Dq/C21) to test the function of direct long-range inhibitory projections to the mPFC. While inhibitory strategies primarily provide information about whether a certain cell population is necessary for a behavior, targeted activation makes it possible to check whether its recruitment is also sufficient to trigger or reinforce a specific function. This gain-of-function approach thus allows additional conclusions and helps to avoid potential compensatory network effects, which often complicate interpretation of inhibition studies. Especially in the context of the APP/PS1 model, in which an imbalance of excitatory-inhibitory signaling is described, activation is a suitable approach for directly testing the functional contributions of specific interneurons.

For these studies, Chrna2-Cre mice were crossed with APP/PS1 animals to produce offspring with the combination of Cre expression and APP/PS1 genotype (Chrna2-Cre::APP/PS1). These animals enable Cre-dependent expression of activating DREADDs in the disease-relevant genetic background.

To achieve selective activation of Chrna2-expressing interneurons in the vHPC, a Cre-dependent excitatory DREADD vector (AAV2.hSyn.DIO.hM3D(Gq).mCherry) was used. The viral construct was stereotactically injected into the vHPC of double-transgenic Chrna2-Cre::APP/PS1 mice (

Figure **23**a). The anatomical target within the vHPC is illustrated in

Figure **23**b After allowing at least three weeks for viral expression, animals underwent a series of behavioral tests, including OF, y-maze, NOR and cFC, as outlined in the experimental timeline (

Figure **23**c). After finishing the behavioral tests, histological analysis was done to check the specificity and localization of DREADD expression. In coronal brain sections from control animals without Cre recombinase (WT and APP/PS1) showed no mCherry signal; a representative image of an APP/PS1 mouse is shown in

Figure **23**d. In contrast, Chrna2-Cre and Chrna2-Cre::APP/PS1 mice showed clear hM3Dq expression in the vHPC, revealed by mCherry fluorescence in colocalization with DAPI-stained cell nuclei (represented in

Figure **23**e for a Chrna2-Cre mouse); confirming the Cre-dependent specificity of DREADD expression in Chrna2-Cre and Chrna2-Cre::APP/PS1 mice. High-resolution confocal images (

Figure **23**f) confirmed cellular localization of the mCherry signal within the CA1 region of the vHPC. DAPI staining provided clear nuclear contrast, allowing for easy identification of individual labeled neurons.

In summary, these results demonstrate the successful and spatially restricted expression of the excitatory DREADD construct in Chrna2^{+} neurons of the vHPC in the APP/PS1 background. The Cre-dependent chemogenetic system offers a precise tool to manipulate O-LM INs and assess their contribution to hippocampal-prefrontal circuit function and AD-related behavioral phenotypes.

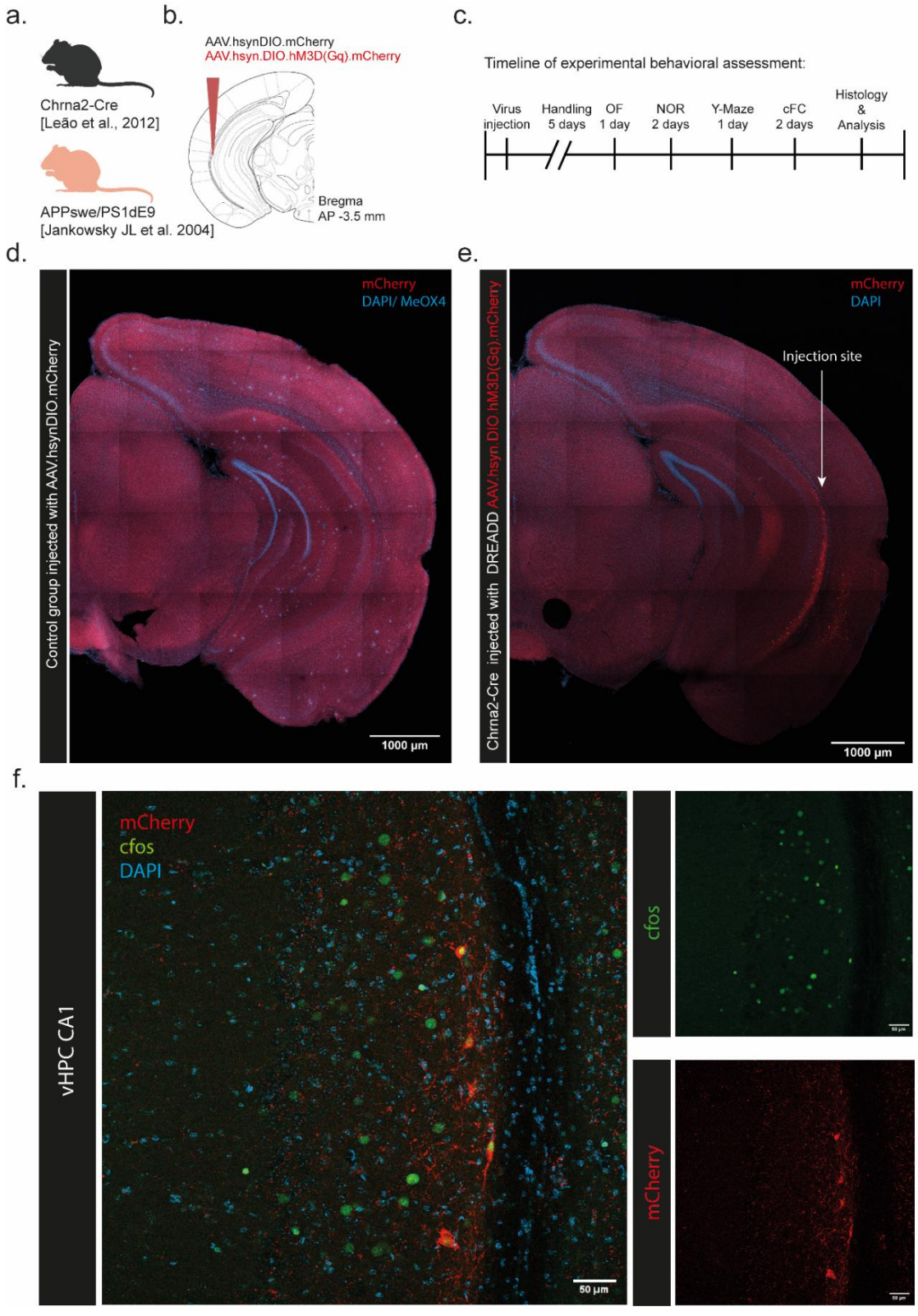

Figure 23. Chemogenetic activation of Chrna2^{+} neurons in the vHPC of Chrna2-Cre and Chrna2-Cre::APP/PS1 mice using excitatory DREADDs. a. Schematic representation of the transgenic mouse models: Chrna2-Cre mice (Leão et al., 2012) crossed with APP/PS1 mice (Jankowsky et al., 2004). **b.** Viral targeting strategy: Cre-dependent excitatory DREADD (AAV2.hSyn.DIO.hM3D(Gq).mCherry) or control virus (AAV.hSyn.DIO.mCherry) were injected into the vHPC (Bregma AP –3.5 mm). **c.** Timeline of the experimental procedure including viral injection, behavioral testing (OF, NOR, y-maze, cFC) and histological analysis.

d. Representative sagittal brain section from a control mouse injected with AAV.hSyn.DIO .mCherry, showing no mCherry expression in the vHPC, because of absence of Cre recombinase in APP/PS1 mice. DAPI labels nuclei and MeX04 (blue) marks Aß plaques.
e. Representative brain section from a Chrna2-Cre mouse injected with AAV2.hSyn.DIO.hM3D(Gq).mCherry. Strong mCherry expression confirms successful targeting of Chrna2^{+} cells in the vHPC. Injection site is indicated. **f.** High-magnification image (20x) from the vHPC CA1 region showing mCherry^{+} neurons (red), cFos^{+} nuclei (green), and DAPI (blue). Insets show single-channel views for cFos and mCherry.

After having confirmed specificity and functionality of my approach, I performed behavioral experiments while chemogenetically activating the vHPC O-LM INs.

For this study four groups were included: APP/PS1 wildtype animals which are referred from now on as WT and APP/PS1 transgenic animals, which received AAV.hSyn.DIO.mCherry injections into the vHPC and served as controls. Chrna2-Cre and Chrna2-Cre::APP/PS1 mice received AAV2.hSyn.DIO.hM3D(Gq).mCherry injections into the vHPC. Here, all mice received the DREADD agonist C21 30 min before each behavioral test. APP/PS1 and WT mice without DREADD expression served as internal controls to assess potential off-target effects of C21. In the DREADD cohorts specific activation of the O-LM interneurons was achieved through the Chrna2-Cre mice.

Figure 24b is showing the cumulative time spent in border zone for control and DREADD cohorts. The WT mice spent significantly less time in the border zone compared to APP/PS1 mice ($p < 0.05$), whereas no significant difference were detected in DREADD-expressing groups (Chrna-Cre and Chrna2-Cre::APP/PS1).

Similarly, time spent in the center zone (

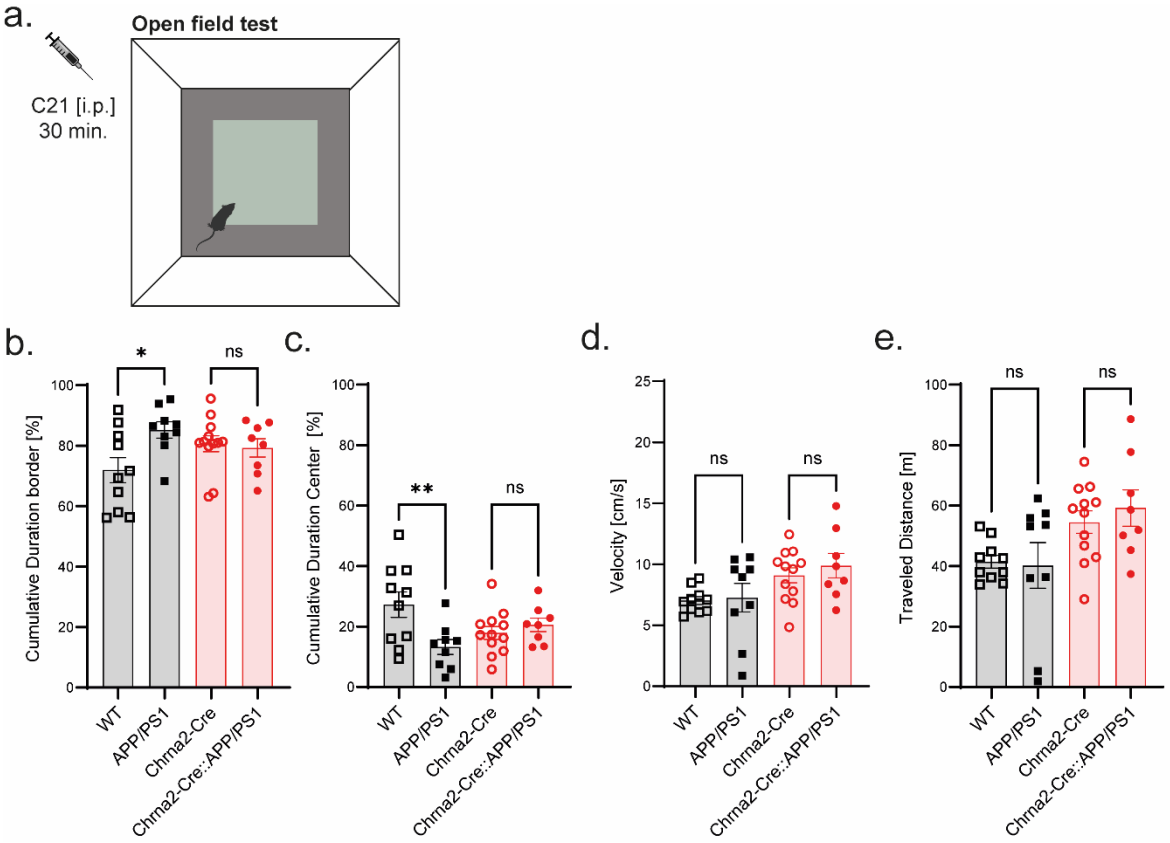

Figure **24**c) was significantly increased in WT animals compared to APP/PS1 mice ($p < 0.01$), but remained unchanged in Chrna-Cre and Chrna2-Cre::APP/PS1 mice.

No significant differences were observed in general locomotor parameters across all groups. Both mean velocity (

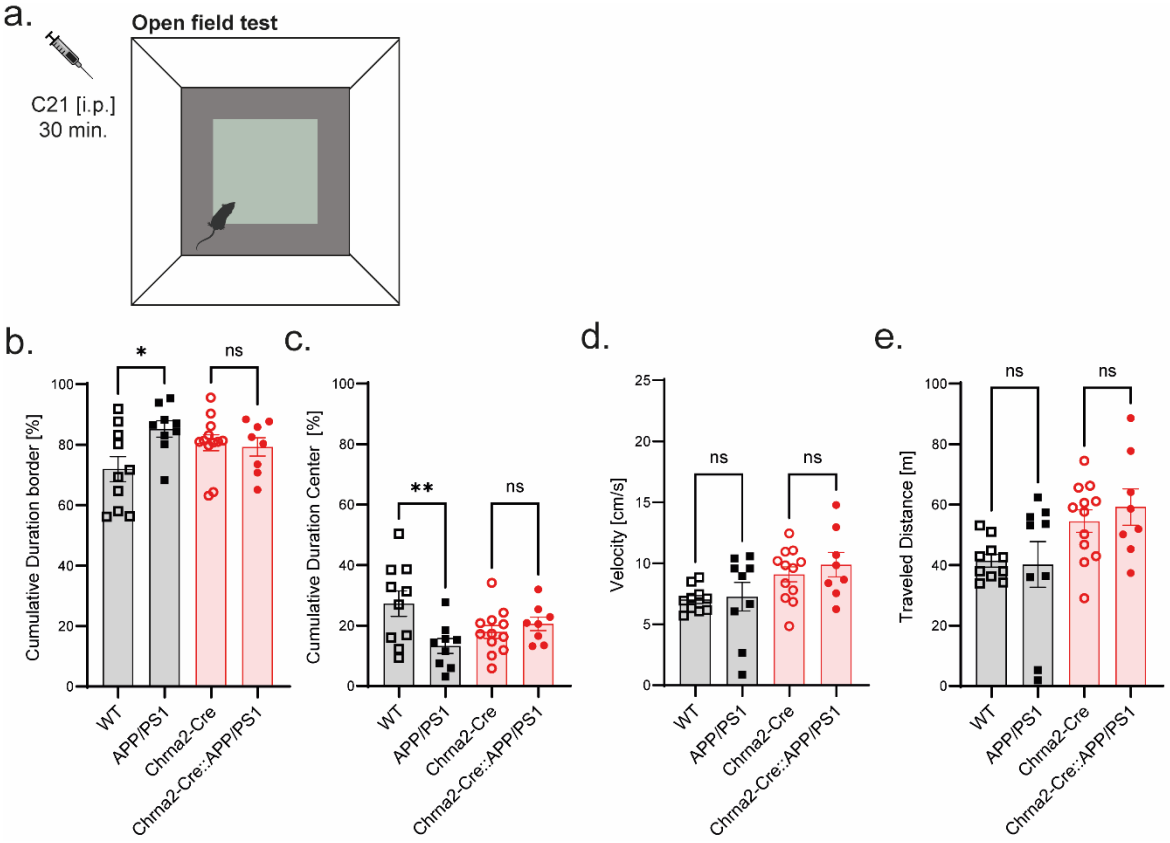

Figure **24**d) and total distance traveled (

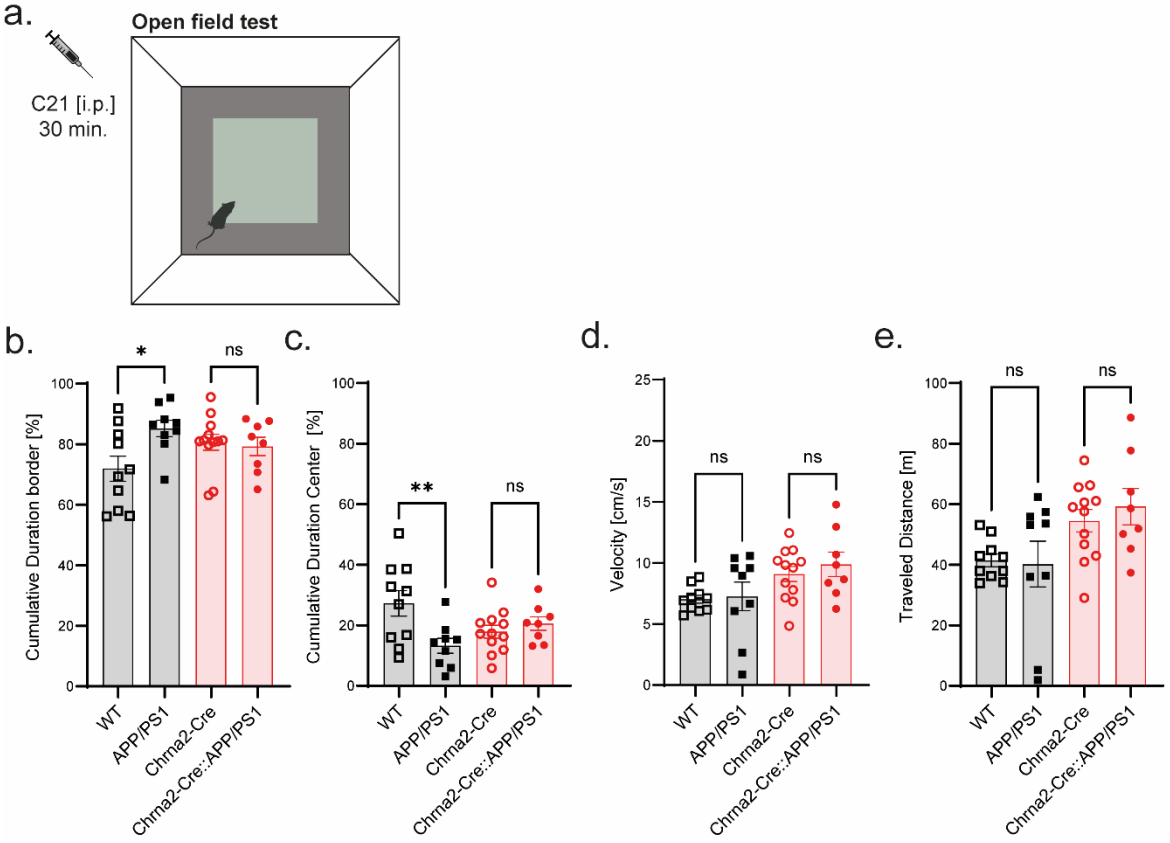

Figure **24**e) remained comparable ($p > 0.05$), suggesting that neither C21 injection alone nor DREADD activation affected overall mobility.

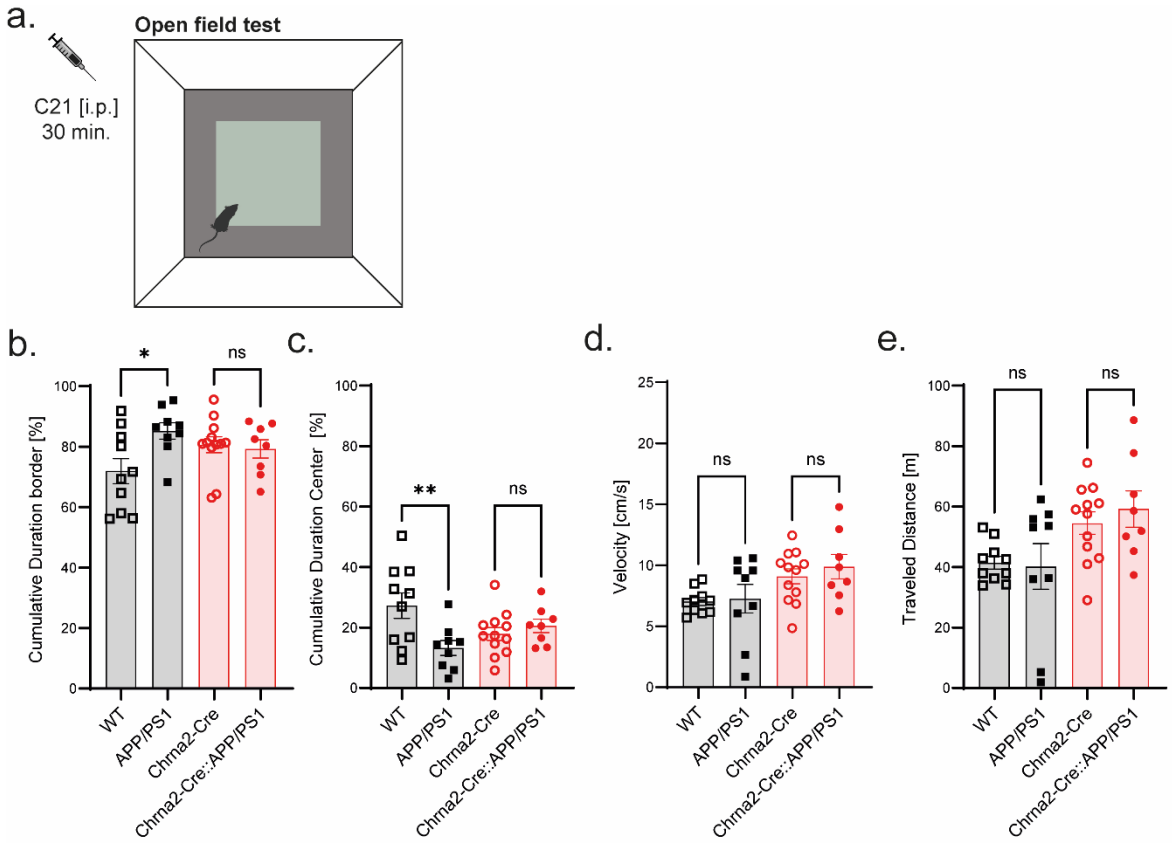

Figure 24. OF Test assessing anxiety-like behavior and locomotion after C21 administration. a. Schematic of the experimental setup. Mice received an intraperitoneal injection of C21 30 minutes before the OF test. **b.** Cumulative time spent in the border zone (%) differed significantly among groups (ordinary one-way ANOVA, $F(3,35) = 2.886$, $p = 0.0494$). Post hoc comparisons revealed that C21 significantly reduced border time in control mice ($p < 0.05$), but had no significant effect in DREADD-expressing animals. **c.** Time spent in the center zone (%) was significantly increased by C21 in control mice ($p < 0.01$), but remained unchanged in DREADD-expressing mice (ns). **d–e.** Locomotor parameters (velocity and distance traveled) did not differ significantly between groups, suggesting that C21 and DREADD activation did not affect general locomotion. Data are shown as mean ± SEM. Statistical analysis was performed using one-way ANOVA followed by multiple comparisons; Brown-Forsythe and Bartlett's tests confirmed homogeneity of variances ($p > 0.05$). Group sizes were as follows: WT ($n = 10$), APP/PS1 ($n = 9$), Chrna2-Cre::APP/PS1 ($n = 12$), and Chrna2-Cre ($n = 8$). Data are shown as mean ± SEM.

To evaluate short- and long-term recognition memory, the NOR test was performed. The experimental design consisted of a habituation and acquisition phase, followed by two memory test sessions: one at 2 hours post-acquisition (short-term memory) and another at 24 hours post-acquisition (long-term memory) (Figure 25a). Prior to each test phase, mice received an intraperitoneal injection of the DREADD agonist C21 (30 minutes before testing). Object exploration was tracked using DLC-based video analysis (Figure 25b). The DI, which quantifies the preference for novel over familiar objects, was analyzed 2 hours after acquisition (Figure

25c). The data revealed no significant differences in DI between groups at this time point. However, it showed that the Chrna2-Cre::APP/PS1 group exhibited a significantly above-chance DI ($p < 0.01$), while all other groups (WT, APP/PS1, Chrna2-Cre) did not show a significant preference for the novel object at 2 hours. At the 24-hour time point, no significant differences were observed above chance level (Figure 25d). This suggests all of the groups (WT, APP/PS1, Chrna2-Cre, Chrna2-Cre::APP/PS1) failed to distinguish the novel object from the familiar object after 24h, highlighting a potential impairment of long-term memory performance.

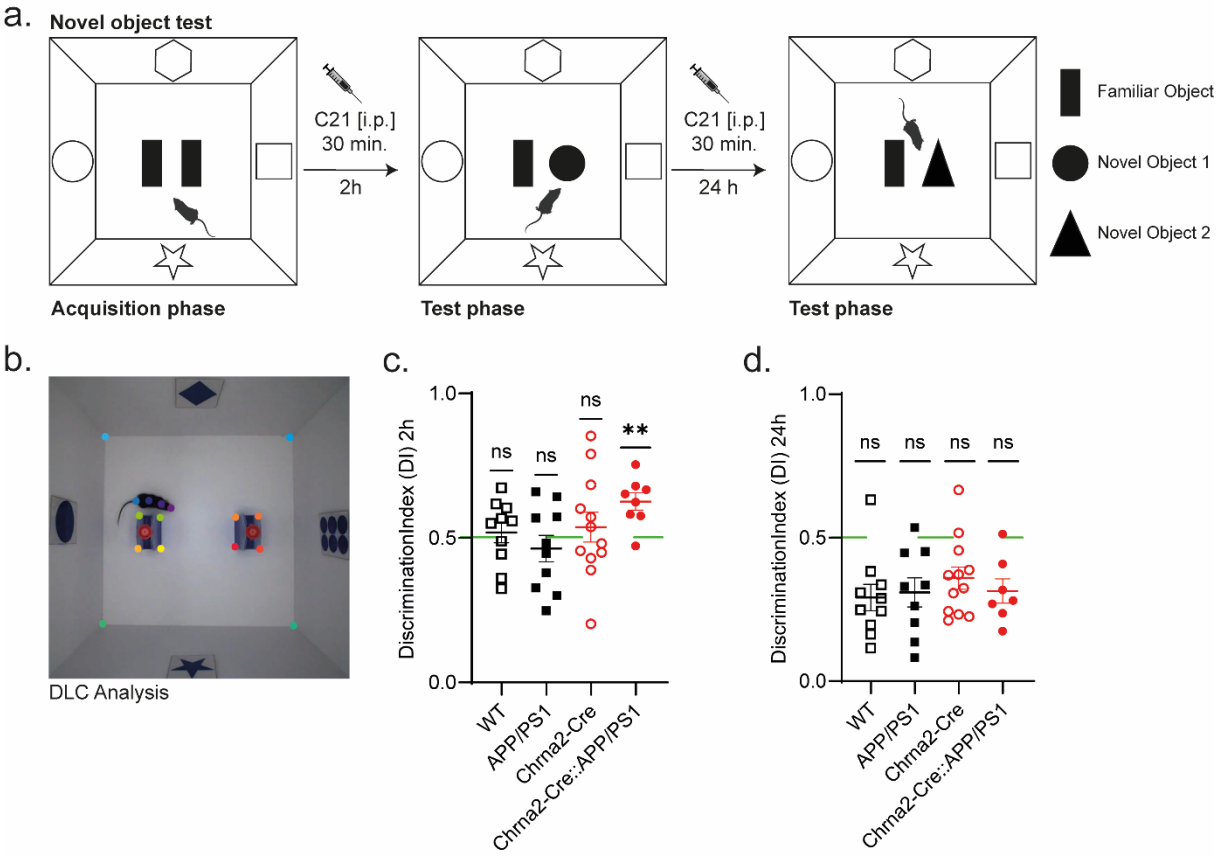

Figure 25. Novel object recognition test to assess short- and long-term memory. a. Schematic overview of the experimental design. Mice underwent a habituation phase (acquisition phase), followed by a short-term memory (2 h) and a long-term memory test (24 h). C21 was administered intraperitoneally 30 minutes prior to each test phase. **b.** Representative image of the open field arena with object placement. DLC analysis was used for automated tracking of object exploration. **c.** DI at 2 h post-acquisition. No significant differences were found across most groups (one-way ANOVA), except for the Chrna2-Cre::APP/PS1 group, which showed a DI significantly above chance level (0.5; $p < 0.01$, one-sample t-test vs. chance). **d.** DI at 24 h post-acquisition. WT, APP/PS1, Chrna2-Cre, and Chrna2-Cre::APP/PS1 groups showed DI values below chance level. Data are presented as mean ± SEM. Statistical analysis: one-way ANOVA with post hoc tests for group comparisons; one-sample t-tests were used to assess whether DI significantly differed from chance level (0.5). Group sizes: WT (n = 10), APP/PS1 (n = 10), Chrna2-Cre (n = 12), Chrna2-Cre::APP/PS1 (n = 8).

To evaluate spatial recognition memory, a y-maze test was conducted, which measures the animals' spontaneous preference for a novel arm following a restricted exploration phase. Mice received an intraperitoneal injection of the DREADD agonist C21 30 minutes prior to testing. The test consisted of two phases: sample phase: arm C was blocked, and animals were allowed to explore arms A and B for a predefined period. Choice phase: After a 60-minute delay, mice were returned to the maze with all three arms accessible, allowing free exploration (
Figure **26**a). Total distance traveled during the sample phase (
Figure **26**b) and the choice phase (
Figure **26**c) did not differ significantly among the experimental groups (one-way ANOVA, $p > 0.05$), indicating that general locomotor activity was comparable across genotypes and treatment conditions. The cumulative duration spent in the novel arm during the choice phase (
Figure **26**d) did not differ significantly between groups (one-way ANOVA, $p > 0.05$), suggesting no group-specific differences in spatial preference behavior. Similarly, the latency to first enter the novel arm (
Figure **26**e) did not vary significantly between groups, indicating that approach behavior toward the novel stimulus was unaffected by genotype or treatment. Lastly, the frequency of arm entries (
Figure **26**f) was comparable across all groups, further supporting the absence of alterations in exploratory drive or decision-making strategies. In summary, no statistically significant group differences were detected in any of the behavioral or locomotor parameters assessed in the y-maze test, indicating that spatial recognition performance under the applied conditions was not differentially affected across the tested genotypes.

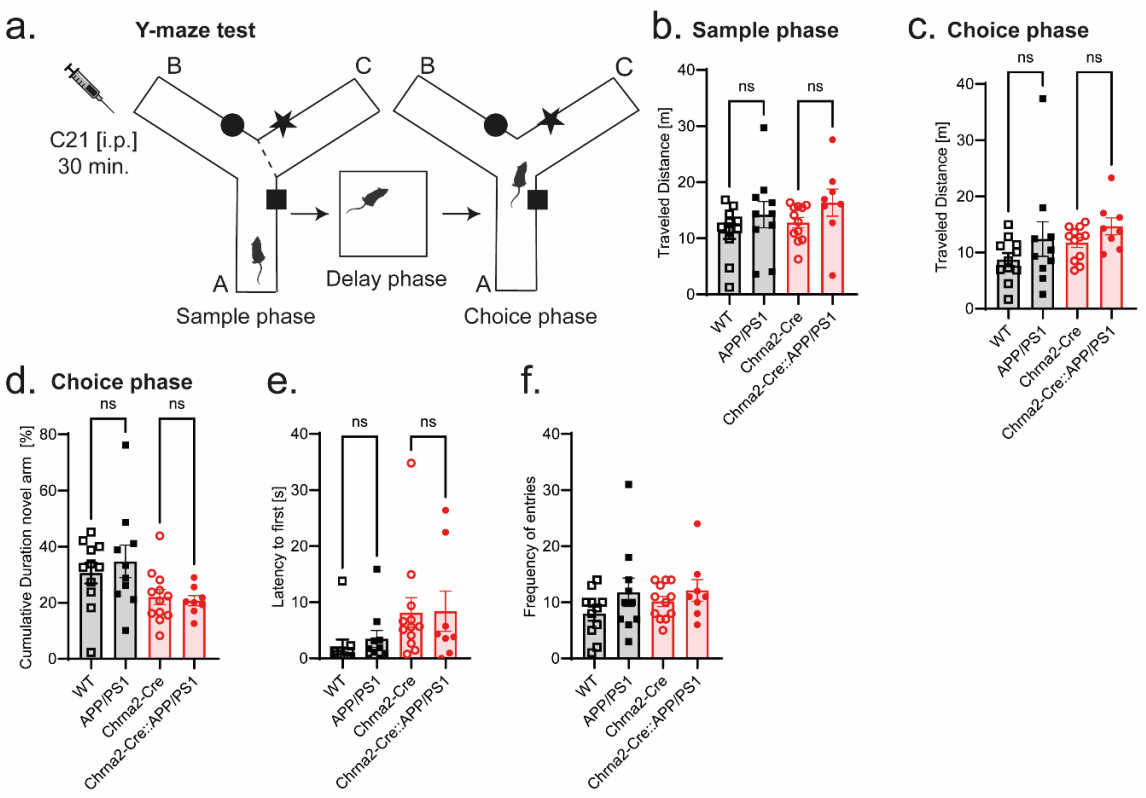

Figure 26. Y-maze test to assess spatial recognition memory in mice. a. Schematic of the y-maze paradigm. Mice were injected with C21 minutes before testing. During the sample phase, one arm (arm C) was blocked. After a delay of 60 minutes, mice were returned to the maze for the choice phase, where all arms were accessible. **b–c.** Total distance traveled (in meters) during the sample phase and choice phase did not differ significantly among groups, indicating no differences in general locomotor activity (one-way ANOVA, $p > 0.05$). **d.** Time spent in the novel arm during the choice phase was comparable across all groups. No significant effect of genotype or treatment was observed (one-way ANOVA, $p > 0.05$). **e.** Latency to first entry into the novel arm was not significantly different among groups. **f.** Frequency of entries into each arm also did not differ significantly across groups. Group sizes: WT (n = 11), APP/PS1 (n = 10), Chrna2-Cre (n = 12), Chrna2-Cre::APP/PS1 (n = 8). Data are presented as mean ± SEM. Statistical analysis was performed using ordinary one-way ANOVA followed by Šidák's multiple comparisons test.

To test associative fear memory animals were placed in a fear conditioning box for a total of 5 minutes. Electric shocks (0.75 mA) were applied at three time points: after 120, 182, and 244 seconds (Figure 27a). The freezing behavior across the individual shock intervals is shown in Figure 27b. APP/PS1 mice showed significantly reduced freezing behavior across the shock intervals compared to wild-type animals (***$p < 0.001$). Similarly, Chrna2-Cre::APP/PS1 mice showed significantly reduced freezing compared to Chrna-Cre wild-type animals (Figure 27c, ***$p < 0.001$). The total distance traveled during the acquisition phase decreased in all groups over the course of the session (Figure 27d). There were no significant group differences in locomotor activity.

On the second day, the animals were again placed in the same context box for five minutes without shocks being applied (Figure 27e). Analysis of freezing behavior revealed that Chrna2-Cre::APP/PS1 mice showed significantly less freezing than Chrna2-Cre animals (*$p < 0.05$), while no significant difference was observed between WT and APP/PS1 mice (Figure 27f). The distance covered during the test phase did not differ significantly between the groups, although a trend toward increased activity was observed in Chrna2-Cre::APP/PS1 mice compared to Chrna2-Cre animals (Figure 27g, $p = 0.0645$).

DLC-based tracking was used for quantitative recording of locomotion and freezing behavior (Figure 27h). The analysis of the motion trajectories (Figure 27i/j) shows examples of the motion patterns of two animals, including velocity profiles, distance curves, and freezing time courses.

These results document the behavioral responses of the different genotypes during acquisition and testing in the cFC paradigm under chemogenetic modulation of the vHPC.

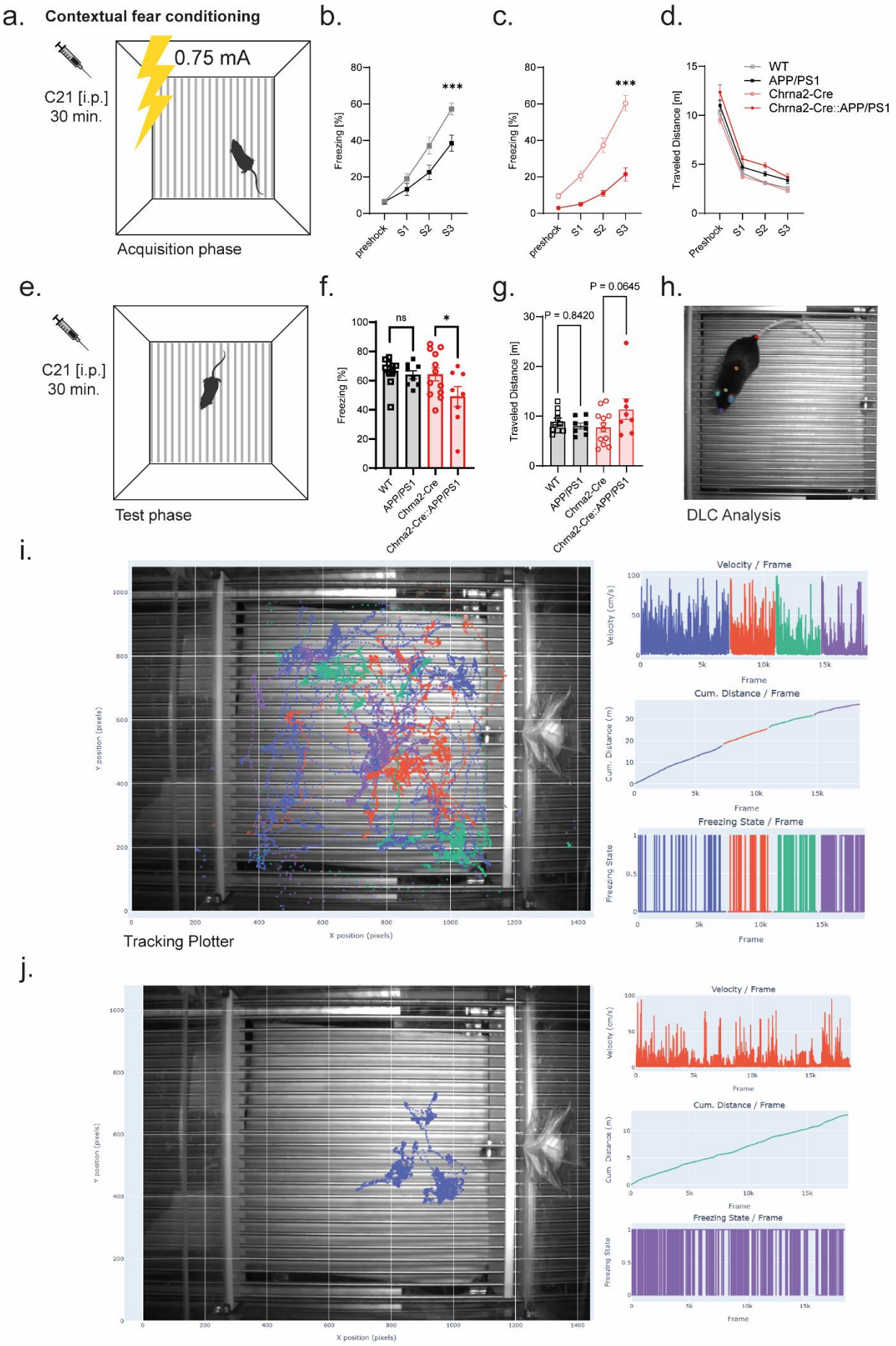
a.
Contextual fear conditioning
C21 [i.p.]
30 min.
0.75 mA
Acquisition phase
b.
Freezing [%]
***
preshock
S1
S2
S3
c.
Freezing [%]
***
preshock
S1
S2
S3
d.
Traveled Distance [m]
WT
APP/PS1
Chrna2-Cre
Chrna2-Cre::APP/PS1
Preshock
S1
S2
S3
e.
C21 [i.p.]
30 min.
Test phase
f.
Freezing [%]
ns
*
WT
APP/PS1
Chrna2-Cre
Chrna2-Cre::APP/PS1
g.
Traveled Distance [m]
P = 0.8420
P = 0.0645
WT
APP/PS1
Chrna2-Cre
Chrna2-Cre::APP/PS1
h.
DLC Analysis
i.
Y position (pixels)
X position (pixels)
Tracking Plotter
Velocity / Frame
Velocity (cm/s)
Frame
Cum. Distance / Frame
Cum. Distance (m)
Frame
Freezing State / Frame
Freezing State
Frame
j.
Y position (pixels)
X position (pixels)
Velocity / Frame
Velocity (cm/s)
Frame
Cum. Distance / Frame
Cum. Distance (m)
Frame
Freezing State / Frame
Freezing State
Frame

Figure 27. Contextual fear conditioning reveals enhanced freezing responses in mice. a. Schematic of the acquisition phase: Mice received an intraperitoneal injection of C21 (3µg/g; i.p.) 30 minutes prior to training. Animals were exposed to a conditioning context and received three foot shocks (0.75 mA, 2 seconds each) with 1-minute intervals between shocks, over a total session duration of 5 minutes. **b.** Time course of freezing behavior during the acquisition phase in wild-type and APP/PS1 mice. While freezing increased across all shock trials (S1–S3), wild-type mice showed significantly higher freezing at S2 ($p = 0.0050$) and S3 ($p = 0.0003$) compared to APP/PS1 (Šidák's multiple comparisons following mixed-effects analysis). **c.** Freezing behavior during acquisition in Chrna2-Cre and Chrna2-Cre::APP/PS1 mice showed a similar profile, with no significant between-group differences. **d.** Total distance traveled decreased across trials (Pre, S1–S3), indicating habituation to the environment. No group differences were observed. **e.** Schematic of the test phase: Mice were re-exposed to the same context 24 h later after C21 injection (30 min prior). **f.** Freezing behavior in the test session. Chrna2-Cre::APP/PS1 mice exhibited significantly increased freezing compared to Chrna2-Cre ($p < 0.05$), indicating exaggerated fear memory expression. **g.** Distance traveled during the test phase did not differ significantly between groups (all $p > 0.05$). **h.** Representative image of DLC-based tracking during the cFC test. **i–j.** Examples of movement trajectories and behavior analyses from individual mice generated using tracking and velocity data. Color coding reflects locomotor speed and freezing probability. Group sizes: WT (n = 10), APP/PS1 (n = 10), Chrna2-Cre (n = 12), Chrna2-Cre::APP/PS1 (n = 8). Data are shown as mean ± SEM. Statistical analyses: mixed-effects model with Šidák's correction for multiple comparisons; $p < 0.05$ (*), $p < 0.01$, $p < 0.001$ and ordinary one-way ANOVA followed by Šidák's multiple comparisons test.

3.5. Functional Mapping of mPFC Neural Activity During Reward-Based Learning Using Two-Photon Microscopy

To investigate dynamic neuronal activity patterns in the mPFC of awake, behaving mice, I employed a two-photon Ca^{2+} imaging approach. This technique enables high-resolution optical recordings of Ca^{2+} transients as a proxy for neuronal activation in deep cortical layers. This method provides a powerful platform for examining how the mPFC integrates contextual and spatial information during goal-directed behavior, with particular relevance for dissecting prefrontal dysfunction in Alzheimer's disease models. For this purpose, mice were injected with an AAV encoding the genetically encoded calcium indicator GCaMP6f (AAV1.CamKII.GCaMP6f.WPRE.SV40) into the mPFC. Following the injection, a prism-based imaging window was surgically implanted to permit chronic access to the cortical region of interest in the dACC and PL area. A representative coronal brain section confirms robust and spatially restricted expression of GCaMP6f within the mPFC, validating accurate targeting and efficient viral transduction, which provided stable optical access, allowing both high cellular resolution and long-term measurements (Figure 28.

During imaging sessions, head-fixed mice were first positioned on a turntable (test imaging) (Figure 28. and later on a linear treadmill (Figure 28a/b) and engaged in a spatial learning task (Figure 12). This behavioral paradigm involved the identification of one reward zone (~190

cm) based on self-motion cues. Fluorescence signals were recorded from neuronal populations in deep layers of the mPFC at depths of approximately 1100 µm.

Motion correction was performed with CaImAn to minimize motion artifacts that can be caused by breathing, heartbeat, or slight head movements. The fluorescence images showed clear Ca^{2+} transients in individual neurons with amplitudes of up to 220% ΔF/F (Figure 28c). These pronounced signal changes indicate strong changes in intracellular calcium concentration and thus high neuronal activity. The simultaneous imaging of 120 cells revealed a broad spectrum of individual activity profiles, ranging from short, high-amplitude peaks to longer, flatter signal curves. This allows both phasic and tonic activity patterns in the neural network of the mPFC to be recorded.

The resulting image showed a significant improvement in signal stability and a clearer description of individual cell bodies, enabling reliable time series to be extracted (Figure 28e/f). This correction was crucial in order to clearly distinguish activity-based signal changes from background noise respectively neuropil activity.

The data obtained demonstrate that this approach can be used to capture large-scale activity patterns *in vivo* at the single-cell level. The observed Ca^{2+} transients reflect dynamic processes within the prefrontal network and thus form a functional basis for linking neuronal population activity with cognitive or behaviorally relevant parameters. At the same time, the analysis highlights the need for methodological corrections in order to derive valid statements about neuronal dynamics.

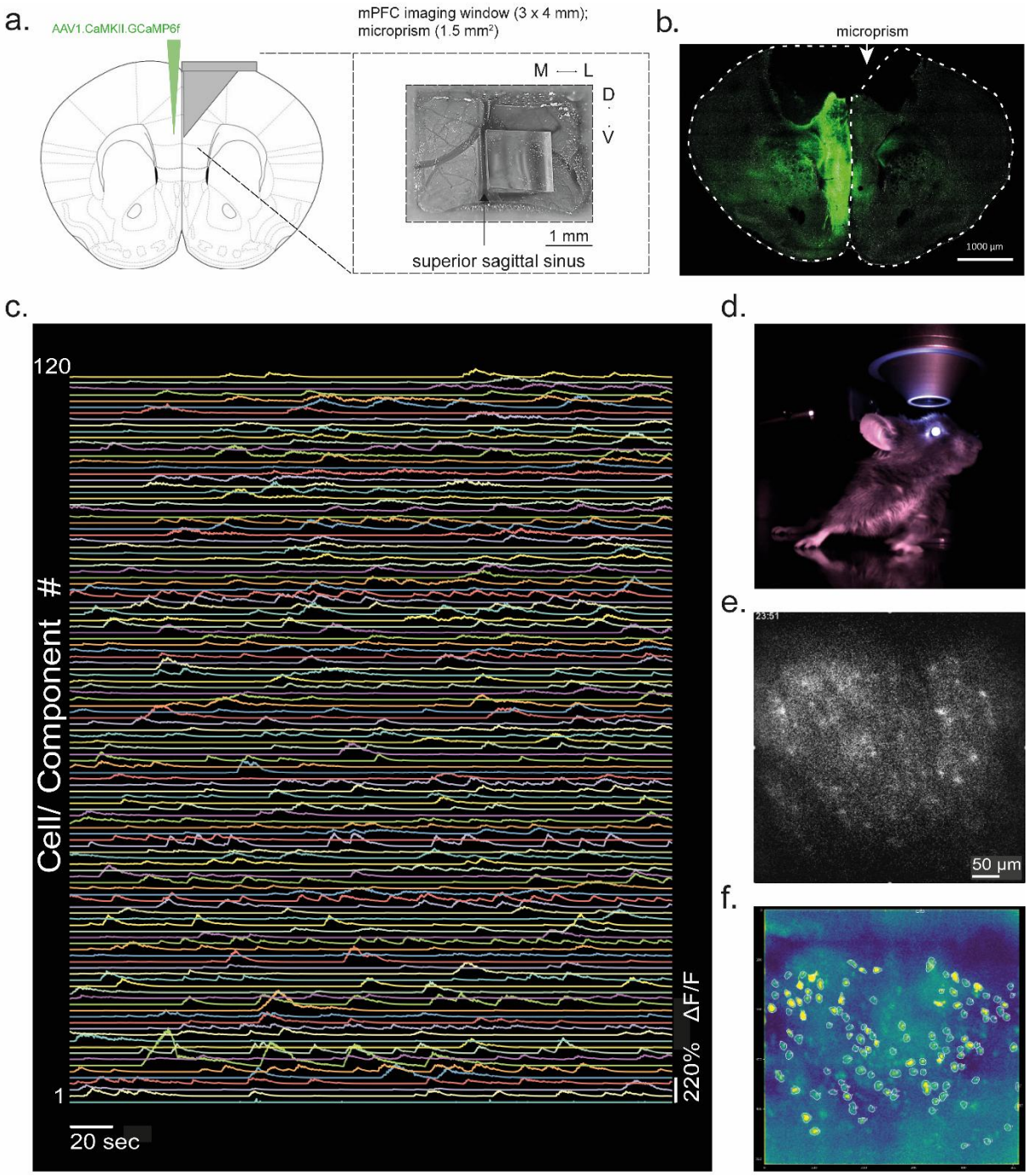

Figure 28. In vivo two-photon Ca^{2+} imaging of neuronal activity in the mPFC. a. Schematic representation of viral delivery (AAV1.CaMKII.GCaMP6f) and implantation of a microprism window (3 × 4 mm) for optical access to the mPFC. **b.** Histological verification of GCaMP6f expression (green) and prism placement. Scale bar: 1000µm. **c.** Simultaneous calcium activity traces of 120 identified neurons, showing robust transients with amplitudes up to ~220% ΔF/F. Temporal scale bar: 20 sec. **d.** Experimental setup illustrating a head-fixed mouse on a turntable under the two-photon microscope during Ca^{2+}-imaging. **e.** Motion-corrected maximum intensity projection of active neurons at 900-1000 µm depth. Scale bar: 50µm. **f.** Correlation image derived from CaImAn analysis, illustrating the spatial footprints of segmented neurons and their distribution across the imaging plane.

In a representative 15-month-old APP/PS1 mouse, task-related behavioral performance and calcium activity were successfully recorded. The following figure illustrates the experimental procedure and the simultaneous recording of behavior and neural activity using an *in vivo* Ca^{2+} imaging setup (Figure 29). During the experiments, mice were head-fixed and performed locomotion on a treadmill while being imaged under a two-photon microscope, which enabled the simultaneous monitoring of running behavior and Ca^{2+}dependent neural activity in the mPFC (Figure 29 a/b). At imaging depths of 900-1000 µm, individual cell bodies could be resolved after motion correction, as illustrated by the maximum intensity projection (Figure 29c). The corresponding heatmap representation further emphasizes the presence of GCaMP-expressing and actively firing neurons (Figure 29d). This preprocessing not only improves the visualization of neuronal activity but also facilitates the reliable separation of cell-specific signals from background fluorescence, thereby ensuring accurate extraction and subsequent analysis of neuronal activity patterns. The extracted calcium time series are summarized in Figure 29e/f, which displays the activity of 245 identified cells and demonstrate temporally resolved fluctuations in fluorescence intensity (ΔF/F) corresponding to task-related neural activity. Each row represents a single neuron, and the trace captures dynamic population responses across time. Numerous cells exhibited synchronous Ca^{2+} transients, indicative of coordinated network dynamics that occurred during the animal's running behavior. In parallel, locomotor behavior was quantified. Figure 29f depicts the time course of running velocity, characterized by alternating periods of variable speed and brief pauses. Panel g depicts the animal's position on the treadmill as a function of time, color-coded according to velocity. Strikingly, the animal consistently reduced its speed around 190 cm − a location corresponding to the predefined reward zone. This deceleration provides a clear behavioral correlate of the reward contingency and demonstrates that the animal might remember the reward location across repeated trials.

For a more detailed behavioral assessment, licking behavior was recorded as an additional measure. Panel h shows the average licking rate as a function of position on the treadmill. A marked increase in licking activity was observed exclusively within the reward zone, corroborating the interpretation from panel g. The combined observation of reduced velocity and elevated licking activity at the same spatial location provides compelling evidence that the animal had learned to reliably identify and anticipate the reward zone.

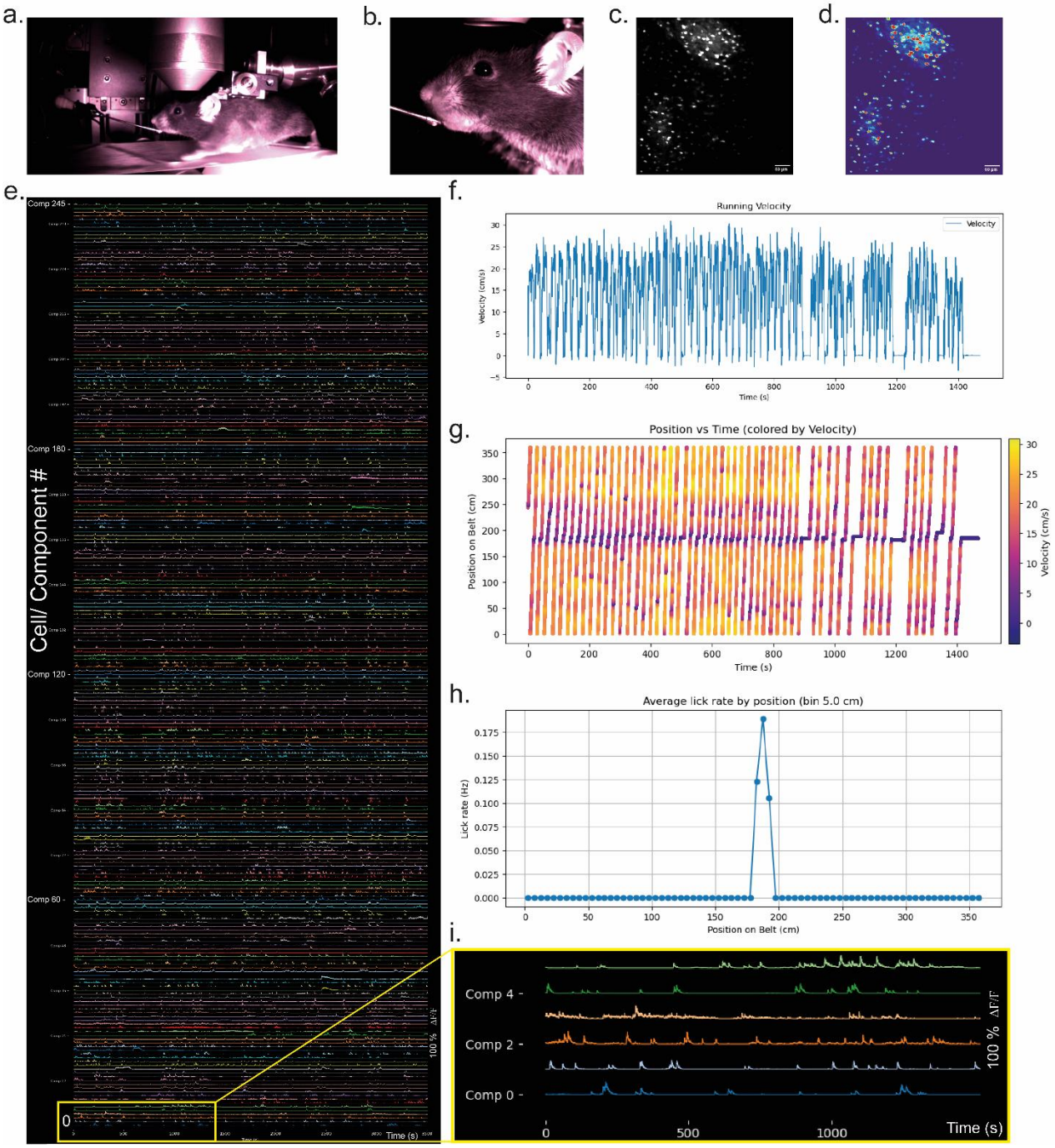

Figure 29. ***In vivo*** **Ca^{2+}-imaging of neuronal activity in the mPFC during learning performance in a linear treadmill task. a. & b.** Experimental setup showing a head-fixed mouse running on a treadmill while positioned under a two-photon microscope. **c.** Motion-corrected maximum intensity projection of active neurons at ~900-1000 µm depth. **d.** Heatmap of motion corrected maximum intensity projections, illustrating the spatial footprints of segmented and GCaMP-expressing neurons within the field of view. **e.** Ca^{2+}-activity traces from 245 identified neurons recorded simultaneously; each line represents ΔF/F fluorescence changes of a single neuron over time. **f.** Running velocity of the mouse over the course of the imaging session. **g.** Position of the animal on the treadmill as a function of time, color-coded according to velocity. **h.** Average lick rate as a function of position, revealing a sharp increase in licking behavior specifically within the reward zone (~190 cm), consistent with location-specific reward expectation. **i.** Magnified view of Ca^{2+} traces from selected neurons (highlighted in **e**), demonstrating activity patterns during reward-related behavior. Scale bar: 100% ΔF/F.

4. Discussion

The hippocampus and medial prefrontal cortex (mPFC) form a crucial network that facilitates working memory. Especially during spatial working memory tasks, both regions show coordinated activity, with the hippocampus encoding spatial information and the mPFC storing and using this information. The functional coupling between the hippocampus and the mPFC, specifically through synchronized theta and gamma oscillations, is essential for effective working memory performance. Impairments in this connection are known to lead to deficits in spatial working memory, as has been observed in animal models. Overall, this interaction supports the adaptive use of contextual and spatial information within working memory.

In this work, my goals were (1) to anatomically map the projections of the hippocampus to the prefrontal cortex in Cre driver-specific mouse lines using cell type-specific viral tracings, (2) to investigate the functional significance of these pathways for spatial working memory by selectively silencing or activating defined inputs, and (3) to determine how interneuron networks, particularly somatostatin-positive O-LM interneurons, may contribute to the mechanisms of spatial working memory. No statistically significant results were obtained in the experiments, primarily because of methodological limitations and low sample sizes. However, several consistent trends were observed that strongly suggest that these manipulations may show robust effects on hippocampus-prefrontal cortex communication in larger cohorts.

Taken together, these results show, that projections between the hippocampus and prefrontal cortex hint an important basis for linking spatial information with working memory processes and that selective interneuron populations may play a central role in shaping this integration. In the following sections, I will discuss my results in the context of the existing literature, methodological considerations, limitations of this study, and possible future directions.

4.1. Functional organization and network modulation of the ventral hippocampus: From global inhibition to cell type-specific mechanisms

The aim of this study was to characterize the structural and functional significance of the interaction between the vHPC and mPFC in the context of spatial working memory processes under AD-like conditions. Specifically, the role of SST^+ and O-LM interneurons in the CA1 region of the hippocampus and their influence on network modulation and the maintenance of an excitatory-inhibitory balance.

4.1.1. Broad vHPC Silencing

In the first experiment, the test animals were divided into two groups: a treated group (CNO/DREADD) and a control group (saline/DREADD). All animals first received bilateral injections of the inhibitory designer receptor AAV2.hSyn.DIO.hM4D(Gi).mCherry into the vHPC to enable global inhibition of this region.

The animals underwent a series of standardized behavioral paradigms specifically targeting the functional role of the vHPC in emotional, locomotive, cognitive, and mnemonic processes.

The findings showed that global inhibition of the vHPC did not significantly reduce overall locomotor activity or cause a change in anxiety avoidance (time spent in the center), which indicates preserved motor function and only minor impairment of anxiety-associated regulation. The vHPC is considered a central structure in the regulation of anxiety- and stress-associated behaviors and in the mediation of emotional contextual memory (Bannerman et al. 2004; Fanselow und Dong 2010). In particular, lesion and inactivation studies show that vHPC dysfunction can lead to reduced anxiety behavior in the open field and elevated plus maze, while the dorsal hippocampus is primarily relevant for spatial-cognitive functions (Kjelstrup et al. 2002; Bannerman et al. 2014).

However, the results of this experiment show that global chemogenetic inhibition of the vHPC using hM4D(Gi) did not cause any significant changes in locomotion or thigmotaxis (center-border preference) in the open field. The results partially differ from classic lesion studies, which often report a significant reduction in anxiety-like behavior after vHPC manipulations (Kjelstrup et al. 2002; Felix-Ortiz et al. 2016).

One possible explanation could be that the DREADD inhibition used in this study represents a more subtle modulation than irreversible lesions or acute pharmacological inhibitors. For example, the activation of hM4D(Gi) primarily influences the firing rate and synaptic activity, while the integrity of the network architecture remains intact (Roth 2016; Armbruster et al. 2007). This could have led to a partial but not complete suppression of vHPC output signals, thereby largely preserving basic behaviors such as locomotion.

In addition, the vHPC is embedded in a broad network with the amygdala and prefrontal cortex (Sierra-Mercado et al. 2011; Padilla-Coreano et al. 2016). Compensatory mechanisms within these networks may have ameliorated the consequences of acute vHPC inhibition. In particular, amygdala-centered circuits may maintain anxiety behavior even when vHPC activity is suppressed, which would explain the absence of effects in the OF.

Global chemogenetic inhibition of the vHPC in wild-type animals did not lead to statistically significant changes in the behavioral tasks tested. A slight trend was visible, but the number of

animals per group was likely to small. This means that the chance of missing a real effect is high, and the data cannot be taken as evidence against a role of the vHPC. From a methodological point of view, it is also important to note that global inhibition of the vHPC influences many different cell types at the same time. Since these populations can have opposite functions, their combined manipulation may cancel out real effects.

4.1.2. SST Circuit Manipulation in AD Model

Evidence from previous studies shows that SST^+ interneurons are important for maintaining synchrony between the vHPC and the mPFC. This synchrony allows the prefrontal cortex to reliably access hippocampal signals, which is essential for memory and emotional regulation emotional regulation (Padilla-Coreano et al. 2016; Tamura et al. 2017; Abbas et al. 2018). Work by (Schmid et al. 2016) further demonstrates that this mechanism is disrupted in Alzheimer's disease. In APP/PS1 mice, SST-positive O-LM interneurons display structural impairments, including axonal loss in the SLM layer and abnormal spine dynamics. At the same time, their cholinergic input from the MS is reduced.

In this context, based on the SST^+ circuitry, my study provides the first identification of direct LRIPs from the vHPC to the mPFC. A direct inhibitory SST^+ pathway between these two regions has not been described before, and its exact function remains unclear. Since hippocampal-prefrontal communication is critical for both memory and emotion regulation, understanding the contribution of these inhibitory LRIPs is important, especially under Alzheimer-like conditions.

To answer this question, I conducted a pilot study in which I performed chemogenetic manipulations on vHPC SST^+ neurons in a double transgenic APP/PS1 mouse model. In combination with classical behavioral paradigms, I conducted a preliminary assessment of whether vHPC SST^+ projections are involved in memory and behavior during the course of the disease. For the experiment, the animals were divided into two groups that differed in terms of both their genotype and treatment. The control groups included SST^+ and SST^+::APP/PS1 mice, while the treatment groups had the same genotype but underwent chemogenetic activation. For this purpose, all groups received bilateral stereotactic injections of the viral vector AAV2.hSyn.DIO.hM4D(Gi).mCherry into the vHPC, which led to the expression of the inhibitory DREADD receptor hM4D(Gi).

This procedure ensured that all observed behavioral differences could be attributed to the manipulation of the vHPC and not to nonspecific effects of CNO administration or viral transduction.

The results showed that chemogenetic silencing of SST^+ neurons in the vHPC did not produce any significant effects in the tests. This could be related to previous findings suggesting that the SST-Cre mouse line has methodological limitations in relation to its specificity. Their results showed that Cre recombination in this line does not just occur in GABAergic interneurons, but also is found in excitatory CA3 pyramidal cells (Müller-Komorowska et al. 2020). (Mikulovic et al. 2018) also demonstrated that SST-Cre mice were not restricted to O-LM cells; they were observed in various CA1 layers, in the DG, and in CA3. They suggest limited specificity of the Cre lines used, in which excitatory projection neurons can also be labeled and activated. This nonspecific expression may have significant functional consequences, as optogenetic or chemogenetic manipulations no longer specifically target inhibitory networks but also modulate excitatory projections. This is because large excitatory postsynaptic currents (EPSCs) were observed in the target regions after optogenetic stimulation in some Cre lines.

4.1.3. Chrna2-Cre Circuit Manipulation in AD Model

To overcome the problems of non-specificity of the SST-Cre line, the Chrna2-Cre mouse line was incorporated into the experiments. This line allows selective manipulation of O-LM interneurons that express the α2 subunit of the nicotinic acetylcholine receptor (Leão et al. 2012).

O-LM interneurons play a special role in the hippocampal network because their projections also target the distal dendrites of CA1 pyramidal cells, helping to balance inputs from the entorhinal cortex and Schaffer collaterals (Leão et al. 2012; Klausberger und Somogyi 2008). In this way, they influence whether contextual information from the hippocampus or sensory information from the entorhinal cortex is integrated into CA1. Optogenetic studies have shown that activation of OLMα2 cells can modulate memory processes bidirectionally: activation during encoding impairs object memory, while inhibition significantly improves object encoding (Mikulovic et al. 2018). An important aspect here is the phase-specific effect, which shows that manipulations outside the encoding phase or during periods without active exploration had no effect. This demonstrates the high temporal sensitivity of these interneurons during learning. Here, the OLMα2 cells also influence fear-related memories. Their activation reduces the consolidation of fear memories, while inhibition has no effect (Lovett-Barron et al. 2014). These findings demonstrate the complexity and bidirectional control of memory processes by this interneuron population. Another important mechanism is their role in generating theta oscillations. Optogenetic stimulation of OLMα2 interneurons in the ventral hippocampus can induce theta-2 oscillations (3-8 Hz) both under anesthesia and in the awake

state, which in turn modulate gamma activity in the range of 60-80 Hz. Since theta-gamma coupling is considered a key mechanism for synchronicity between the hippocampus and prefrontal cortex as well as for memory encoding (Buzsáki und Wang 2012; Colgin 2011), these findings confirm the central importance of OLMα2 cells for controlling network dynamics. Behavioral effects were also demonstrated: the stimulation of OLMα2 cells to induce theta-2 activity promoted risk-taking behavior in response to anxiety-inducing stimuli (e.g., the smell of a predator), while the inhibition of these cells reduced both the oscillations and the associated behavior.

This switch resulted in more selective and reliable labeling of O-LM interneurons, providing a higher-resolution and functionally interpretable map of afferent connectivity in the vHPC. Functionally, α2-nAChR-expressing interneurons are known to be important regulators of recurrent inhibitory microcircuits and are involved in the modulation of memory and learning processes. Importantly, OLMα2 cells can have bidirectional control over memory encoding:
an activation impairs object memory but improves object recognition and disrupts fear memory encoding, while inhibition can improve object memory.

Given this functional relevance and anatomical precision, the Chrna2-Cre line offered a powerful alternative to SST-Cre mice. It allowed us to isolate O-LM interneurons with minimal off-target expression and robustly examine the anatomical convergence of mPFC- and vHPC-derived projections within this specialized inhibitory microcircuit. Therefore, the switch from SST-Cre to Chrna2-Cre mice was not only methodologically justified but also crucial for the validity and specificity of our findings on inhibitory long-range connectivity in Alzheimer's-related circuits.

The tracing studies performed in this study also confirmed, as demonstrated previously in SST-Cre and Chrna2-Cre mice in the results the existence of direct inhibitory long-range projections from O-LMα2 interneurons in the ventral hippocampus to the medial prefrontal cortex.

For this reason, the following experiment, the vHPC was chemogenetically activated via hM3Dq in Chrna2-Cre and Chrna2-Cre::APP/PS1 mice to examine the contribution of cholinergically modulated OLMα2 interneurons to emotion, locomotion, recognition, and working memory processing, as well as fear memory. Here, the experimental animals were divided into four groups, which differed in terms of both genotype and treatment. The control groups, consisting of wild-type mice and transgenic APP/PS1 mice, and the treated groups, consisting of Chrna2-Cre animals and double transgenic Chrna2-Cre::APP/PS1 mice. For this purpose, bilateral injections were administered to the vHPC under stereotactic conditions. The animals in the treatment group received bilateral injections of the viral vector

AAV2.hSyn.DIO.hM3D(Gq).mCherry into the vHPC, enabling an expression of the activating DREADD receptor (hM3D(Gq)).

The control group (WT and APP/PS1) received equal injections of a loxP-flanked control virus (AAV.hSyn.DIO.mCherry) without functional DREADD. Before each experimental test mice also received C21 injections as the treated groups (Chrna2-Cre and Chrna2-Cre::APP/PS1) to prevent the possibility that the DREADD agonist itself causes behavior-altering effects. This allowed to verify whether potential behavioral differences were actually due to manipulation of the vHPC and not caused by the effects of C21 or the virus injection.

The present results of the cFC show a prominent phase-dependent influence of ventral hippocampal O-LMα2 interneurons on contextual fear conditioning, especially in the context of Alzheimer's disease. During acquisition (day 1), wild-type and APP/PS1 control animals that did not receive chemogenetic manipulations showed expected behavioral profiles in the control groups. Here, wild-type mice showed a freezing behavior of approximately 60%, while APP/PS1 controls showed reduced freezing, which is consistent with impaired contextual memory formation in this model.

Chrna2-Cre mice which received the hM3Dq activation of O-LMα2 interneurons performed at the level of wild-type controls, indicating that increased distal inhibition might be effectively buffered by intact hippocampal circuits. In contrast, Chrna2::APP/PS1 mice under the same manipulation showed a profound deficit, with freezing responses under 20%.

This finding suggests that in the APP/PS1 hippocampus, which shows AD-like pathology, additional O-LM-induced inhibition may critically disrupt the integration of entorhinal inputs in CA1 pyramidal cells, thereby preventing the formation of robust contextual memory traces. Here, the absence of encoding deficits in Chrna2-Cre mice does not seem to be in conflict with the optogenetic findings of (Mikulovic et al. 2018), who demonstrated that activation of O-LMα2 impairs object memory even in healthy animals.

This discrepancy can be addressed by considering task-specific network requirements. Object memory relies strongly on entorhinal inputs to distal CA1 dendrites, making it highly susceptible to O-LM-mediated suppression.

In contrast, contextual fear conditioning relies more strongly on Schaffer collateral inputs from CA3, which can compensate for a reduction in entorhinal drive.

Such compensatory mechanisms are preserved in WT networks but are significantly impaired in APP/PS1 mice. While O-LM activation has little effect in healthy Chrna2-Cre mice, it exposes existing deficits in the Alzheimer's-like hippocampus and leads to an almost complete lack of encoding. Consistent with this, a normalization of freezing responses across all groups

was observed in the retrieval data. On the second day, WT, APP/PS1, and Chrna2-Cre mice all showed a freezing response of about 60%, while Chrna2::APP/PS1 mice − despite their major encoding deficit − recovered to about 50%.

This might suggest that O-LM activation, which is harmful during the encoding phase, might be beneficial during retrieval by maintaining buffering pathological hyperexcitability in APP/PS1 circuits.

Taken together, the results suggest a lack of detectability of a consistent effect under the given boundary conditions rather than the certain absence of a biological effect.

A central and important aspect limiting the present experiments is that the manipulations were performed during both the encoding and retrieval phases. This approach makes it difficult to clearly relate the observed effects to a specific memory phase. From a neurophysiological perspective, changes during encoding may already have influenced the quality of the initial memory trace, making it impossible to detect a separate effect during retrieval.

For example, if manipulation had been applied only during encoding, later differences in behavior could most likely be linked to the encoding phase (Ranganath 2010; Squire und Wixted 2011). In contrast, if manipulation had taken place only during retrieval, this would have provided evidence for the involvement of the studied cell types in memory recall. Since in this study both encoding and retrieval phases were affected equally, it is not possible to tell which phase was contributing for the effects.

This is a methodological limitation, which is well known in literature. As described encoding and retrieval depend on some equal neural mechanism, but not identical (Diana et al. 2007; Eichenbaum 2017). While encoding is closely linked to the integration of sensory inputs and initial synaptic plasticity (Morris 2006), retrieval mainly depends on the reactivation of hippocampal and prefrontal networks, which are modulated depending on context (Preston und Eichenbaum 2013; Fernández und Morris 2018).

For future experiments, phase-specific manipulations will therefore be crucial to examine the distinct roles of encoding and retrieval. A specific manipulation only during encoding could reveal the importance of the studied interneurons for memory formation, whereas manipulation restricted to retrieval would test their contribution to recall.

Another methodological consideration in this study is the choice of pharmacological ligands for activating the DREADDs. In the first two experimental groups with wild-type and SST mice, CNO was used, while in a later group with Chrna2-Cre mice, C21 was used instead. So, within the same behavioral paradigms different ligands were used to activate the DREADDs. This makes it difficult to compare the experiments later, the decision to use C21 was

scientifically justified and supported in the literature. CNO has long been the standard ligand in chemogenetic studies, but it is pharmacologically critical.

A major criticism focuses on its reverse metabolism to clozapine, which has a broad binding spectrum to endogenous G protein-coupled receptors (GPCRs). These off-target effects can influence behavior, neuronal activity, and even basic physiological parameters such as sleep architecture, regardless of DREADD expression. Those effects are seen in animals which did not receive DREADDs and are therefore clearly not specific, but caused by clozapine-dependent off-targets. In behavioral experiments, too, it is discussed that these non-specific effects may complicate interpretation and can prevent correlation of effects to DREADD activations.

In this context, C21 gained importance as a better alternative. Compared to CNO, C21 has several advantages: it has higher potency at muscarinic DREADDs (e.g., hM3Dq, hM4Di), which means it reaches lower EC50 values and shows robust bioavailability and brain penetration (Thompson et al. 2018). Unlike CNO, C21 is not metabolized back to clozapine, reducing the risk of clozapine-induced off-target effects. (Robinson et al. 2023) also demonstrated that C21 has significantly higher selectivity for DREADDs compared to endogenous receptors and can therefore be seen as a more reliable and specific ligand. (Ferrari et al. 2022) confirmed this in neurophysiological studies and found that C21 produces consistent EEG and neural activity profiles comparable to CNO, but with a lower risk of clozapine-related artifacts.

In the present study, this means that the results generated in the first two experimental groups using CNO may be influenced by clozapine-related off-targets and therefore limited in their specificity. The use of C21 in the third experiment was a logical step in this sense, because it overcame one of the known limitations of CNO.

However, although the use of two different ligands within a project with similar paradigms used, leads to methodological heterogeneity, the switch to C21 increases the validity of the manipulations and the outcome.

In summary, it can be concluded that the use of C21 in the later stages of the work was not only methodologically but also scientifically justified.

For future investigations, it therefore seems reasonable to continue with a consistent ligand strategy, with C21 agonists being preferred. In addition, larger control groups should be used to quantify possible off-target effects and further increase the significance of chemogenetic experiments.

4.2. Functional mapping of mPFC neural activity during reward-based learning using two-photon microscopy

The present results should be considered in the context of existing literature on the role of the mPFC and its interaction with the hippocampus in spatial memory processes. While the hippocampus has been seen as the main structure for encoding and consolidating spatial and contextual info (SCOVILLE und MILNER 1957; O'Keefe und Nadel 1978), the mPFC plays a complementary and integrative role (Eichenbaum 2017; Euston et al. 2012). The mPFC plays a key role in coordinating spatial working memory by translating representations provided by the hippocampus into task-specific decision-making and action processes (Miller und Cohen 2001; Spellman et al. 2015a). Functionally, several studies show that interactions between the hippocampus and the mPFC, mediated by theta and gamma oscillations, play a key role in the temporally precise communication between the two structures (Sigurdsson et al. 2010; Jones und Wilson 2005b; Colgin 2011). This synchronization allows memory content from the hippocampus to be integrated into prefrontal networks and made available for goal-directed behavior. Impairments in these interactions, as described in the mouse model for Alzheimer's disease (APP/PS1) or in clinical patient cohorts, often lead to deficits in spatial working memory and impair flexibility in adapting to new spatial or contextual information (Hyman et al. 2010; Mably und Colgin 2018; Kesner und Churchwell 2011).

In this context, the establishment of mPFC prism-window imaging during a spatial learning paradigm on the linear treadmill offers an important approach to directly investigate the dynamics of large neuronal populations during cognitive tasks.

This approach enables to investigate not only the extent to which APP/PS1 mice can still form position-specific memory content in advanced age, but also how prefrontal (ensemble) activity is organized in interaction with hippocampal networks in wild-type mice and under AD-like conditions.

Therefore, a pioneering approach was established in the laboratory to record neural activity patterns in the mPFC of mice during behavioral paradigms with high cellular resolution using the two-photon microscope. This was achieved using a combined method of viral expression of the calcium indicator GCaMP6f and implanted microscope prisms, which were made accessible through a chronic mPFC imaging window.

The successful establishment of this surgically and technically challenging method was demonstrated by pilot data: the implantation of the prism was stable, the expression of GCaMP6f was shown to be robust, and the animals could be reliably imaged in a head-fixed

state using a two-photon microscope. These results demonstrate the viability of the approach and provide an important methodological basis for further experiments.

Such data should be understood as preliminary data or proof-of-concept experiments, as they document the successful implementation of a complex in vivo method. Based on this methodological approach, initial behavioral paradigms were implemented to investigate the function of the mPFC during cognitive tasks in the Alzheimer's model, which is currently poorly understood.

For this purpose, a linear treadmill task with defined and tactile zones (including a reward zone) was established, which requires learning and remembering position-specific information. Simultaneous recording of Ca^{2+} transients from several hundred neurons was combined with parameters such as running speed, position data, and reward-associated behaviors.

The first analysis showed that 15-month-old transgenic APP/PS1 mice were able to identify the reward zone and consolidate this behavior over several test/habituation and trial runs.

The establishment of prism imaging in the mPFC during behavior represents a methodological innovation that makes it possible to capture the dynamics of large neuron populations in an area central to executive functions. At the same time, these pilot findings from one animal allow hypotheses to be derived for further analysis. The available data provides the basis for further investigation.

A central issue concerns the dynamic organization of neural ensembles in the mPFC. Such limitations in the variability of neural activity patterns could indicate deficits in the adaptability of prefrontal networks and would be consistent with reports of reduced cognitive flexibility in mouse models of AD. Furthermore, the investigation of functional network interactions is of central importance. Since the mPFC is in close reciprocal connection with the hippocampus, electrophysiological methods such as LFP recordings and spike phaselocking could be used to characterize functionally those direct LRIPs and temporal synchronization mechanisms between the two structures.

This would clarify how information transmission in the hippocampus-prefrontal cortex network is specifically impaired in APP/PS1 mice or whether compensatory adaptations can be observed by using chemogenetic or optogenetic tools.

4.3. Limitations & Outlook

This study combined three highly complementary strategies to manipulate hippocampal circuits: global inhibition in wild-type mice, selective inhibition of SST^{+} interneurons in SST-Cre animals, and activation of $Chrna2^{+}$ O-LM interneurons. Using a variety of classic

behavioral tasks such as OF, NOR, Y-maze, and cFC, the experiments reveal both the utility and limitations of chemogenetic approaches and provide several important methodological insights.

4.3.1. Choice of DREADD ligands

An important aspect is the use of different ligands. CNO was used in the first two groups (global inhibition of WT mice and SST^+ inhibition in SST-Cre mice), while C21 was preferred in the third group (O-LM activation in Chrna2-Cre mice). It is known that CNO is converted back to clozapine *in vivo*, which can lead to off-target effects and complicate interpretation (Roth 2016; Robinson et al. 2023). C21, in contrast, has higher selectivity for muscarinic DREADDs and is not re-converted, making it more specific (Thompson et al. 2018). At the same time, the use of two different ligands within the same behavioral paradigms makes it difficult to compare the groups. It is unclear to what level the pharmacology of the ligands may have influenced the results. For future experiments, it would therefore be preferable to pursue a consistent ligand strategy.

4.3.2. Specificity of mouse lines

Another methodological point concerns the mouse lines. The SST-Cre line was useful as a first step, but it is not completely specific. It shows unwanted expression in CA3 pyramidal neurons and in parts of the ventral CA1, which can lead to bias in inhibitory manipulations (Müller-Komorowska et al. 2020; Mikulovic et al. 2015; Mikulovic et al. 2018). Incorporating the Chrna2-Cre line was a crucial step, as this line allows selective targeting of O-LM interneurons (Leão et al. 2012; Thulin et al. 2025). These cells play an important role by controlling the balance of entorhinal and hippocampal inputs to CA1 pyramidal neurons and acting as gatekeepers for memory processes through cholinergic mechanisms.

4.3.3. Interpretation of results and study design

The behavioral effects observed were not strong, but trends observed across different tasks suggest that O-LM interneurons may play a role that could only be revealed with larger animal groups and designs that clearly separate between memory encoding and memory retrieval. Previous studies indicate that O-LM interneurons operate in a phase-dependent manner and that differences along the dorsoventral axis of the hippocampus may influence how these circuits function.

4.3.4. Chemogenetics versus optogenetics

Chemogenetic tools are useful because they enable long-lasting and reliable stimulation. But they lack temporal and spatial precision and always need ligands to be given systemically, which can cause unwanted side effects. Optogenetics overcomes these problems by allowing millisecond-precise and location-specific control (Deisseroth 2015).This makes it possible to test encoding and retrieval periods within the same animal and to focus on selected subregions such as CA1 or the mPFC. Another advantage is that optogenetics can also be combined with freely moving behavior, e.g., OF, NOR, Y-maze, or cFC, and with imaging techniques such as two-photon calcium recording and LFP techniques. This enables the direct correlation of behavior with neural activity and allows for a deeper understanding of the role of projections between the hippocampus and prefrontal cortex.

4.3.5. Sample size

The total number of animals in this study was small. This reduced the statistical power and made it difficult to detect hypothesized effects. Future experiments should include more animals to allow for robust conclusions. This would help increase reliability while keeping the number of animals at a reasonable level, which is required for behavioral experiments anyway.

4.3.6. Male and female differences

In this study, both male and female mice were included, but the group sizes were too small to examine sex-specific differences in detail. The literature shows mixed results. Some studies report that males perform better in spatial tasks such as the water maze (Choleris et al. 2018; Jonasson 2005). However, other studies do not show clear differences or even reveal that females perform better than males under certain conditions (Beery und Zucker 2011). Factors such as stress levels, type of task, and age appear to strongly influence the results (Shansky 2018). Future studies must include balanced groups so that sex can be included as an important factor in the analysis.

4.3.7. Outlook

Taken together, three points stand out for future work. First, consistent use of specific mouse lines such as Chrna2-Cre is important to target O-LM interneurons. Second, modern and selective tools should be applied in a consistent way, and optogenetics should be established as a standard method to reach temporal and spatial precision. Third, combining these

manipulations with freely moving behavior and neural recordings will allow a much better understanding of how hippocampus and prefrontal cortex interact in healthy animals and in disease models such as APP/PS1. Furthermore, future studies will require larger samples and experimental groups in which encoding and retrieval are tested independently. This means that in one group, only the encoding phase is manipulated, while in another independent group, encoding remains unchanged and only the retrieval phase is stimulated before the animal performs the task.

5. Appendix

5.1. Abbreviations

AAV	Adeno-associated virus
Aß	Amyloid beta
Ach	Acetylcholine
ACC	Anterior cingulate cortex
AD	Alzheimer's disease
AICD	Amyloid precursor intracellular domain
AMPA	α-amino-3-hydroxy-5-methyl-4-isoxazolepropionic acid
AP	Antero-posterior
ApoE	Apolipoprotein E
APP	Amyloid precursor protein
ASC	apoptosis-associated speck-like protein containing
BC	basket cells
BIC	bistratified cells
BSA	Bovine serum albumin
Ca^{2+}	Calcium
CA	Cornu ammonis
CARD	caspase recruitment domain
CCK	Cholecystokinin
Ca^{2+}	Calcium
CaImAn	Calcium Imaging Analysis
CamKII	Calcium/calmodulin-dependent protein kinase II
cAMP	cyclic adenosine monophosphate
Chrna2	Cholinergic Receptor Nicotinic Alpha 2 Subunit
CNMF	Constrained Non-negative Matrix Factorization
CNN	Convolutional neural network
CNO	Clozapine N-oxide
C21	Compound 21
DAG	Diacylglycerol
DAPI	4′,6-diamidino-2-phenylindole
DBS	Deep brain stimulation
DG	Dentate Gyrus
∆F/F	Delta F over F
DG	Dentate gyrus
DLC	DeepLabCut
DMSO	Dimethyl sulfoxide
DV	Dorso-ventral
EPSP	Excitatory post synaptic potential
FAD	Familial Alzheimer's Disease
IL	Infralimbic area
IL-1ß	Interleukin-1ß
i.p.	Intraperitoneal
IS-3	interneuron-specific type 3 cells
GABA	Gamma amino butyric acid
GDP	Guanosine diphosphate
GECI	Genetically encoded calcium indicator
GIRK	G-protein–gated Inwardly Rectifying Potassium Channe

GTP	Guanosine triphosphate
gSig	spatial scale of the signal
HPC	Hippocampus
IEG	Immediate early gene
IP_3	Inositol-1,4,5-trisphosphate
IPSP	Inhibitory post synaptic potential
LFP	Local field potential
LRIP	Long-range inhibitory projection
LP	Long pass dichroic mirror
LTD	Long term depression
LTP	Long term potentiation
mAChRs	Muscarinic acetylcholine receptors
MCI	Mild cognitive impairment
MeX04	Methoxy-X04 (4,4'-[(2-methoxy-1,4-phenylene)di-(1E)-2,1-ethenediyl]bis-phenol)
MI	Modulation index
ML	Medio-lateral
mPFC	Medial prefrontal cortex
MS	medial septum
mTORC1	mechanistic Target of Rapamycin Complex 1
NA	Numeric aperture
nAChR	Neuronal nicotinic acetylcholine receptor
NFTs	Neurofibrillary tangles
NGC	neurogliaform cells
NI	nucleus incertus
NLRP3	NACHT, LRR, and PYD domains-containing protein 3
NMDA	N-Methyl-D-Aspartate
NoRMCorre	Non-Rigid Motion Correction
n.s.	Not significant
NOR	Novel object recognition
O-LM	Oriens-lacunosum moleculare
PBS	Phosphate buffer saline
PFA	Paraformaldehyde
PMT	Photomultiplier
PKC	Protein kinase C
PL	Prelimbic are
PLC	Phospholipase C
PN	Pyramidal neurons/ cells
PP	Perforant pathway
PrnP	prion protein promoter
PROTAC	proteolysis targeting chimera
PSEN 1	Presenilin 1
PSEN 2	Presenilin 2
PV	Parvalbumin
RAD	radiatum-directed cells
ROI	Region of interest
rpm	Rounds per minute
RT	Room temperature
s.c.	Subcutaneously
Sch	Schaffer collaterals
SLM	*Stratum lacunosum moleculare*

SNR	*Signal-to-noise ratio*
SO	*Stratum oriens*
SP	*Stratum pyramidale*
SR	*Stratum radiatum*
SST	Somatostatin
TAP	Temporoammonic pathway
TTL	Pulses for triggering/synchronization
vHPC	Ventral hippocampus
VIP	Vasoactive intestinal peptide
WT	Wild-type

5.2. Consumables

5.2.1. Surgery

Designation	Product no.	Company
Sugi Saugtupfer mit Griff 70 x 7mm steril	30601	QUESTALPHA GmbH & Co. KG (Eschenburg, Germany)
SMI Spon Gelatineschwamm Standard 80x50x10 mm	603322	Praxisdienst GmbH (Longuich, Germany)
X10 EINWEG SKALPELL NR.15 STERIL	11728353	Fisher Scientific (Schwerte, Germany)
HANDSCHUH SEMPERGUARD COMFORT NITR. PF M	SEMP816781635	VWR (Radnor, Pennsylvania, Vereinigte Staaten)
Tc Plate 24 Well Standard, F	83.3922.005	Sarstedt (Nümbrecht, Germany)
VICRYL VIOL GEFL - 6-0; TF; 0,70 (VE 36) - Ethicon	V929H	Johnson & Johnson (New Jersey, USA)
Cotton Swab steril einzeln verpackt	115-8271	VWR (Radnor, Pennsylvania, Vereinigte Staaten)
Einmal-Kanülen Sterican® stumpf, 27G, 0,4 x 25 mm	11668296	Th. Geyer (Renningen, Germany)
Prism RA H-K9L 1.5 x 1.5 x 1mm Coated Hyp as per 4530-0406	4530-0406	Tower Optical (Norwalk, Connecticut, USA)
Sterilisationsbeutel Steriking®, selbstklebend, 90 x 250 mm, 200 Stück	KKY0.1	Carl Roth GmbH + Co. KG (Karlsruhe, Germany)
Nanofil Syringe 10µl	NANOFIL	World Precision Instruments (Sarasota, FL, USA)
GC Gradia Direct Flo BW, 2 Spritzen à 1,5 g	45922	GC Cooperation (Tokyo, Japan)
Kontakt Chemie DRUCKLUFT 67 33170-DE Druckluftspray nicht brennbar 100 ml	829771-BP	Conrad Electronic (Hirschau, Germany)
OptiBond™ FL Kit Kerr, REF 26684E	34938	Dentalheld (Düsseldorf, Germany)
HS-Maxima® Papierspitzen ISO 035, grün, Packung 200 Stück	9001217	Henry Schein (Melville, New York, USA)
Fast Curing Optical Adhesive 1 oz.	NOA81	Norland Products Inc. (Cranbury, NJ, USA

5.3. Reagents

5.3.1. AAVs

Designation	Titer	Product no.	Company
AAV1-CAG-FLEX-tdTomato,	100 µL at titer ≥ 1×10^{13} vg/mL	43-131918	UNC Vector core (Chapel Hill, North Carolina, USA)
AAV1-CAG-tdTomato	100 µL at titer ≥ 5×10^{12} vg/mL	-	Addgene (Watertown, USA)
AAV2-hSyn-hM3D(Gq)-mCherry	100 µL at titer ≥6×10^{12} vg/mL	50474-AAV2	Addgene (Watertown, USA)
AAV2-hSyn-hM4D(Gi)-mCherry	100 µL at titer ≥ 5×10^{12} vg/mL	50475-AAV2	Addgene (Watertown, USA)
pAAV-hSyn-DIO-mCherry	100 µL at titer ≥ 4×10^{12} vg/mL	50459-AAV2	Addgene (Watertown, USA)
Retrograde AAV (pAAV-hSyn-DIO-EGFP)	100 µL at titer ≥ 7×10^{12} vg/mL	50457-AAVrg	Addgene (Watertown, USA)
AAV1.CamKII.GCaMP6f.WPRE.SV40	100 µL at titer ≥ 1×10^{13} vg/mL	100834-AAV1	Addgene (Watertown, USA)

5.3.2. Antibodies

Designation	Dilution	#LOT	Product no.	Company
Chicken anti-cfos	1:250	1-3	22609	Synaptic Systems (Göttingen, Germany)
Rabbit anti-Somatostatin	1:250		SAB4502861-100UG	Sigma-Aldrich (St. Louis, Missouri, USA)
Rat anti-mCherry	1:10000	YH374753	M11217	Thermo Scientific (Massachusetts, USA)
DAPI (10 mg)	1:5000	0000116964	D9542-10MG	Sigma-Aldrich (St. Louis, Missouri, USA)
Goat anti-rat IgG, Alexa Fluor® 594	1:400	2026149	A11007	Invitrogen Thermo Fisher Scientific (Massachusetts, USA)
Goat anti-chicken IgY, Alexa Fluor® 488	1:400	2566343	A-11039	Life Technologies (Carlsbad, Kalifornien, USA)
Goat anti-rabbit IgG, Alexa Fluor® 647	1:400	2390713	A21244	Invitrogen Thermo Fisher Scientific (Massachusetts, USA)

5.3.3. Anesthetics and Medications

Designation	Product no.	Company
Tramadol AbZ 100 mg/ml Tropfen	PZN 01017178	AbZ-Pharma GmbH (Ulm, Germany)
Ketavet® (Ketaminhydrochlorid) 100 mg/ml	D3821-07	Pfizer (New York, USA)
Rompun® (Xylazinhydrochloride) 2%	KP09X0L	Bayer (Leverkusen, Germany)

5.3.4. Pharmaceutical Manipulation

Designation	Product no.	Company
CNO (Clozapine *N*-Oxide)	C0832	Sigma-Aldrich (St. Louis, USA)
DREADD agonist 21 (Compound 21)	HB4888	Hello Bio (Bristol, United Kingdom)

5.3.5. Immunohistochemistry

Designation	Product no.	Company
10% normal goat serum	50062Z	Life technologies (Carlsbad, USA)
Fluorescence mounting medium	S3023	Dako/Agilent Technologies (Santa Clara, USA)
Triton-X100	A1388	Sigma-Aldrich (St. Louis, USA)
Bovine serum albumine	0163	Roth (Karlsruhe, Germany)
Phosphate buffered saline (PBS)	A0964	AppliChem (Darmstadt, Germany)
Paraformaldehyde (PFA) 10%	A146.1	Roth (Karlsruhe, Germany)
Dako fluorescent mounting medium	S3023	Dako Denmark (Glostrup, Denmark)
Coverslips	H878.2	Carl Roth GmbH + Co. KG (Karlsruhe, Germany)
Parafilm M, Rolle 100 mm x 38 m, Packung à 1 Stück	743311	BIOZYM SCIENTIFIC (Hessisch Oldendorf, Germany)
Glass slides	H870.1	Carl Roth GmbH + Co. KG (Karlsruhe, Germany)

5.3.6. Solution

Anesthetic solution	Volume [ml]	MeX04 solution	Volume	CNO/C21 [0.4 µg/ µl]	Volume
Ketamine 10%	1 ml	DMSO	1000 µl	DMSO 1%	0.125 ml
Xylazine 2%	0.25 ml	NaCl 0.9% (pH 12)	1000 µl	NaCl 0.9	12.375 ml
NaCl 0.9	6 ml	MeX04	10 mg	CNO/C21	5 mg

5.4. Equipment

5.4.1. Surgery

Designation	Product no.	Company
Micro4 Micro Syringe Pump Controller	SYS-MICRO4	World Precision Instruments (Sarasota, USA)
UMP3 Ultra Micro Pump	UMP3	World Precision Instruments (Sarasota, USA)
NanoFil Syringe 10 µL	NANOFIL	World Precision Instruments (Sarasota, USA)
Remote Control SM-7	200-100 900 9050	Luigs and Neumann (Ratingen, Germany)
Control system SM7	200-100 900 7411	Luigs and Neumann (Ratingen, Germany)
LN Junior RE/LE (3 axes)	210-1000000070-RE/LE	Luigs and Neumann (Ratingen, Germany)
Dentaldrill	A755983	Schick (Schemmerhofen, Germany)
Stereomicroscope SZ 51	19320	Olympus (Tokyo, Japan)
Sterilizer, Steri 250	031100	Keller (Burgdorf, Switzerland)
Pipette holder	UPN-1	Narishige (Tokyo, Japan)
Pipette holder	UPN-2	Narishige (Tokyo, Japan)
Peri-Star Pro, peristaltic pump	PERIPRO-4LS	World Precision Instruments (Sarasota, USA)
Light-curing device, LED smart (420nm-480nm, 1000 W/cm^2)	14012119	Kohlschein-Dental GmbH & Co. KG (Altenberge, Germany)
Surgical tools	various	Fine Science Tools (Foster City, CA USA)

Stereotactic base plate for mice	SR-A	Narishige (Tokyo, Japan)
Auxiliary ear bars for mice	EB-3B	Narishige (Tokyo, Japan)
Auxiliary ear bars for mice	EB-5N	Narishige (Tokyo, Japan)
Head holding device for mice	MA-6N	Narishige (Tokyo, Japan)
UV-Diode LEDMOD V2 365nm	LEDMOD365 .450.V2	OMICRON electronics GmbH (Rodgau, Germany)

5.4.2. Behavior

Designation	**Product no.**	**Company**
Box (50x 50x 50 cm)	-	Custom built (DZNE, Bonn, Germany)
Fear conditioning box	-	Custom built (DZNE, Bonn, Germany)
Y-maze	-	Custom built (DZNE, Bonn, Germany)
Camera UI-3140CP-C-HQ Rev.2	UI-3140CP-C-HQ Rev.2	IDS Imaging Development Systems GmbH (Obersulm, Heilbronn, Germany)
VOLTCRAFT LX-10 Luxmeter 0 - 199900 lx	1662853-BP	Conrad Electronic SE (Hirschau, Bayern, Germany)
Arduino Board	-	Arduino LLC/Arduino Srl (Ivrea, Italy & USA)
RAZER Ring Light LED Ringleuchte Anzahl LEDs=192	15702759	Galaxus Deutschland GmbH (Hamburg, Germany)
Rollenpflaster Leukosilk®	0631.1	Carl Roth GmbH + Co. KG (Karlsruhe, Germany)
Laufbandstoff, L: 19m, B: 65mm, 11g/m	700-100 900 0201	Luigs und Neumann (Ratingen, Germany)

5.4.3. Microscopes

Designation	**Company**
Zeiss LSM 900	Carl Zeiss Microscopy GmbH (Jena, Germany)
Zeiss LSM 880	Carl Zeiss Microscopy GmbH (Jena, Germany)
Bergamo II	Thorlabs Inc. (Newton, NJ, USA)
Zeiss AxioScan	Carl Zeiss Microscopy GmbH (Jena, Germany)

Zeiss AxioZoom	Carl Zeiss Microscopy GmbH (Jena, Germany)

5.4.4. Software

Designation	**Company**
Adobe Illustrator, Version 28.4.1	Adobe Systems Inc. (Mountain View, CA USA)
GraphPad Prism 9	GraphPad Software, Inc. (San Diego, CA USA)
Fiji/ImageJ 152.i	Wayne Rasband (NIH, USA)
Bonsai	Open-source framework, developed by Gonçalo Lopes (Portugal)
ZEN	Carl Zeiss AG (Jena, Germany)
Omicron Control Center (v3.9.28)	OMICRON electronics GmbH (Klaus, Austria)
EthoVision XT17	Noldus (Wahningen, Netherlands)
Thorlabs	Thorlabs GmbH (Newton, NJ, USA)
DeepLabCut	developed by the Mathis Lab at EPFL and open-source contributors
IDS peak Cockpit 1.5.0.0	IDS Imaging Development Systems GmbH (Obersulm, Heilbronn, Germany)
Emi Converter	Custom GUI-based converter
Tracking plotter	Custom GUI-based plotter

5.5. Contributions

In this study, Falko Fuhrmann contributed his help to establish the mPFC cranial prism window surgeries, providing technical advice, helping out to preparing the treadmill experiment, and partially performing the AAV cranial injections. Niko Britt partially assisted in conducting the behavioral experiments and finished the confocal imaging. The intraperitoneal injections during the behavior experiments were carried out by Arush Baijal, Shuvrangshu Guha, Eileen Tedt, Dilek Mercan Saglam, and Andrea Baral. Additionally, Andrea Baral took care of genotyping and provided help with the perfusions after the experiments. With Julia Steffen, she also performed the immunohistochemistry.

6. References

Abbas, Atheir I.; Sundiang, Marina J. M.; Henoch, Britt; Morton, Mitchell P.; Bolkan, Scott S.; Park, Alan J. et al. (2018): Somatostatin Interneurons Facilitate Hippocampal-Prefrontal Synchrony and Prefrontal Spatial Encoding. In: *Neuron* 100 (4), 926-939.e3. DOI: 10.1016/j.neuron.2018.09.029.

Aisen, P. S.; Davis, K. L. (1994): Inflammatory mechanisms in Alzheimer's disease: implications for therapy. In: *The American journal of psychiatry* 151 (8), S. 1105–1113. DOI: 10.1176/ajp.151.8.1105.

Albadawi, Emad A. (2025): Structural and functional changes in the hippocampus induced by environmental exposures. In: *Neurosciences (Riyadh, Saudi Arabia)* 30 (1), S. 5–19. DOI: 10.17712/nsj.2025.1.20240052.

Alzheimer, Alois (1907a): Über eine eigenartige Erkrankung der Hirnrinde. In: *Allg Z Psychiatrie Psychisch-Gerichtl Med 64: 146–148*.

Alzheimer, Alois (1907b): Über eine eigenartige Erkrankung der Hirnrinde. In: *Zbl Nervenheilkd Psychiatr 30 (Neue Folge 18 bd)*.

Alzheimer, Alois (1906): Über einen eigenartigen, schweren Erkran kungsprozess der Hirnrinde. In: *Neurol Zbl 25: 1134*.

Amaral, D. G.; Witter, M. P. (1989): The three-dimensional organization of the hippocampal formation: A review of anatomical data. In: *Neuroscience* 31 (3), S. 571–591. DOI: 10.1016/0306-4522(89)90424-7.

Ameen, Taha Basit; Kashif, Syeda Naveera; Abbas, Syed Muhammad Iraj; Babar, Kulsoom; Ali, Syed Muhammad Sinaan; Raheem, Abdul (2024): Unraveling Alzheimer's: the promise of aducanumab, lecanemab, and donanemab. In: *The Egyptian Journal of Neurology, Psychiatry and Neurosurgery* 60 (1), S. 72. DOI: 10.1186/s41983-024-00845-5.

Armbruster, Blaine N.; Li, Xiang; Pausch, Mark H.; Herlitze, Stefan; Roth, Bryan L. (2007): Evolving the lock to fit the key to create a family of G protein-coupled receptors potently activated by an inert ligand. In: *Proceedings of the National Academy of Sciences of the United States of America* 104 (12), S. 5163–5168. DOI: 10.1073/pnas.0700293104.

Artinian, Julien; Jordan, Alexander; Khlaifia, Abdessattar; Honoré, Eve; La Fontaine, Alexandre; Racine, Anne-Sophie et al. (2019): Regulation of Hippocampal Memory by mTORC1 in Somatostatin Interneurons. In: *The Journal of neuroscience : the official journal of the Society for Neuroscience* 39 (43), S. 8439–8456. DOI: 10.1523/JNEUROSCI.0728-19.2019.

Asgarihafshejani, Azam; Honoré, Ève; Michon, François-Xavier; Laplante, Isabel; Lacaille, Jean-Claude (2022): Long-term potentiation at pyramidal cell to somatostatin interneuron synapses controls hippocampal network plasticity and memory. In: *iScience* 25 (5), S. 104259. DOI: 10.1016/j.isci.2022.104259.

Ashe, Karen H.; Zahs, Kathleen R. (2010): Probing the biology of Alzheimer's disease in mice. In: *Neuron* 66 (5), S. 631–645. DOI: 10.1016/j.neuron.2010.04.031.

Azarnia Tehran, Domenico; Kochlamazashvili, Gaga; Pampaloni, Niccolò P.; Sposini, Silvia; Shergill, Jasmeet Kaur; Lehmann, Martin et al. (2022): Selective endocytosis of Ca(2+)-permeable AMPARs by the Alzheimer's disease risk factor CALM bidirectionally controls synaptic plasticity. In: *Science advances* 8 (21), eabl5032. DOI: 10.1126/sciadv.abl5032.

Backus, Alexander R.; Schoffelen, Jan-Mathijs; Szebényi, Szabolcs; Hanslmayr, Simon; Doeller, Christian F. (2016): Hippocampal-Prefrontal Theta Oscillations Support Memory Integration. In: *Current biology : CB* 26 (4), S. 450–457. DOI: 10.1016/j.cub.2015.12.048.

Bannerman, D.M; Rawlins, J.N.P; McHugh, S.B; Deacon, R.M.J; Yee, B.K; Bast, T. et al. (2004): Regional dissociations within the hippocampus—memory and anxiety. In:

Neuroscience & Biobehavioral Reviews 28 (3), S. 273–283. DOI: 10.1016/j.neubiorev.2004.03.004.

Bannerman, David M.; Sprengel, Rolf; Sanderson, David J.; McHugh, Stephen B.; Rawlins, J. Nicholas P.; Monyer, Hannah; Seeburg, Peter H. (2014): Hippocampal synaptic plasticity, spatial memory and anxiety. In: *Nature reviews. Neuroscience* 15 (3), S. 181–192. DOI: 10.1038/nrn3677.

Baudry, Michel; Bi, Xiaoning (2024): Revisiting the calpain hypothesis of learning and memory 40 years later. In: *Frontiers in molecular neuroscience* 17, S. 1337850. DOI: 10.3389/fnmol.2024.1337850.

Beery, Annaliese K.; Zucker, Irving (2011): Sex bias in neuroscience and biomedical research. In: *Neuroscience & Biobehavioral Reviews* 35 (3), S. 565–572. DOI: 10.1016/j.neubiorev.2010.07.002.

Brazeau, P.; Vale, W.; Burgus, R.; Ling, N.; Butcher, M.; Rivier, J.; Guillemin, R. (1973): Hypothalamic polypeptide that inhibits the secretion of immunoreactive pituitary growth hormone. In: *Science (New York, N.Y.)* 179 (4068), S. 77–79. DOI: 10.1126/science.179.4068.77.

Bukke, Vidyasagar Naik; Archana, Moola; Villani, Rosanna; Romano, Antonino Davide; Wawrzyniak, Agata; Balawender, Krzysztof et al. (2020): The Dual Role of Glutamatergic Neurotransmission in Alzheimer's Disease: From Pathophysiology to Pharmacotherapy. In: *International journal of molecular sciences* 21 (20). DOI: 10.3390/ijms21207452.

Busche, Marc Aurel; Hyman, Bradley T. (2020): Synergy between amyloid-β and tau in Alzheimer's disease. In: *Nature neuroscience* 23 (10), S. 1183–1193. DOI: 10.1038/s41593-020-0687-6.

Bush, A. I.; Pettingell, W. H.; Multhaup, G.; d Paradis, M.; Vonsattel, J. P.; Gusella, J. F. et al. (1994): Rapid induction of Alzheimer A beta amyloid formation by zinc. In: *Science (New York, N.Y.)* 265 (5177), S. 1464–1467. DOI: 10.1126/science.8073293.

Bush, G.; Luu, P.; Posner, M. I. (2000): Cognitive and emotional influences in anterior cingulate cortex. In: *Trends in cognitive sciences* 4 (6), S. 215–222. DOI: 10.1016/s1364-6613(00)01483-2.

Buzsáki, György; Moser, Edvard I. (2013): Memory, navigation and theta rhythm in the hippocampal-entorhinal system. In: *Nature neuroscience* 16 (2), S. 130–138. DOI: 10.1038/nn.3304.

Buzsáki, György; Wang, Xiao-Jing (2012): Mechanisms of gamma oscillations. In: *Annual review of neuroscience* 35, S. 203–225. DOI: 10.1146/annurev-neuro-062111-150444.

Chandra, Sidhanth; Sisodia, Sangram S.; Vassar, Robert J. (2023): The gut microbiome in Alzheimer's disease: what we know and what remains to be explored. In: *Molecular neurodegeneration* 18 (1), S. 9. DOI: 10.1186/s13024-023-00595-7.

Chen, Chun; Liao, Jianming; Xia, Yiyuan; Liu, Xia; Jones, Rheinallt; Haran, John et al. (2022): Gut microbiota regulate Alzheimer's disease pathologies and cognitive disorders via PUFA-associated neuroinflammation. In: *Gut* 71 (11), S. 2233–2252. DOI: 10.1136/gutjnl-2021-326269.

Choleris, Elena; Galea, Liisa A.M.; Sohrabji, Farida; Frick, Karyn M. (2018): Sex differences in the brain: Implications for behavioral and biomedical research. In: *Neuroscience & Biobehavioral Reviews* 85, S. 126–145. DOI: 10.1016/j.neubiorev.2017.07.005.

Cipriani, Gabriele; Dolciotti, Cristina; Picchi, Lucia; Bonuccelli, Ubaldo (2011): Alzheimer and his disease: a brief history. In: *Neurological sciences : official journal of the Italian Neurological Society and of the Italian Society of Clinical Neurophysiology* 32 (2), S. 275–279. DOI: 10.1007/s10072-010-0454-7.

Colgin, Laura Lee (2011): Oscillations and hippocampal–prefrontal synchrony. In: *Current Opinion in Neurobiology* 21 (3), S. 467–474. DOI: 10.1016/j.conb.2011.04.006.

Colgin, Laura Lee (2016): Rhythms of the hippocampal network. In: *Nature reviews. Neuroscience* 17 (4), S. 239–249. DOI: 10.1038/nrn.2016.21.

Courtin, Julien; Chaudun, Fabrice; Rozeske, Robert R.; Karalis, Nikolaos; Gonzalez-Campo, Cecilia; Wurtz, Hélène et al. (2014): Prefrontal parvalbumin interneurons shape neuronal activity to drive fear expression. In: *Nature* 505 (7481), S. 92–96. DOI: 10.1038/nature12755.

Cunliffe, Grace; Tan, Li Yang; Jung, Sangyong; Turner, Jonathan; Gigg, John (2025): Executive dysfunction is associated with altered hippocampal-prefrontal functional connectivity in 3xTg Alzheimer's model mice. In: *Communications Biology* 8 (1), S. 1163. DOI: 10.1038/s42003-025-08546-2.

Dalton, Marshall A.; D'Souza, Arkiev; Lv, Jinglei; Calamante, Fernando (2022): New insights into anatomical connectivity along the anterior-posterior axis of the human hippocampus using in vivo quantitative fibre tracking. In: *eLife* 11. DOI: 10.7554/eLife.76143.

Dannenberg, Holger; Pabst, Milan; Braganza, Oliver; Schoch, Susanne; Niediek, Johannes; Bayraktar, Melike et al. (2015): Synergy of direct and indirect cholinergic septo-hippocampal pathways coordinates firing in hippocampal networks. In: *The Journal of neuroscience : the official journal of the Society for Neuroscience* 35 (22), S. 8394–8410. DOI: 10.1523/JNEUROSCI.4460-14.2015.

Deisseroth, Karl (2015): Optogenetics: 10 years of microbial opsins in neuroscience. In: *Nature neuroscience* 18 (9), S. 1213–1225. DOI: 10.1038/nn.4091.

Diana, Rachel A.; Yonelinas, Andrew P.; Ranganath, Charan (2007): Imaging recollection and familiarity in the medial temporal lobe: a three-component model. In: *Trends in cognitive sciences* 11 (9), S. 379–386. DOI: 10.1016/j.tics.2007.08.001.

Eichenbaum, Howard (2017): Prefrontal–hippocampal interactions in episodic memory. In: *Nature reviews. Neuroscience* 18 (9), S. 547–558. DOI: 10.1038/nrn.2017.74.

Euston, David R.; Gruber, Aaron J.; McNaughton, Bruce L. (2012): The role of medial prefrontal cortex in memory and decision making. In: *Neuron* 76 (6), S. 1057–1070. DOI: 10.1016/j.neuron.2012.12.002.

Fanselow, Michael S.; Dong, Hong-Wei (2010): Are the dorsal and ventral hippocampus functionally distinct structures? In: *Neuron* 65 (1), S. 7–19. DOI: 10.1016/j.neuron.2009.11.031.

Felix-Ortiz, A. C.; Burgos-Robles, A.; Bhagat, N. D.; Leppla, C. A.; Tye, K. M. (2016): Bidirectional modulation of anxiety-related and social behaviors by amygdala projections to the medial prefrontal cortex. In: *Neuroscience* 321, S. 197–209. DOI: 10.1016/j.neuroscience.2015.07.041.

Fernández, Guillén; Morris, Richard G.M. (2018): Memory, Novelty and Prior Knowledge. In: *Trends in neurosciences* 41 (10), S. 654–659. DOI: 10.1016/j.tins.2018.08.006.

Fernández-Arroyo, Beatriz; Jurado, Sandra; Lerma, Juan (2025): Understanding OLM interneurons: Characterization, circuitry, and significance in memory and navigation. In: *Neuroscience* 578, S. 69–80. DOI: 10.1016/j.neuroscience.2024.07.046.

Ferrari, Loris L.; Ogbeide-Latario, Oghomwen E.; Gompf, Heinrich S.; Anaclet, Christelle (2022): Validation of DREADD agonists and administration route in a murine model of sleep enhancement. In: *Journal of neuroscience methods* 380, S. 109679. DOI: 10.1016/j.jneumeth.2022.109679.

Francis, P. T.; Palmer, Alan; Snape, Mike; Wilcock, Gordon (1999): The cholinergic hypothesis of Alzheimer's disease: A review of progress. In: *Journal of neurology, neurosurgery, and psychiatry* 66, S. 137–147. DOI: 10.1136/jnnp.67.4.558.

Giovannucci, Andrea; Friedrich, Johannes; Gunn, Pat; Kalfon, Jérémie; Brown, Brandon L.; Koay, Sue Ann et al. (2019): CaImAn an open source tool for scalable calcium imaging data analysis. In: *eLife* 8, e38173. DOI: 10.7554/eLife.38173.

Goedert, M. (1993): Tau protein and the neurofibrillary pathology of Alzheimer's disease. In: *Trends in neurosciences* 16 (11), S. 460–465. DOI: 10.1016/0166-2236(93)90078-z.

Goodpaster, Caitlin M.; Christensen, Chloe R.; Alturki, Maryam-Batul; DeNardo, Laura A. (2025): Prefrontal cortex development and its implications in mental illness. In: *Neuropsychopharmacology : official publication of the American College of Neuropsychopharmacology*. DOI: 10.1038/s41386-025-02154-8.

Hampel, Harald; Hardy, John; Blennow, Kaj; Chen, Christopher; Perry, George; Kim, Seung Hyun et al. (2021): The Amyloid-β Pathway in Alzheimer's Disease. In: *Molecular Psychiatry* 26 (10), S. 5481–5503. DOI: 10.1038/s41380-021-01249-0.

Han, Lin; Yang, Dan; Kundra, Vikas (2007): Signaling can be uncoupled from imaging of the somatostatin receptor type 2. In: *Molecular imaging* 6 (6), S. 427–437.

Hangya, Balázs; Borhegyi, Zsolt; Szilágyi, Nóra; Freund, Tamás F.; Varga, Viktor (2009): GABAergic neurons of the medial septum lead the hippocampal network during theta activity. In: *The Journal of neuroscience : the official journal of the Society for Neuroscience* 29 (25), S. 8094–8102. DOI: 10.1523/JNEUROSCI.5665-08.2009.

Hardy, J.; Allsop, D. (1991): Amyloid deposition as the central event in the aetiology of Alzheimer's disease. In: *Trends in pharmacological sciences* 12 (10), S. 383–388. DOI: 10.1016/0165-6147(91)90609-v.

Heneka, Michael T. (2017): Inflammasome activation and innate immunity in Alzheimer's disease. In: *Brain Pathol* 27 (2), S. 220–222. DOI: 10.1111/bpa.12483.

Heneka, Michael T.; Kummer, Markus P.; Stutz, Andrea; Delekate, Andrea; Schwartz, Stephanie; Vieira-Saecker, Ana et al. (2013): NLRP3 is activated in Alzheimer's disease and contributes to pathology in APP/PS1 mice. In: *Nature* 493 (7434), S. 674–678. DOI: 10.1038/nature11729.

Heppner, Frank L.; Ransohoff, Richard M.; Becher, Burkhard (2015): Immune attack: the role of inflammation in Alzheimer disease. In: *Nature reviews. Neuroscience* 16 (6), S. 358–372. DOI: 10.1038/nrn3880.

Hoover, Walter B.; Vertes, Robert P. (2007): Anatomical analysis of afferent projections to the medial prefrontal cortex in the rat. In: *Brain structure & function* 212 (2), S. 149–179. DOI: 10.1007/s00429-007-0150-4.

Hyman, James M.; Zilli, Eric A.; Paley, Amanda M.; Hasselmo, Michael E. (2010): Working Memory Performance Correlates with Prefrontal-Hippocampal Theta Interactions but not with Prefrontal Neuron Firing Rates. In: *Frontiers in integrative neuroscience* 4, S. 2. DOI: 10.3389/neuro.07.002.2010.

Iqbal, Khalid; Liu, Fei; Gong, Cheng-Xin; Del Alonso, Alejandra C.; Grundke-Iqbal, Inge (2009): Mechanisms of tau-induced neurodegeneration. In: *Acta neuropathologica* 118 (1), S. 53–69. DOI: 10.1007/s00401-009-0486-3.

Jankowsky, Joanna L.; Slunt, Hilda H.; Gonzales, Victoria; Jenkins, Nancy A.; Copeland, Neal G.; Borchelt, David R. (2004): APP processing and amyloid deposition in mice haplo-insufficient for presenilin 1. In: *Neurobiology of aging* 25 (7), S. 885–892. DOI: 10.1016/j.neurobiolaging.2003.09.008.

Jankowsky, Joanna L.; Zheng, Hui (2017): Practical considerations for choosing a mouse model of Alzheimer's disease. In: *Molecular neurodegeneration* 12 (1), S. 89. DOI: 10.1186/s13024-017-0231-7.

Jay, T. M.; Witter, M. P. (1991): Distribution of hippocampal CA1 and subicular efferents in the prefrontal cortex of the rat studied by means of anterograde transport of Phaseolus vulgaris-leucoagglutinin. In: *The Journal of comparative neurology* 313 (4), S. 574–586. DOI: 10.1002/cne.903130404.

Jiao, Shu-Sheng; Bu, Xian-Le; Liu, Yu-Hui; Zhu, Chi; Wang, Qing-Hua; Shen, Lin-Lin et al. (2016): Sex Dimorphism Profile of Alzheimer's Disease-Type Pathologies in an APP/PS1

Mouse Model. In: *Neurotoxicity research* 29 (2), S. 256–266. DOI: 10.1007/s12640-015-9589-x.

Jonasson, Zachariah (2005): Meta-analysis of sex differences in rodent models of learning and memory: a review of behavioral and biological data. In: *Neuroscience & Biobehavioral Reviews* 28 (8), S. 811–825. DOI: 10.1016/j.neubiorev.2004.10.006.

Jones, Matthew W.; Wilson, Matthew A. (2005a): Theta rhythms coordinate hippocampal-prefrontal interactions in a spatial memory task. In: *PLoS biology* 3 (12), e402. DOI: 10.1371/journal.pbio.0030402.

Jones, Matthew W.; Wilson, Matthew A. (2005b): Theta rhythms coordinate hippocampal-prefrontal interactions in a spatial memory task. In: *PLoS biology* 3 (12), e402. DOI: 10.1371/journal.pbio.0030402.

Keller, J. N.; Schmitt, F. A.; Scheff, S. W.; Ding, Q.; Chen, Q.; Butterfield, D. A.; Markesbery, W. R. (2005): Evidence of increased oxidative damage in subjects with mild cognitive impairment. In: *Neurology* 64 (7), S. 1152–1156. DOI: 10.1212/01.WNL.0000156156.13641.BA.

Kesner, Raymond P.; Churchwell, John C. (2011): An analysis of rat prefrontal cortex in mediating executive function. In: *Neurobiology of Learning and Memory* 96 (3), S. 417–431. DOI: 10.1016/j.nlm.2011.07.002.

Khan, Ahsan; Ti, Chun Hang Eden; Yuan, Kai; Crespo Garcia, Maite; Anderson, Michael C.; Tong, Raymond Kai-Yu (2024): Medial Prefrontal Cortex Stimulation Reduces Retrieval-Induced Forgetting via Fronto-parietal Beta Desynchronization. In: *The Journal of neuroscience : the official journal of the Society for Neuroscience* 44 (37). DOI: 10.1523/JNEUROSCI.0189-24.2024.

Király, Bálint; Domonkos, Andor; Jelitai, Márta; Lopes-dos-Santos, Vítor; Martínez-Bellver, Sergio; Kocsis, Barnabás et al. (2023): The medial septum controls hippocampal supra-theta oscillations. In: *Nature Communications* 14 (1), S. 6159. DOI: 10.1038/s41467-023-41746-0.

Kjelstrup, Kirsten G.; Tuvnes, Frode A.; Steffenach, Hill-Aina; Murison, Robert; Moser, Edvard I.; Moser, May-Britt (2002): Reduced fear expression after lesions of the ventral hippocampus. In: *Proceedings of the National Academy of Sciences of the United States of America* 99 (16), S. 10825–10830. DOI: 10.1073/pnas.152112399.

Klausberger, Thomas; Magill, Peter J.; Márton, László F.; Roberts, J. David B.; Cobden, Philip M.; Buzsáki, György; Somogyi, Peter (2003): Brain-state- and cell-type-specific firing of hippocampal interneurons in vivo. In: *Nature* 421 (6925), S. 844–848. DOI: 10.1038/nature01374.

Klausberger, Thomas; Somogyi, Peter (2008): Neuronal diversity and temporal dynamics: the unity of hippocampal circuit operations. In: *Science (New York, N.Y.)* 321 (5885), S. 53–57. DOI: 10.1126/science.1149381.

L Lorenzini; A Maranzano; S Ingala; LE Collij; M Tranfa; K Blennow et al. (2024): Association of Vascular Risk Factors and Cerebrovascular Pathology With Alzheimer Disease Pathologic Changes in Individuals Without Dementia. In: *Neurology*. DOI: 10.1212/wnl.0000000000209801.

Laubach, Mark; Amarante, Linda M.; Swanson, Kyra; White, Samantha R. (2018): What, If Anything, Is Rodent Prefrontal Cortex? In: *eNeuro* 5 (5). DOI: 10.1523/ENEURO.0315-18.2018.

Leão, Richardson N.; Mikulovic, Sanja; Leão, Katarina E.; Munguba, Hermany; Gezelius, Henrik; Enjin, Anders et al. (2012): OLM interneurons differentially modulate CA3 and entorhinal inputs to hippocampal CA1 neurons. In: *Nature neuroscience* 15 (11), S. 1524–1530. DOI: 10.1038/nn.3235.

Leutgeb, Jill K.; Leutgeb, Stefan; Moser, May-Britt; Moser, Edvard I. (2007): Pattern separation in the dentate gyrus and CA3 of the hippocampus. In: *Science (New York, N.Y.)* 315 (5814), S. 961–966. DOI: 10.1126/science.1135801.

Liguz-Lecznar, Monika; Dobrzanski, Grzegorz; Kossut, Malgorzata (2022): Somatostatin and Somatostatin-Containing Interneurons-From Plasticity to Pathology. In: *Biomolecules* 12 (2). DOI: 10.3390/biom12020312.

Lovett-Barron, Matthew; Kaifosh, Patrick; Kheirbek, Mazen A.; Danielson, Nathan; Zaremba, Jeffrey D.; Reardon, Thomas R. et al. (2014): Dendritic Inhibition in the Hippocampus Supports Fear Learning. In: *Science (New York, N.Y.)* 343 (6173), S. 857–863. DOI: 10.1126/science.1247485.

Lu, Lihui; Ren, Yuqi; Yu, Tao; Liu, Zhixiang; Wang, Sice; Tan, Lubin et al. (2020): Control of locomotor speed, arousal, and hippocampal theta rhythms by the nucleus incertus. In: *Nature Communications* 11 (1), S. 262. DOI: 10.1038/s41467-019-14116-y.

Mably, Alexandra J.; Colgin, Laura Lee (2018): Gamma oscillations in cognitive disorders. In: *Current Opinion in Neurobiology* 52, S. 182–187. DOI: 10.1016/j.conb.2018.07.009.

Malenka, Robert C.; Bear, Mark F. (2004): LTP and LTD: An Embarrassment of Riches. In: *Neuron* 44 (1), S. 5–21. DOI: 10.1016/j.neuron.2004.09.012.

Mandelkow, E. M.; Mandelkow, E. (1998): Tau in Alzheimer's disease. In: *Trends in cell biology* 8 (11), S. 425–427. DOI: 10.1016/s0962-8924(98)01368-3.

Martinez-Losa, Magdalena; Tracy, Tara E.; Ma, Keran; Verret, Laure; Clemente-Perez, Alexandra; Khan, Abdullah S. et al. (2018): Nav1.1-Overexpressing Interneuron Transplants Restore Brain Rhythms and Cognition in a Mouse Model of Alzheimer's Disease. In: *Neuron* 98 (1), 75-89.e5. DOI: 10.1016/j.neuron.2018.02.029.

Mathis, Alexander; Mamidanna, Pranav; Cury, Kevin M.; Abe, Taiga; Murthy, Venkatesh N.; Mathis, Mackenzie Weygandt; Bethge, Matthias (2018): DeepLabCut: markerless pose estimation of user-defined body parts with deep learning. In: *Nature neuroscience* 21 (9), S. 1281–1289. DOI: 10.1038/s41593-018-0209-y.

Mikulovic, Sanja; Restrepo, C. Ernesto; Hilscher, Markus M.; Kullander, Klas; Leão, Richardson N. (2015): Novel markers for OLM interneurons in the hippocampus. In: *Frontiers in Cellular Neuroscience* Volume 9 - 2015. DOI: 10.3389/fncel.2015.00201.

Mikulovic, Sanja; Restrepo, Carlos Ernesto; Siwani, Samer; Bauer, Pavol; Pupe, Stefano; Tort, Adriano B. L. et al. (2018): Ventral hippocampal OLM cells control type 2 theta oscillations and response to predator odor. In: *Nature Communications* 9 (1), S. 3638. DOI: 10.1038/s41467-018-05907-w.

Miller, E. K.; Cohen, J. D. (2001): An integrative theory of prefrontal cortex function. In: *Annual review of neuroscience* 24, S. 167–202. DOI: 10.1146/annurev.neuro.24.1.167.

Möller, H. J.; Graeber, M. B. (1998): The case described by Alois Alzheimer in 1911. Historical and conceptual perspectives based on the clinical record and neurohistological sections. In: *European archives of psychiatry and clinical neuroscience* 248 (3), S. 111–122. DOI: 10.1007/s004060050027.

Morris, R. G. M. (2006): Elements of a neurobiological theory of hippocampal function: the role of synaptic plasticity, synaptic tagging and schemas. In: *European Journal of Neuroscience* 23 (11), S. 2829–2846. DOI: 10.1111/j.1460-9568.2006.04888.x.

Müller-Komorowska, Daniel; Opitz, Thoralf; Elzoheiry, Shehabeldin; Schweizer, Michaela; Ambrad Giovannetti, Eleonora; Beck, Heinz (2020): Nonspecific Expression in Limited Excitatory Cell Populations in Interneuron-Targeting Cre-driver Lines Can Have Large Functional Effects. In: *Frontiers in neural circuits* 14, S. 16. DOI: 10.3389/fncir.2020.00016.

Nath, Tanmay; Mathis, Alexander; Chen, An Chi; Patel, Amir; Bethge, Matthias; Mathis, Mackenzie Weygandt (2019): Using DeepLabCut for 3D markerless pose estimation

across species and behaviors. In: *Nature Protocols* 14 (7), S. 2152–2176. DOI: 10.1038/s41596-019-0176-0.

O'Keefe, John; Nadel, Lynn (1978): The Hippocampus as a Cognitive Map: Oxford: Clarendon Press. Online verfügbar unter http://hdl.handle.net/10150/620894.

Oddo, Salvatore; Caccamo, Antonella; Shepherd, Jason D.; Murphy, M. Paul; Golde, Todd E.; Kayed, Rakez et al. (2003): Triple-transgenic model of Alzheimer's disease with plaques and tangles: intracellular Abeta and synaptic dysfunction. In: *Neuron* 39 (3), S. 409–421. DOI: 10.1016/s0896-6273(03)00434-3.

Padilla-Coreano, Nancy; Bolkan, Scott S.; Pierce, Georgia M.; Blackman, Dakota R.; Hardin, William D.; Garcia-Garcia, Alvaro L. et al. (2016): Direct Ventral Hippocampal-Prefrontal Input Is Required for Anxiety-Related Neural Activity and Behavior. In: *Neuron* 89 (4), S. 857–866. DOI: 10.1016/j.neuron.2016.01.011.

Palop, Jorge J.; Mucke, Lennart (2010): Synaptic depression and aberrant excitatory network activity in Alzheimer's disease: two faces of the same coin? In: *Neuromolecular medicine* 12 (1), S. 48–55. DOI: 10.1007/s12017-009-8097-7.

Palop, Jorge J.; Mucke, Lennart (2016): Network abnormalities and interneuron dysfunction in Alzheimer disease. In: *Nature reviews. Neuroscience* 17 (12), S. 777–792. DOI: 10.1038/nrn.2016.141.

Pangalos, Maria; Donoso, José R.; Winterer, Jochen; Zivkovic, Aleksandar R.; Kempter, Richard; Maier, Nikolaus; Schmitz, Dietmar (2013): Recruitment of oriens-lacunosum-moleculare interneurons during hippocampal ripples. In: *Proceedings of the National Academy of Sciences* 110 (11), S. 4398–4403. DOI: 10.1073/pnas.1215496110.

Park, Pojeong; Volianskis, Arturas; Sanderson, Thomas M.; Bortolotto, Zuner A.; Jane, David E.; Zhuo, Min et al. (2014): NMDA receptor-dependent long-term potentiation comprises a family of temporally overlapping forms of synaptic plasticity that are induced by different patterns of stimulation. In: *Philosophical transactions of the Royal Society of London. Series B, Biological sciences* 369 (1633), S. 20130131. DOI: 10.1098/rstb.2013.0131.

Pelkey, Kenneth A.; Chittajallu, Ramesh; Craig, Michael T.; Tricoire, Ludovic; Wester, Jason C.; McBain, Chris J. (2017): Hippocampal GABAergic Inhibitory Interneurons. In: *Physiological Reviews* 97 (4), S. 1619–1747. DOI: 10.1152/physrev.00007.2017.

Pierce, Kristen L.; Premont, Richard T.; Lefkowitz, Robert J. (2002): Seven-transmembrane receptors. In: *Nature Reviews Molecular Cell Biology* 3 (9), S. 639–650. DOI: 10.1038/nrm908.

Pittaluga, Anna; Roggeri, Alessandra; Vallarino, Giulia; Olivero, Guendalina (2021): Somatostatin, a Presynaptic Modulator of Glutamatergic Signal in the Central Nervous System. In: *International journal of molecular sciences* 22 (11). DOI: 10.3390/ijms22115864.

Praticò, Domenico (2008): Oxidative stress hypothesis in Alzheimer's disease: a reappraisal. In: *Trends in pharmacological sciences* 29 (12), S. 609–615. DOI: 10.1016/j.tips.2008.09.001.

Preston, Alison R.; Eichenbaum, Howard (2013): Interplay of hippocampus and prefrontal cortex in memory. In: *Current biology : CB* 23 (17), R764-73. DOI: 10.1016/j.cub.2013.05.041.

Racine, Anne-Sophie; Michon, François-Xavier; Laplante, Isabel; Lacaille, Jean-Claude (2021): Somatostatin contributes to long-term potentiation at excitatory synapses onto hippocampal somatostatinergic interneurons. In: *Molecular brain* 14 (1), S. 130. DOI: 10.1186/s13041-021-00830-6.

Rai, Uma; Thrimawithana, Thilini R.; Valery, Celine; Young, Simon A. (2015): Therapeutic uses of somatostatin and its analogues: Current view and potential applications. In: *Pharmacology & therapeutics* 152, S. 98–110. DOI: 10.1016/j.pharmthera.2015.05.007.

Ranganath, Charan (2010): Binding Items and Contexts: The Cognitive Neuroscience of Episodic Memory. In: *Current Directions in Psychological Science* 19 (3), S. 131–137. DOI: 10.1177/0963721410368805.

Regland, B.; Gottfries, C. G. (1992): The role of amyloid beta-protein in Alzheimer's disease. In: *Lancet (London, England)* 340 (8817), S. 467–469. DOI: 10.1016/0140-6736(92)91780-c.

Robinson, Hannah L.; Nicholson, Katherine L.; Shelton, Keith L.; Hamilton, Peter J.; Banks, Matthew L. (2023): Comparison of three DREADD agonists acting on Gq-DREADDs in the ventral tegmental area to alter locomotor activity in tyrosine hydroxylase:Cre male and female rats. In: *Behavioural Brain Research* 455, S. 114674. DOI: 10.1016/j.bbr.2023.114674.

Rolls, Edmund T.; Treves, Alessandro (2024): A theory of hippocampal function: New developments. In: *Progress in neurobiology* 238, S. 102636. DOI: 10.1016/j.pneurobio.2024.102636.

Rosenbaum, Daniel M.; Rasmussen, Søren G. F.; Kobilka, Brian K. (2009): The structure and function of G-protein-coupled receptors. In: *Nature* 459 (7245), S. 356–363. DOI: 10.1038/nature08144.

Roth, Bryan L. (2016): DREADDs for Neuroscientists. In: *Neuron* 89 (4), S. 683–694. DOI: 10.1016/j.neuron.2016.01.040.

Sandoval, Karin E.; Witt, Ken A. (2024): Somatostatin: Linking Cognition and Alzheimer Disease to Therapeutic Targeting. In: *Pharmacological Reviews* 76 (6), S. 1291–1325. DOI: 10.1124/pharmrev.124.001117.

Schindelin, Johannes; Arganda-Carreras, Ignacio; Frise, Erwin; Kaynig, Verena; Longair, Mark; Pietzsch, Tobias et al. (2012): Fiji: an open-source platform for biological-image analysis. In: *Nature Methods* 9 (7), S. 676–682. DOI: 10.1038/nmeth.2019.

Schmid, Lena C.; Mittag, Manuel; Poll, Stefanie; Steffen, Julia; Wagner, Jens; Geis, Hans-Rüdiger et al. (2016): Dysfunction of Somatostatin-Positive Interneurons Associated with Memory Deficits in an Alzheimer's Disease Model. In: *Neuron* 92 (1), S. 114–125. DOI: 10.1016/j.neuron.2016.08.034.

Schulz, Jan M.; Knoflach, Frederic; Hernandez, Maria-Clemencia; Bischofberger, Josef (2018): Dendrite-targeting interneurons control synaptic NMDA-receptor activation via nonlinear α5-GABAA receptors. In: *Nature Communications* 9 (1), S. 3576. DOI: 10.1038/s41467-018-06004-8.

SCOVILLE, W. B.; MILNER, B. (1957): Loss of recent memory after bilateral hippocampal lesions. In: *Journal of neurology, neurosurgery, and psychiatry* 20 (1), S. 11–21. DOI: 10.1136/jnnp.20.1.11.

Selkoe, Dennis J.; Hardy, John (2016): The amyloid hypothesis of Alzheimer's disease at 25 years. In: *EMBO molecular medicine* 8 (6), S. 595–608. DOI: 10.15252/emmm.201606210.

Shansky, Rebecca M. (2018): Sex differences in behavioral strategies: avoiding interpretational pitfalls. In: *Current Opinion in Neurobiology* 49, S. 95–98. DOI: 10.1016/j.conb.2018.01.007.

Siapas, Athanassios G.; Lubenov, Evgueniy V.; Wilson, Matthew A. (2005): Prefrontal phase locking to hippocampal theta oscillations. In: *Neuron* 46 (1), S. 141–151. DOI: 10.1016/j.neuron.2005.02.028.

Sierra-Mercado, Demetrio; Padilla-Coreano, Nancy; Quirk, Gregory J. (2011): Dissociable roles of prelimbic and infralimbic cortices, ventral hippocampus, and basolateral amygdala in the expression and extinction of conditioned fear. In: *Neuropsychopharmacology : official publication of the American College of Neuropsychopharmacology* 36 (2), S. 529–538. DOI: 10.1038/npp.2010.184.

Sigurdsson, Torfi; Stark, Kimberly L.; Karayiorgou, Maria; Gogos, Joseph A.; Gordon, Joshua A. (2010): Impaired hippocampal–prefrontal synchrony in a genetic mouse model of schizophrenia. In: *Nature* 464 (7289), S. 763–767. DOI: 10.1038/nature08855.

Siwani, Samer; França, Arthur S.C.; Mikulovic, Sanja; Reis, Amilcar; Hilscher, Markus M.; Edwards, Steven J. et al. (2018): OLMα2 Cells Bidirectionally Modulate Learning. In: *Neuron* 99 (2), 404-412.e3. DOI: 10.1016/j.neuron.2018.06.022.

Song, You-Hyang; Yoon, Jiwon; Lee, Seung-Hee (2021): The role of neuropeptide somatostatin in the brain and its application in treating neurological disorders. In: *Experimental & Molecular Medicine* 53 (3), S. 328–338. DOI: 10.1038/s12276-021-00580-4.

Spellman, Timothy; Rigotti, Mattia; Ahmari, Susanne E.; Fusi, Stefano; Gogos, Joseph A.; Gordon, Joshua A. (2015a): Hippocampal-prefrontal input supports spatial encoding in working memory. In: *Nature* 522 (7556), S. 309–314. DOI: 10.1038/nature14445.

Spellman, Timothy; Rigotti, Mattia; Ahmari, Susanne E.; Fusi, Stefano; Gogos, Joseph A.; Gordon, Joshua A. (2015b): Hippocampal–prefrontal input supports spatial encoding in working memory. In: *Nature* 522 (7556), S. 309–314. DOI: 10.1038/nature14445.

Spires-Jones, Tara L.; Hyman, Bradley T. (2014): The intersection of amyloid beta and tau at synapses in Alzheimer's disease. In: *Neuron* 82 (4), S. 756–771. DOI: 10.1016/j.neuron.2014.05.004.

Squire, Larry R.; Wixted, John T. (2011): The cognitive neuroscience of human memory since H.M. In: *Annual review of neuroscience* 34, S. 259–288. DOI: 10.1146/annurev-neuro-061010-113720.

Swerdlow, Russell H. (2020): The mitochondrial hypothesis: Dysfunction, bioenergetic defects, and the metabolic link to Alzheimer's disease. In: *International review of neurobiology* 154, S. 207–233. DOI: 10.1016/bs.irn.2020.01.008.

Takeuchi, Tomonori; Duszkiewicz, Adrian J.; Sonneborn, Alex; Spooner, Patrick A.; Yamasaki, Miwako; Watanabe, Masahiko et al. (2016): Locus coeruleus and dopaminergic consolidation of everyday memory. In: *Nature* 537 (7620), S. 357–362. DOI: 10.1038/nature19325.

Tamura, Makoto; Spellman, Timothy J.; Rosen, Andrew M.; Gogos, Joseph A.; Gordon, Joshua A. (2017): Hippocampal-prefrontal theta-gamma coupling during performance of a spatial working memory task. In: *Nature Communications* 8 (1), S. 2182. DOI: 10.1038/s41467-017-02108-9.

Taniguchi, Hiroki; He, Miao; Wu, Priscilla; Kim, Sangyong; Paik, Raehum; Sugino, Ken et al. (2011): A resource of Cre driver lines for genetic targeting of GABAergic neurons in cerebral cortex. In: *Neuron* 71 (6), S. 995–1013. DOI: 10.1016/j.neuron.2011.07.026.

Tervo, D. Gowanlock R.; Hwang, Bum-Yeol; Viswanathan, Sarada; Gaj, Thomas; Lavzin, Maria; Ritola, Kimberly D. et al. (2016): A Designer AAV Variant Permits Efficient Retrograde Access to Projection Neurons. In: *Neuron* 92 (2), S. 372–382. DOI: 10.1016/j.neuron.2016.09.021.

Thompson, Karen J.; Khajehali, Elham; Bradley, Sophie J.; Navarrete, Jovana S.; Huang, Xi Ping; Slocum, Samuel et al. (2018): DREADD Agonist 21 Is an Effective Agonist for Muscarinic-Based DREADDs in Vitro and in Vivo. In: *ACS Pharmacology & Translational Science* 1 (1), S. 61–72. DOI: 10.1021/acsptsci.8b00012.

Thulin, Angelica; Henriksson, Katharina; Nogueira, Ingrid; Kullander, Klas (2025): Differentiated Presynaptic Input to OLMα2 Cells Along the Hippocampal Dorsoventral Axis: Implications for Hippocampal Microcircuit Function. In: *Hippocampus* 35 (5), e70026. DOI: 10.1002/hipo.70026.

Turi, Gergely Farkas; Li, Wen-Ke; Chavlis, Spyridon; Pandi, Ioanna; O'Hare, Justin; Priestley, James Benjamin et al. (2019): Vasoactive Intestinal Polypeptide-Expressing Interneurons

in the Hippocampus Support Goal-Oriented Spatial Learning. In: *Neuron* 101 (6), 1150-1165.e8. DOI: 10.1016/j.neuron.2019.01.009.

Tyan, Leonid; Chamberland, Simon; Magnin, Elise; Camiré, Olivier; Francavilla, Ruggiero; David, Linda Suzanne et al. (2014): Dendritic inhibition provided by interneuron-specific cells controls the firing rate and timing of the hippocampal feedback inhibitory circuitry. In: *The Journal of neuroscience : the official journal of the Society for Neuroscience* 34 (13), S. 4534–4547. DOI: 10.1523/JNEUROSCI.3813-13.2014.

Urban, Daniel J.; Roth, Bryan L. (2015): DREADDs (designer receptors exclusively activated by designer drugs): chemogenetic tools with therapeutic utility. In: *Annual review of pharmacology and toxicology* 55, S. 399–417. DOI: 10.1146/annurev-pharmtox-010814-124803.

Venegas, Carmen; Kumar, Sathish; Franklin, Bernardo S.; Dierkes, Tobias; Brinkschulte, Rebecca; Tejera, Dario et al. (2017): Microglia-derived ASC specks cross-seed amyloid-β in Alzheimer's disease. In: *Nature* 552 (7685), S. 355–361. DOI: 10.1038/nature25158.

Vertes, Robert P. (2006): Interactions among the medial prefrontal cortex, hippocampus and midline thalamus in emotional and cognitive processing in the rat. In: *Neuroscience* 142 (1), S. 1–20. DOI: 10.1016/j.neuroscience.2006.06.027.

Walsh, Dominic M.; Selkoe, Dennis J. (2007): Aβ Oligomers – a decade of discovery. In: *Journal of neurochemistry* 101 (5), S. 1172–1184. DOI: 10.1111/j.1471-4159.2006.04426.x.

Wang, Jianquan; Markesbery, William R.; Lovell, Mark A. (2006): Increased oxidative damage in nuclear and mitochondrial DNA in mild cognitive impairment. In: *Journal of neurochemistry* 96 (3), S. 825–832. DOI: 10.1111/j.1471-4159.2005.03615.x.

Wang, Shuguang; Liao, Zuning; Zhang, Qiying; Han, Xinyuan; Liu, Changqing; Wang, Jin (2025): Mitochondrial dysfunction in Alzheimer's disease: a key frontier for future targeted therapies. In: *Frontiers in Immunology* Volume 15 - 2024. DOI: 10.3389/fimmu.2024.1484373.

Wang, Szu-Han; Redondo, Roger L.; Morris, Richard G. M. (2010): Relevance of synaptic tagging and capture to the persistence of long-term potentiation and everyday spatial memory. In: *Proceedings of the National Academy of Sciences* 107 (45), S. 19537–19542. DOI: 10.1073/pnas.1008638107.

Weis, William I.; Kobilka, Brian K. (2018): The Molecular Basis of G Protein-Coupled Receptor Activation. In: *Annual review of biochemistry* 87, S. 897–919. DOI: 10.1146/annurev-biochem-060614-033910.

Whitehouse, P. J.; Price, D. L.; Clark, A. W.; Coyle, J. T.; DeLong, M. R. (1981): Alzheimer disease: evidence for selective loss of cholinergic neurons in the nucleus basalis. In: *Annals of neurology* 10 (2), S. 122–126. DOI: 10.1002/ana.410100203.

Wirt, Ryan. A.; Crew, Lauren. A.; Ortiz, Andrew. A.; McNeela, Adam. M.; Flores, Emmanuel; Kinney, Jefferson. W.; Hyman, James M. (2021): Altered theta rhythm and hippocampal-cortical interactions underlie working memory deficits in a hyperglycemia risk factor model of Alzheimer's disease. In: *Communications Biology* 4 (1), S. 1036. DOI: 10.1038/s42003-021-02558-4.

Zatta, Paolo; Drago, Denise; Bolognin, Silvia; Sensi, Stefano L. (2009): Alzheimer's disease, metal ions and metal homeostatic therapy. In: *Trends in pharmacological sciences* 30 (7), S. 346–355. DOI: 10.1016/j.tips.2009.05.002.

Zhang, Jifa; Zhang, Yinglu; Wang, Jiaxing; Xia, Yilin; Zhang, Jiaxian; Chen, Lei (2024): Recent advances in Alzheimer's disease: mechanisms, clinical trials and new drug development strategies. In: *Signal Transduction and Targeted Therapy* 9 (1), S. 211. DOI: 10.1038/s41392-024-01911-3.

Zhang, Zhigang; Yang, Xifei; Song, You-Qiang; Tu, Jie (2021): Autophagy in Alzheimer's disease pathogenesis: Therapeutic potential and future perspectives. In: *Ageing research reviews* 72, S. 101464. DOI: 10.1016/j.arr.2021.101464.